공학박사 학위논문

독립형 교류 마이크로그리드에서 전압 품질을 개선한 정확한 전력분배 제어기법

Advanced Control Strategies for Accurate Power Sharing with Enhanced Voltage Quality in Islanded AC Microgrids

울산대학교 대학원
전기공학부
HOANG VAN TUAN

공학박사 학위논문

독립형 교류 마이크로그리드에서 전압 품질을 개선한 정확한 전력분배 제어기법

Advanced Control Strategies for Accurate Power Sharing with Enhanced Voltage Quality in Islanded AC Microgrids

지도교수 이홍희

이 논문을 공학박사 학위논문으로 제출함

2020년 06월

울산대학교 대학원

전기공학부

HOANG VAN TUAN

울산대학교 UNIVERSITY OF ULSAN

HOANG VAN TUAN 의 공학박사 학위논문을 인준함

심사위원장	전태원	(인)
심사위원	이홍희	(인)
심사위원	최성진	(인)
심사위원	이동춘	(인)
심사위원	정의헌	(인)

울산대학교 대학원

2020년 06월

UNIVERSITY OF ULSAN

Advanced Control Strategies for Accurate Power Sharing with Enhanced Voltage Quality in Islanded AC Microgrids

by

HOANG VAN TUAN

Supervisor: Professor Hong-Hee Lee

A dissertation
submitted in partial fulfillment
for the degree of Doctor of Philosophy
in
School of Electrical Engineering
University of Ulsan

June, 2020

This certifies that the doctoral dissertation of HOANG VAN TUAN is approved by:

1. Committee Chair: **Professor Tae-Won Chun**

Signature: 

2. Committee Member: **Professor Hong-Hee Lee**

Signature: 

3. Committee Member: **Professor Sung-Jin Choi**

Signature: 

4. Committee Member: **Professor Dong-Choon Lee**

Signature: 

5. Committee Member: **Doctor Eui-Heon Jung**

Signature: 

School of Electrical Engineering

University of Ulsan

Ulsan, Korea

June, 2020

To my beloved wife and families

Abstract

With the growth of environmental awareness and concerns about carbon emission, distributed generators (DGs) such as photovoltaics, wind turbines, fuel cells, and microturbines have been extensively used in power distribution system. Microgrid concept has been widely adopted to effectively coordinate the operation of multiple parallel DGs because it can flexibly operate in either grid-connected mode or islanded mode to provide cost-effective operation and more reliable power. In islanded mode, the droop controller has been conventionally adopted to operate the microgrid. However, it is impossible to satisfy the power sharing accuracy and voltage quality requirements with the conventional droop controller. Therefore, this thesis presents advanced control strategies to address these power sharing and power quality issues in islanded microgrids.

Firstly, based on analysis of an islanded microgrid with meshed structure, enhanced power sharing control schemes based on centralized approach or distributed approach are developed to share active and reactive power accurately in a meshed microgrid, with the aid of adaptive regulation of the virtual impedances. The proposed control methods always achieve accurate power sharing even when the microgrid configuration or the load condition is changed. Furthermore, the proposed control strategy can be implemented directly without any knowledge of the detailed microgrid configuration or the required load power measurement, which decreases the complexity and cost of the system.

Next, in order to guarantee accurate power sharing even though nonlinear load is applied intensively into the microgrid system, the thesis presents an enhanced control scheme by adaptively regulating virtual impedances at dominant frequencies. The proposed scheme provides accurate active, reactive, and harmonic power sharing despite variations of microgrid configuration or load condition. Additionally, a simple secondary controller has also been proposed to remove the frequency and voltage magnitude deviations without additional voltage measurement at the point of common coupling (PCC). The complexity and cost of the system are significantly reduced because no information about the detailed microgrid configuration, feeder impedances, and the load powers is needed.

Finally, an enhanced DG virtual impedance controller (VIC) is proposed to provide accurate harmonic power sharing along with voltage harmonic compensation in islanded

microgrids. The proposed VIC is developed based on simple integral controllers with two controllable parts and no information about the feeder impedances or load currents. The control performance is theoretically analyzed using a small-signal state-space model to evaluate the system dynamics and stability.

All control strategies are validated through digital simulation using PSIM and experiment with scaled-down microgrid prototypes in the laboratory. The obtained results verify the feasibility and effectiveness of the proposed control schemes. The last part of the thesis draws conclusions and offers future studies of the research.

Acknowledgments

This work was supported in part by the National Research Foundation of Korea Grand funded by the Korean Government (NRF-2015R1D1A1A09058166) and in part by the Networked-based Automation Research Center (NARC) funded by the Ministry of Trade, Industry & Energy.

I would like to thank deeply my supervisor, Professor Hong-Hee Lee, for his guidance and support throughout the course of this work. It has been my great happiness to work with him since I came to Industrial Network and Power Electronics Laboratory (INPEL). I am thankful to Professors in Committee Member for the time and evaluations on my thesis. Equally, I would like to express my sincere gratitude to all Professors in University of Ulsan (UOU) who gave lectures and supports to me during my courses. I would also like to thank to financial supports from Brain Korea 21 Plus program in UOU. A big thank goes to University of Ulsan for giving me a great opportunity to complete my Ph.D. degree successfully.

I also would like to express my warm gratitude to all INPEL members who have been my side with happy moments. I hope all of you will be successful in the future.

Last but not least, I am grateful as ever for the encouragement and love shown by my wife and families during this research work.

Ulsan, June 2020

Hoang Van Tuan

Contents

Abstract i

Acknowledgments iii

Abbreviations xiv

1 Introduction 1

1.1 Microgrid Concept . . . 1
1.2 Literature Review and Problem Statement . . . 3
1.2.1 Inaccurate Power Sharing among DG Units . . . 4
1.2.2 Frequency and Voltage Magnitude Deviations . . . 7
1.2.3 Highly Distorted PCC Voltage . . . 8
1.3 Research Objectives . . . 9
1.4 Contributions of the Thesis . . . 9
1.5 Outline of the Thesis . . . 11

2 Accurate Active and Reactive Power Sharing Strategies 12

2.1 Centralized Power Sharing Control Strategy . . . 12
2.1.1 Operating Principle of an Islanded Microgrid . . . 12
2.1.2 Proposed Control Scheme . . . 16
2.1.3 Simulation Results . . . 20
2.1.4 Experimental Varification . . . 25
2.1.5 Conclusion of the Section . . . 28
2.2 Distributed Power Sharing Control Strategy . . . 30
2.2.1 Preliminaries . . . 30
2.2.2 Proposed Control Scheme . . . 32
2.2.3 Steady-State and Small-Signal Analysis . . . 34
2.2.4 Simulation Results . . . 40
2.2.5 Experimental Results . . . 45
2.2.6 Conclusion of the Section . . . 48

3 Accurate Harmonic Power Sharing Strategy **49**
3.1 Power Sharing Control Analysis 49
3.2 Proposed Control Scheme 53
3.2.1 Microgrid Central Controller 54
3.2.2 Local Controller 56
3.2.3 Stability Analysis by Investigating the Effective Harmonic Impedance 60
3.3 Simulation Results 62
3.4 Experimental Verification 66
3.4.1 Case I: Same Power Ratings 69
3.4.2 Case II: Different Power Ratings 70
3.5 Conclusion of the Chapter 72

4 PCC Voltage Harmonic Compensation Strategy **73**
4.1 Islanded Microgrid Analysis 73
4.1.1 Active and Reactive Power Sharing 74
4.1.2 Harmonic Power Sharing Analysis 75
4.1.3 PCC Voltage Harmonic Compensation Analysis 76
4.2 Proposed Virtual Harmonic Impedance Scheme 76
4.2.1 Proposed Virtual Impedance with Two Controllable Parts 77
4.2.2 Proposed Virtual Harmonic Impedance Controller 79
4.2.3 Small-Signal Stability Analysis 81
4.2.4 Stability with Communication Delay 84
4.3 Simulation Results 86
4.3.1 Control Performance with the Proposed Method 86
4.3.2 Plug-and-Play Operation 91
4.3.3 Effect of Communication Delay 91
4.3.4 Communication Link Failure 93
4.3.5 Effect of Local Load 93
4.4 Experimental Results 94
4.5 Conclusion of the Chapter 98

5 Conclusions and Future Works **100**
5.1 Conclusions 100
5.2 Future works 101

Appendix A - State Matrices in Chapter 2 **102**

Appendix B - State Matrices in Chapter 4 **104**

Appendix C - Publications **105**
Journal Articles 105
Conferences 105

Bibliography **106**

List of Figures

1.1 Architecture of the AC microgrid. 2
1.2 Droop-based control scheme for a DG unit. 3
1.3 Model of a droop-controlled DG unit. 4
1.4 Configuration of a meshed microgrid. 6

2.1 Configuration of the meshed microgrid. 13
2.2 Meshed microgrid with two DGs. 14
2.3 Proposed local control scheme. 17
2.4 Model of DG unit with virtual impedance. 18
2.5 Meshed microgrid used in the simulation. 20
2.6 Simulated power sharing performance of the conventional droop control. (a) Reactive power. (b) Real power. (c) Q_{err_i} (%). 22
2.7 Simulated power sharing performance with the centralized control scheme. (a) Reactive power. (b) Real power. (c) Q_{err_i} (%). 23
2.8 Simulated performance of the proposed controller with same DG units. (a) Reactive power. (b) Real power. (c) Q_{err_i} (%). (d) Variation of virtual inductance. 24
2.9 Simulated performance of the proposed controller with different DG units. (a) Reactive power. (b) Real power. (c) Q_{err_i} (%). (d) Variation of virtual inductance. 25
2.10 Simulated performance of the proposed controller before and after losing communications, and after recovering communication. 26
2.11 Meshed microgrid used in experiment. 27
2.12 Experimental power sharing performance of the proposed controller with same DG units. (a) Real power. (b) Reactive power. 27
2.13 Zoom-in DG current waveforms with: (a) Conventional droop method; (b) Proposed method (activated at $t = t_1$); (c) Proposed method under load change operation (Load 1 is connected at $t = t_2$); (d) Proposed method under local load effect (Load 2 is connected $t = t_3$). 28

2.14 Experimental reactive power sharing performance of the proposed controller when a load change during regulating virtual impedance period. 29
2.15 Experimental power sharing performance of the proposed controller with different DG units. (a) Real power. (b) Reactive power. (c) Q_{err_i} (%). . 29
2.16 Experimental reactive-power-sharing performance under plug-and-play operation. 30
2.17 Model of a DG unit 31
2.18 Proposed power control scheme for i-th DG unit 32
2.19 The islanded microgrid used in stability analysis and experiment 36
2.20 Root locus diagram according to control gain k_0 with negligible communication delay ($\tau = 0$): $0 \leq k_0 \leq 20$, $m_1 = 0.5m_2 = m_3 = 0.0015rad/W \centerdot s$, $n_1 = 0.5n_2 = n_3 = 0.007V/Var$, $\omega_{LPF} = 31.5rad/s$. 39
2.21 Root locus diagram according to communication delay τ: $0 \leq \tau \leq 150ms$, $m_1 = 0.5m_2 = m_3 = 0.0015rad/W \centerdot s$, $n_1 = 0.5n_2 = n_3 = 0.007V/Var$, $\omega_{LPF} = 31.5rad/s$, $k_0 = 12$. 40
2.22 The islanded microgrid used in simulation. 41
2.23 Control performance with proposed control scheme: (a) active power; (b) reactive power; (c) DG virtual impedance; (d) frequency set point; (e) voltage magnitude set point. 42
2.24 Control performance with proposed control scheme during a communication link failure: (a) active power; (b) reactive power; (c) DG virtual impedance; (d) frequency set point; (e) voltage magnitude set point. 43
2.25 Control performance in plug-and-play operation: (a) active power; (b) reactive power; (c) frequency set point; (d) voltage magnitude set point. . . . 44
2.26 The photo of the experimental setup. 45
2.27 Control performance with proposed control scheme: (a) active power; (b) reactive power; (c) frequency set point; (d) voltage magnitude set point. . . 46
2.28 Control performance with proposed control scheme during a communication failure: (a) active power; (b) reactive power; (c) frequency set point; (d) voltage magnitude set point. 46
2.29 The dynamic responses for various values of k_0: (a) $k_0 = 2$; (b) $k_0 = 7$; (c) $k_0 = 12$; (d) $k_0 = 17$. 47
2.30 The dynamic responses for different communication delays: (a) $\tau = 1ms$; (b) $\tau = 50ms$; (c) $\tau = 100ms$; (d) $\tau = 150ms$. 47

3.1 A meshed microgrid with two DG units. 50

3.2 Equivalent circuits of the microgrid at different frequencies: (a) at fundamental frequency, (b) at harmonic frequencies. 50
3.3 Equivalent circuit of the microgrid at harmonic frequencies when each nonlinear load is separately analyzed. 51
3.4 Proposed control scheme. 54
3.5 Decomposition of fundamental and harmonic components (T denotes the fundamental cycle time). 56
3.6 Equivalent model of the microgrid in Fig. 1 for h-order harmonic frequency: (a) without the virtual impedance; (b) with the virtual impedance. 59
3.7 Meshed microgrid used in simulation. 61
3.8 Simulated power sharing performance: (a) active power; (b) reactive power; (c) 3rd harmonic power; and (d) 5th harmonic power. 62
3.9 Simulated performance of the proposed secondary controller: (a) frequency; (b) average voltage; (c) DG output voltage magnitude. 63
3.10 Variation of virtual inductances: (a) at fundamental frequency; (b) at 3rd harmonic frequency; (c) at 5th harmonic frequency. 64
3.11 Harmonic components of DG currents. (a) DG out currents with conventional droop method. (b) 3rd harmonic currents with conventional droop method. (c) 5th harmonic currents with conventional droop method. (d) DG out currents with proposed method. (e) 3rd harmonic currents with proposed method. (f) 5th harmonic currents with proposed method. (g) DG out currents with proposed method with increased load. (h) 3rd harmonic currents with proposed method with increased load. (i) 5th harmonic currents with proposed method with increased load. 65
3.12 Simulation performance with the proposed controller under the plug-and-play operation. (a) Active power. (b) Reactive power. (c) Third harmonic power. (d) Fifth harmonic power. (e) Frequency. (f) Average value of the DG fundamental output voltages. 66
3.13 Simulated power sharing performance of the proposed controller before and after losing communication, and after recovering communication. (a) Active power. (b) Reactive power. (c) Third harmonic power. (d) Fifth harmonic power. 67
3.14 Simulated power sharing performance of the conventional droop controller. (a) Active power. (b) Reactive power. (c) Third harmonic power. (d) Fifth harmonic power. 68
3.15 Meshed microgrid used in the experiment. 68

3.16 Experimental performance with the proposed controller (Case I). (a) Active power. (b) Reactive power. (c) Third harmonic power. (d) Fifth harmonic power. (e) Frequency. (f) Average and DG output voltage magnitudes. . . 69
3.17 Zoomed-in view of DG current waveforms with (Case I). (a) Conventional droop method. (b) Proposed virtual impedance control method (activated at $t = t_1$). (c) Proposed secondary controller (activated at $t = t_2$). (d) Proposed method with increased load (Load3 is connected at $t = t_3$). (e) Proposed method with decreased load (Load3 is disconnected at $t = t_4$). . 70
3.18 Experimental performance with the proposed controller under the plug-and-play operation (Case I). (a) Active power. (b) Reactive power. (c) Third harmonic power. (d) Fifth harmonic power. (e) Frequency. (f) Average value of the DG fundamental output voltages. 71
3.19 Experimental performance with the proposed controller (Case II). (a) Active power. (b) Reactive power. (c) Third harmonic power. (d) Fifth harmonic power. (e) Frequency. (f) Average and DG output voltage magnitudes. 71

4.1 Configuration of the islanded microgrid. 74
4.2 Equivalent circuit of two DG units at h-order harmonic frequency. 75
4.3 Equivalent circuit of two DG units at h-order harmonic frequency with the proposed virtual harmonic impedance. 77
4.4 Proposed control scheme. 79
4.5 The islanded microgrid used for small-signal analysis and simulations. . . . 80
4.6 Root locus diagram according to control gain k_H^3 with: $0 < k_H^3 < 0.000018$, $\omega_{LPF} = 100rad/s$ and $k_C^3 = 20$. 83
4.7 Root locus diagram according to control gain k_C^3 with: $0 < k_C^3 < 50$, $\omega_{LPF} = 100rad/s$ and $k_H^3 = 0.000015$. 83
4.8 Root locus diagram according to control gain k_H^5 with: $0 < k_H^5 < 0.0005$, $\omega_{LPF} = 100rad/s$ and $k_C^5 = 35$. 84
4.9 Root locus diagram according to control gain k_C^5 with: $0 < k_C^5 < 80$, $\omega_{LPF} = 100rad/s$ and $k_H^5 = 0.00035$. 84
4.10 Root locus diagram according to communication delay τ: $0 \leq \tau \leq 50ms$, $k_C^3 = 20$, $k_H^3 = 0.000015$, and $\omega_{LPF} = 100rad/s$. 85
4.11 Root locus diagram according to communication delay τ: $0 \leq \tau \leq 50ms$, $k_C^3 = 8$, $k_H^3 = 0.000015$, and $\omega_{LPF} = 100rad/s$. 85
4.12 Root locus diagram according to communication delay τ: $0 \leq \tau \leq 100ms$, $k_C^3 = 4$, $k_H^3 = 0.000015$, and $\omega_{LPF} = 100rad/s$. 86

4.13 Simulated power sharing performance: (a) active power; (b) reactive power; (c) 3rd harmonic power; (d) 5th harmonic power. 87
4.14 Zoon-in DG current waveforms corresponding to stages in Fig. 4.10: (a) stage 1; (b) stage 2; (c) stage 3. 88
4.15 PCC harmonic distortion indexes. 88
4.16 Zoon-in PCC voltage waveforms corresponding to stages in Fig. 4.10: (a) stage 1; (b) stage 2; (c) stage 3. 89
4.17 Zoon-in DG output voltage waveforms corresponding to stages in Fig. 4.10: (a) stage 1; (b) stage 2; (c) stage 3. 90
4.18 Variations of DG virtual impedances: (a) at 3rd harmonic frequency; (b) at 5th harmonic frequency. 90
4.19 Control performance under plug-and-play operation: (a) 3rd harmonic power; (b) 5th harmonic power; (c) harmonic distortion. 91
4.20 Dynamic responses for different communication delays and gains: (a) $\tau = 1ms$, $k_C^3 = 20$, $k_C^5 = 35$; (b) $\tau = 15ms$, $k_C^3 = 20$, $k_C^3 = 35$; (c) $\tau = 25ms$, $k_C^3 = 20$, $k_H^3 = 35$; (d) $\tau = 25ms$, $k_C^3 = 8$, $k_C^5 = 17$. 92
4.21 Control performance of the proposed controller before and after losing communication, and after recovering communication: (a) 3rd harmonic power; (b) 5th harmonic power; (c) harmonic distortion. 93
4.22 Control performance of the proposed controller when connecting and disconnecting a local load: (a) 3rd harmonic power; (b) 5th harmonic power; (c) harmonic distortion. 94
4.23 The islanded microgrid used for experiment: (a) photo of laboratory setup; (b) equivalent circuit. 95
4.24 Experimental power sharing performance with proposed controller: (a) active power; (b) reactive power; (c) 3rd harmonic power; (d) 5th harmonic power. 95
4.25 Zoom-in DG current waveforms with: (a) conventional droop method; (b) first virtual impedance part (activated at t1); (c) second virtual impedance part (activated at t2); (d) proposed method with increased load (Load 3 is connected at t3). 96
4.26 PCC harmonic distortion indexes. 96
4.27 Zoom-in PCC voltage waveforms in: (a) stage 1; (b) stage 3. 97
4.28 The harmonic spectra of PCC voltage waveforms without compensation in stage 1 (cyan) and with compensation in stage 3 (blue). 97

4.29 Dynamic performance with different communication delays and gains: (a) $\tau = 10ms$, $k_C^3 = 3$; (b) $\tau = 10ms$, $k_C^3 = 6$; (c) $\tau = 50ms$, $k_C^3 = 6$; (d) $\tau = 50ms$, $k_C^3 = 1.5$. 98

List of Tables

2.1 Sensitivity of ΔQ_{12} with respective to the change in the real and reactive powers. 15
2.2 System Parameters. 21
2.3 System parameters 37

3.1 System Parameters. 55

4.1 System Parameters 81
4.2 Comparison of the control performance in each stage 90

Abbreviations

AC	Alternating Current
DC	Direct Current
DER	Distributed Energy Resource
DG	Distributed Generator
DSP	Digital Signal Processor
MGCC	Microgrid Central Controller
PCC	Point of Common Coupling
PLL	Phase locked Loop
PI	Proportional–Integral
PWM	Pulse Width Modulation
SOGI	Second Order Generalized Integrator
THD	Total Harmonic Distortion
UPS	Uninterruptible Power Supply

Chapter 1

Introduction

The concept of microgrids is introduced in this chapter. Thereafter, microgrid control issues are discussed along with the literature review. Finally, objectives and contributions of the thesis are presented, followed by the thesis outline.

1.1 Microgrid Concept

With the growth of environmental awareness and concerns about carbon emissions, distributed generators (DGs) using renewable energy resources such as photovoltaics, wind turbines, fuel cells, and microturbines have been extensively used in power distribution systems in recent years to meet the rising load demand for utilities [1–3]. Because the output voltage of these energy resources is either in DC or in uncontrolled AC form, power electronics-based converters are commonly used to interface these sources [4–6]. Given that increasing numbers of power electronics-based DGs have been integrated into the power grid recently, some notable problems have been resulted in such areas such as power management, resonance, and system stability. Subsequently, the microgrid concept has been introduced as the best solution for these issues. A microgrid (MG) is defined by Microgrid Exchange Group (MEG) of the U.S Department of Energy (DOE) [7] as "a group of interconnected loads and distributed energy resources within clearly defined electrical boundaries that acts as a single controllable entity with respect to the grid. A microgrid can connect and disconnect from the grid to enable it to operate in both grid-connected or islanded mode."

Fig. 1.1 shows the basic architecture of an AC MG system. Renewable energy sources (RESs) such as PV and wind turbines are connected to the point of common coupling (PCC) through converters. A microgrid can operate flexibly in either a grid-connected or an islanded mode to provide a cost-effective operation and a reliable power supply to loads and customers [8–11]. In the grid-connected mode, the operating voltage and frequency

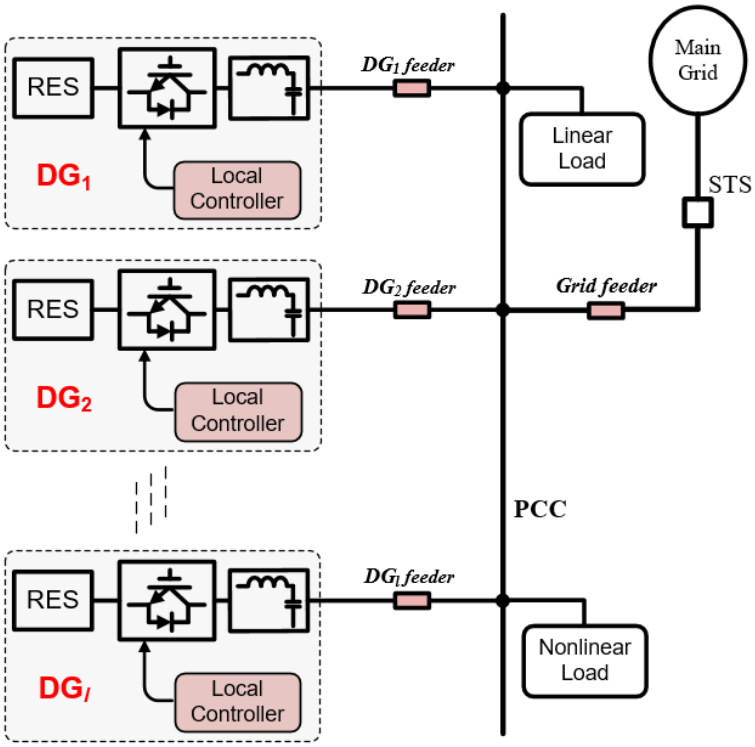

Figure 1.1: Architecture of the AC microgrid.

regulation is provided by the main grid [12]. The utility grid ensures a relatively stiff and robust frequency regulation due to the rotating mass inertia of the large synchronous generators in the power system [13]. Moreover, the amount of power exchanged between the microgrid and the grid is determined by the difference between the generation power and the load demand power in the microgrid. In other words, the main grid is responsible for maintaining the power balance in the microgrid.

In the case of islanded operation, the microgrid control is, however, more challenging because the regulation of microgrid frequency and voltage and the power balance between supply and demand must be realized by coordinate control of DG units. Conventionally, to realize frequency and voltage regulations and share load power demand among DGs in a decentralized manner, the real power-frequency ($P-\omega$) and reactive power-voltage magnitude ($Q-E$) droop control methods have been adopted [14–16].

Fig. 1.2 shows the typical droop-based control scheme for a DG unit. Each DG has an external power control loop based on droop control in which the angular frequency and voltage magnitude of the DG output are given as follows:

$$\omega = \omega_0 - mP, \tag{1.1}$$

$$E = E_0 - nQ, \tag{1.2}$$

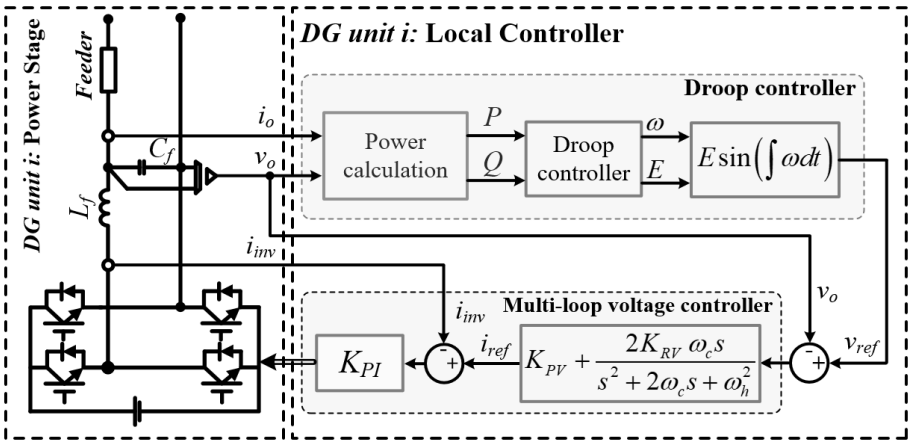

Figure 1.2: Droop-based control scheme for a DG unit.

where ω_0 and E_0 are the nominal values of the DG angular frequency and DG voltage magnitude, respectively; P and Q are the measured real and reactive powers after the low-pass filter (LPF), respectively; and m and n are the real and reactive power droop slopes, respectively. From (1.1) and (1.2), the instantaneous voltage reference V_{ref} is given as [17, 18]:

$$V_{ref} = Esin\left(\int \omega dt\right). \tag{1.3}$$

Next, in order to generate the desired output voltage for the DG unit according to the voltage reference V_{ref} in (1.3), the double-loop voltage controller is widely used [19,20]. In the double-loop voltage controller, the outer loop uses a nonideal proportional-resonant controller tuned at the fundamental frequency [21]:

$$G_{Outer}(s) = K_{PV} + \frac{2K_{RV}\omega_c s}{s^2 + 2\omega_c s + \omega^2} \tag{1.4}$$

where K_{PV} is the outer loop proportional gain, K_{RV} is the resonant controller gain at the fundamental frequency, and ω_c is the cutoff frequency of the resonant controller. The inner loop has a simple proportional control gain K_{PI} with the filter inductor current feedback, which provides sufficient damping to the output LC filter [21]:

$$G_{Inner}(s) = K_{PI}. \tag{1.5}$$

1.2 Literature Review and Problem Statement

The droop control method has many desirable features including flexibility, redundancy, and expandability because only local measurements and no communication link are re-

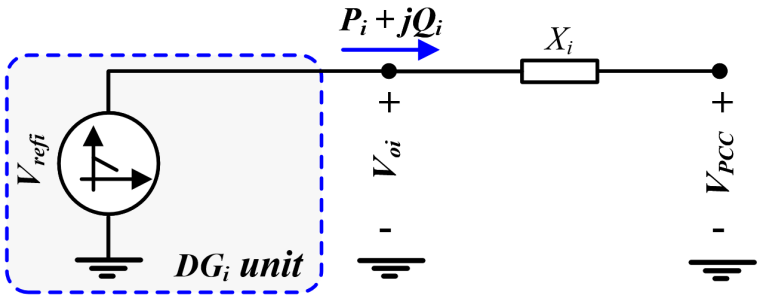

Figure 1.3: Model of a droop-controlled DG unit.

quired. Nevertheless, its application exposes several significant limitations. Problems with the droop controller and improved methods in literature are discussed as follows.

1.2.1 Inaccurate Power Sharing among DG Units

Even though real load demand power is always accurately shared among DG units according to their rated powers using the conventional droop controller, accurate reactive and harmonic power sharing cannot be realized, which may result in overload condition for some DG units.

1.2.1.1 Inaccurate Reactive Power Sharing

A DG unit interfaced to the PCC through the power feeder line is modelled as in Fig. 1.3, in which the DG unit is represented as a controllable voltage source, V_{oi} is the output voltage of DG_i unit, and V_{PCC} is the PCC voltage. Generally, the impedance of feeder line is inductive, and the line resistance can be ignored [22, 23]. Then, the impedance between the DG_i unit and PCC can be described as X_i ($X_i = \omega_i L_i$). Considering that the phase-shift angle δ_i between V_{oi} and V_{PCC} is very small, the output reactive power of DG_i unit is determined as follows:

$$Q_i = \frac{E_i V_{PCC} \sin \delta_i - V_{PCC}^2}{X_i}, \tag{1.6}$$

where X_i is the output reactance of the DG_i unit, δ_i is the phase angle between the DG_i output voltage and the PCC voltage, and E_i and V_{PCC} are the amplitude of DG_i output voltage and the PCC voltage, respectively.

Substituting (1.2) into (1.6), the reactive power of the DG unit becomes

$$Q_i = \frac{V_{PCC}(E_0 - V_{PCC})}{X_i + n_i V_{PCC}}. \tag{1.7}$$

From (1.7), the reactive power sharing error ΔQ_{ij} between two identical DGs, DG_i and DG_j, are

$$\Delta Q_{ij} = Q_i - Q_j = \frac{X_j - X_i}{V_{PCC}(E_0 - V_{PCC})} Q_i Q_j. \tag{1.8}$$

From (1.8), the accurate reactive power sharing cannot be achieved ($\Delta Q_{ij} = 0$) because the feeder impedances are mismatched ($X_j - X_i \neq 0$).

In order to solve the inaccurate power sharing problem, many methods have been proposed [24,25]. In [26], the voltage drop caused by the transmission lines was estimated online and incorporated into the power control scheme to achieve accurate reactive power sharing in an islanded microgrid. However, to estimate the voltage drop properly, the microgrid should operate in grid-connected mode before islanding mode operation. In [27], the line impedance mismatches were compensated for by controlling the reactive power in proportion to the derivative of the DG output voltage. Although the reactive power sharing error was minimized by this method, it was not completely eliminated. Authors in [28] proposed a robust droop control to ensure accurate powersharing by using the load voltage information. However, it is not easy to detect the load voltage because it is far from the controller. To achieve accurate power sharing without the droop controller, a modified double-loop voltage controller was developed in [29]. However, the overall system stops when the communication fault occurs, and it is impossible to supply the power to the loads.

To simultaneously solve the power control instability problem as well as the inaccurate power sharing difficulty, the virtual impedance technique, which modified the output voltage reference by means of a load current feed-forward loop, was introduced [30–32]. However, reactive power sharing error was not eliminated completely due to the mismatch in physical feeder impedances. In [17], the equivalent DG unit impedance was designed to be inversely proportional to the DG rating by determining the virtual impedance based on pre-knowledge of the physical feeder impedance, and the reactive power sharing errors were eliminated. However, it is generally very difficult to find the physical feeder impedance in practical applications. In [33], an equivalent model was developed to calculate the DG equivalent feeder impedance by using the feeder current and feeder impedance, and the inaccurate power sharing problem due to the effects of the mismatched equivalent feeder impedances was solved by adaptively adjusting the output virtual impedances. However, it is hard to detect the feeder impedances correctly in practical applications and the powersharing method becomes ineffective if the microgrid structure changes.

All of the aforementioned power sharing methods focus on a single-bus microgrid with a fixed configuration. However, when DG units and loads are freely connected to and disconnected from any node, the microgrid structure becomes much more complex (meshed

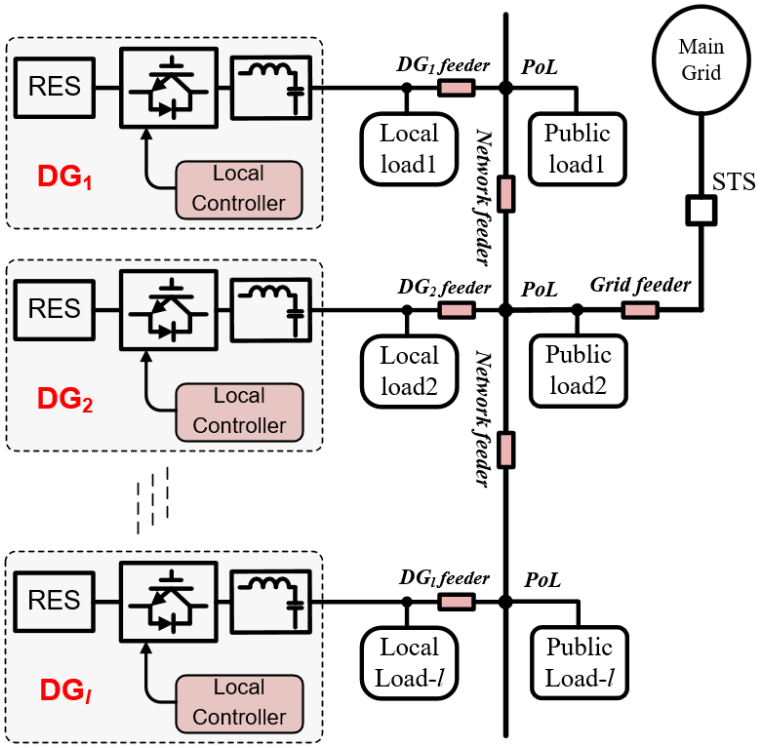

Figure 1.4: Configuration of a meshed microgrid.

or looped), as shown in Fig. 1.4 [19, 20, 34, 35]. A meshed system has a variable structure because the load and DG conditions change frequently [36]. This makes it difficult to achieve accurate reactive power sharing by considering only traditional factors, such as DG output impedances, mismatched feeder impedances, and mismatched local loads. In [18], an enhanced power sharing strategy was introduced that detected the reactive power sharing error. That said, it is difficult to detect the reactive power error, and accurate reactive power sharing cannot be achieved if the load demand changes. For accurate power sharing, some virtual impedance based methods have been introduced [34, 37–40]. In [37], an optimized virtual impedance controller was developed to eliminate the reactive power sharing error in a meshed microgrid based on exact knowledge of the detailed microgrid configuration. However, this method is not effective when the microgrid structure changes. Authors in [34] achieved proportional power sharing in a meshed microgrid by regulating the virtual resistance with complex impedances. However, the robustness of the controller is not guaranteed clearly when local load or microgrid structure changes. In [38] and [39], a distributed virtual impedance control scheme was proposed to solve the inaccurate power sharing problem in the microgrids. Even though the reactive power sharing performance is improved significantly, the virtual impedance regulator becomes very complicated due to many controller gains. Recently, based on the helps of low-

bandwidth communication links (LBCs) and a microgrid central controller (MGCC), an adaptive virtual impedance scheme was developed in [40]. This method is effective for single-bus microgrids and is inherently immune to delays in the communication links. However, it does not consider the different offsets of the local loads or changes of the microgrid structure. Also, the virtual resistance and reactance are regulated equally, even though their effects on regulating the DG reactive power are different.

1.2.1.2 Inaccurate Harmonic Power Sharing

Similar to reactive power sharing situation, when nonlinear loads extensively used in the microgrid system, the harmonic load power is distributed among DGs according to the feeder impedances. Unfortunately, because the feeder impedances are normally mismatched, the harmonic load power is poorly shared which may trigger the current protection or lead to overloads of DG units.

Even though many real and reactive power sharing methods have been developed, the harmonic power sharing for meshed microgrids is not fulfilled sufficiently until now. Some methods developed for the single-bus systems in [23,39,41] might be applied to the meshed microgrids because the feeder impedance information is not required. In [41], a harmonic droop-based technique was developed by using the voltage value at the point of common coupling (PCC). However, it is not easy to detect the PCC voltage because it is usually far from the controllers. In [23], the reactive, imbalance, and harmonic power sharing performance were enhanced by regulating the virtual impedances at the fundamental and selected dominant harmonic frequencies. However, the accurate power sharing cannot be achieved if the load changes during virtual impedance regulation. More recently, Zhang et al. [39] achieved both the accurate fundamental and harmonic power sharing by a distributed virtual impedance control method based on the well-known consensus algorithm. Nevertheless, the virtual impedance regulator becomes very complicated due to many controller gains.

1.2.2 Frequency and Voltage Magnitude Deviations

It can be seen from (1.1) and (1.2), the angular frequency and voltage magnitude seriously depend on the load power, which causes wide deviations, and the frequency and voltage deviations become more severe as the load demand increases. These deviations significantly decrease the microgrid voltage quality.

In order to solve the deviation problems, the centralized control method (CCM) has been conventionally adopted with the aid of communication links and a microgrid central controller (MGCC) [19, 20, 25, 34, 40, 42–44]. However, the CCM shows some significant

limitations. First, the CCM needs a MGCC and point-to-point communication links between the MGCC and all DG units. Therefore, the entire secondary control functionality is lost if the MGCC or any communication link fails. Furthermore, the cost and complexity of the system are high because the CCM requires additional sensors and a phase-locked-loop (PLL) to detect the frequency and voltage magnitudes at the point of common coupling (PCC). Another issue is that a communication link must be established between any new DG unit and the MGCC when connecting the unit to the microgrid system. This situation is inflexible in terms of possible expansions. Lastly, the MGCC is required to collect information from all DG units and handle huge amounts of data, so it might suffer from overload as the number of DGs increases.

To overcome these problems, the distributed control method (DCM) has been developed recently [45–51]. However, to generate suitable compensating signals, conventional DCM needs PI-type controllers in the DG local controller and additional information such as the frequency and voltage magnitude of its neighbors, which increase the computational burden and complexity.

1.2.3 Highly Distorted PCC Voltage

Besides inaccuate harmonic power sharing problem, the PCC voltage becomes highly distorted when nonlinear loads are extensively used in the microgrid system.

In order to share the harmonic load power and attenuate the PCC voltage harmonics, an individual harmonic droop controller was presented [52], but the impact of the feeder impedance was not considered. In another work, a virtual capacitive impedance was used to compensate for the harmonic voltage drop across the inductive feeder impedance and attenuate the PCC voltage harmonics [53]. Nevertheless, this method requires information about the feeder impedances. To avoid this issue, an enhanced hierarchical control structure was proposed with the aid of communication links [54–57], where an additional control loop was implemented for PCC voltage quality improvement. However, the control system is complex due to the many control loops and Park/Inverse Park transformation. To reduce the complexity of the control system, a harmonic droop control loop was used in addition to a distributed consensus-based virtual impedance control loop, and accurate harmonic power sharing was achieved together with improved PCC voltage quality [39]. However, this method cannot guarantee that PCC voltage quality complies with the IEEE 519-1992 standard (total harmonic distortion (THD) $< 5\%$) [58]. PCC voltage harmonics can be attenuated by reducing the DG equivalent feeder impedances [59], and accurate harmonic power sharing with high PCC voltage quality was achieved by means of a harmonic droop controller to regulate the DG equivalent feeder impedance by using the

instantaneous PCC voltage [41]. Nevertheless, it is inconvenient to send the non-dc signal from MGCC to DGs through low bandwidth communication links.

1.3 Research Objectives

The main aim of this thesis is to solve problems related to the power sharing and voltage quality in droop-controlled islanded microgrids. After an introductive description of the microgrid paradigm, some of control objectives are proposed to accurately share linear and nonlinear loads among DGs; eliminate deviations of the frequency and voltage magnitude; and compensate for PCC voltage harmonics in islanded microgrids. The research methodology will be developed as follows:

- Advanced control strategies to provide accurate active, reactive, and harmonic power sharing in islanded microgrid systems regardless of microgrid structure. The control strategies are simple and easy to implement without any knowledge of the detailed microgrid configuration or line impedances.

- Simple control strategies to eliminate the frequency and voltage magnitude deviations due to the droop operation. The strategies does not require additional PCC voltage measurement and PI-type controller at MGCC or DG local controllers.

- Enhanced control strategies to compensate PCC voltage harmonics so as to guarantee the PCC voltage quality to comply with the standard IEEE 519-1992 (THD $< 5\%$). The control strategies are simple and easy to implement without need for information of line impedances.

1.4 Contributions of the Thesis

From aforementioned research objectives, theoretical analyses, simulations using PSIM, and experiments with scaled-down microgrid prototypes have been done in this thesis to demonstrate advanced features of the proposed control methods. The main contributions of the thesis are as follows:

- Development of an enhanced adaptive virtual impedance control scheme, which can effectively eliminate the reactive-power-sharing error in a meshed microgrid without any estimation algorithm regardless of the microgrid configuration and load changes. The proposed method is directly and easily implemented in any type of microgrid topology (single-bus or meshed system) without the need for any information, such

as the microgrid structure, feeder impedances, or load powers. Of particular importance, the reactive power is shared accurately even when the load condition or microgrid structure changes during the virtual impedance regulation.

- Development of a simplified and accurate control scheme to realize accurate power sharing and restoration of the frequency and voltage magnitude for islanded microgrids using distributed cooperative control. The strategy realizes accurate power sharing with a very simple DG virtual impedance regulator regardless of load condition variations, and detailed guidelines are provided to design a DG virtual impedance controller. The conventional droop equations are modified to eliminate the frequency and voltage deviations by using only neighbors' droop information without PCC voltage information or PI controllers in either the MGCC or DG units. The stability is theoretically evaluated according to the communication delay using a small-signal state-space model, and the scheme is validated through digital simulation and experiment.

- Development of an enhanced power sharing control scheme for the meshed microgrids together with the elimination of the frequency and voltage magnitude deviations. Harmonic power sharing in a meshed microgrid is analyzed, and then, the harmonic power sharing errors are eliminated irrespective of the load variation or the microgrid configuration change by means of the adaptive regulation of the virtual impedances at the dominant harmonic frequencies. Additionally, a simple centralized secondary controller is developed to remove the frequency/voltage deviations without detection of PCC voltage. The PI controller used to generate compensating signal for frequency is removed. Therefore, the system cost is reduced, and the control system becomes very simple.

- Development of an enhanced virtual harmonic impedance control scheme that can always guarantee accurate harmonic power sharing with high PCC voltage quality (THD $< 5\%$) for islanded microgrids, regardless of the load conditions. Specifically, the DG virtual impedance at a selected dominant harmonic frequency is directly regulated through two controllable parts. The first one is adjusted to eliminate the harmonic power sharing errors, and the second part is a negative impedance to attenuate the PCC voltage harmonics by reducing the DG equivalent feeder impedance. As a result, accurate harmonic power sharing and voltage harmonic compensation can be achieved simultaneously with only one virtual impedance control loop, which makes the control system simple.

1.5 Outline of the Thesis

The thesis is organized in 5 chapters, as follows:

- **Chapter 1** introduces the concept of microgrid and surveys the past work related to power sharing, frequency and voltage magnitude restoration, and PCC voltage harmonic compensation. Then, objectives and contributions of the research work are outlined.
- **Chapter 2** presents enhanced adaptive virtual impedance control schemes based on centralized approach or distributed approach to eliminate the reactive power sharing error in islanded microgrids regardless of microgrid structure. The proposed controller are theoretically investigated and validated via simulation and experiment.
- **Chapter 3** introduces an enhanced power sharing control scheme to share accurately dominant harmonic powers for meshed microgrids with the aid of adaptive regulation of the virtual impedances at dominant frequencies. Theoretical analysis and simulation and experimental results are also provided.
- **Chapter 4** presents an enhanced virtual harmonic impedance control scheme to compensate for the PCC voltage harmonics with accurate harmonic power sharing in islanded microgrids. Theoretical analysis and simulation and experimental results are also provided in detail.
- **Chapter 5** concludes the works in this thesis. Also, future works are mentioned to open some new topics on the AC microgrid and its applications.
- **Appendix A** shows state matrices in Chapter 2.
- **Appendix B** shows state matrices in Chapter 4.
- **Appendix C** shows the list of publications.

Chapter 2

Accurate Active and Reactive Power Sharing Strategies

In this chapter, enhanced power sharing control schemes based on centralized approach or distributed approach are developed to share active and reactive power accurately in a meshed microgrid, with the aid of adaptive regulation of the virtual impedances. The proposed control methods always achieve accurate power sharing even when the microgrid configuration or the load condition is changed. Furthermore, the proposed control strategy can be implemented directly without any knowledge of the detailed microgrid configuration or the required load power measurement, which decreases the complexity and cost of the system. The proposed control is theoretically investigated and its feasibility and effectiveness are validated via simulation and experiment.

2.1 Centralized Power Sharing Control Strategy

2.1.1 Operating Principle of an Islanded Microgrid

2.1.1.1 Microgrid Operation

As DG units or loads are connected to or disconnected from the microgrid at various points, it is convenient to consider the traditional single-bus microgrid configuration as a meshed form. In Fig. 2.1 shows the configuration of a meshed microgrid composed of a number of DG units and loads. In Fig. 2.1, a load connected directly to a DG unit is called a local load, and one connected to a system at the point of load (PoL) is called a public load. Based on the operating information exchanged between the MGCC and DG units through low-bandwidth communication links, the microgrid can be operated in grid-connected mode or islanded mode by controlling the static transfer switch (STS) at the PCC.

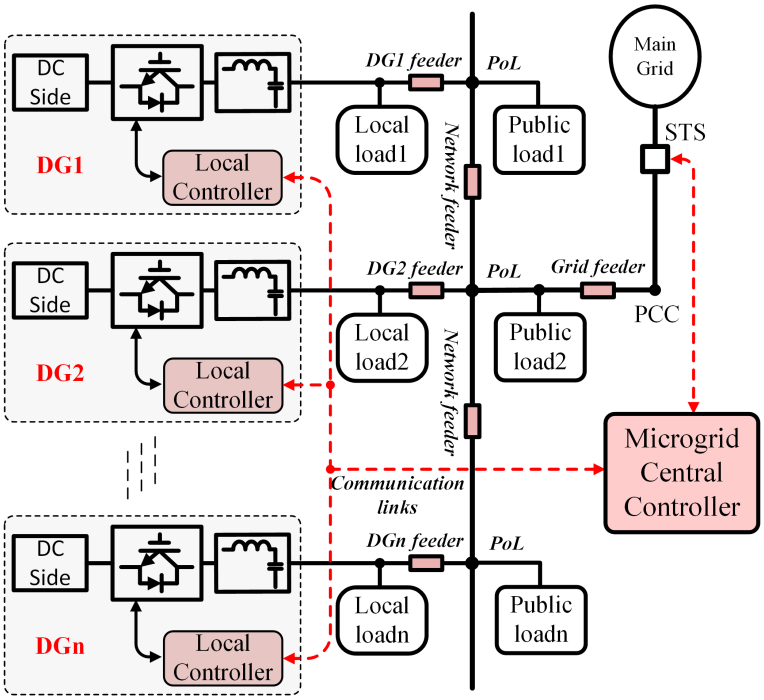

Figure 2.1: Configuration of the meshed microgrid.

During islanded operation, each DG unit can be operated via the conventional droop controller in which the angular frequency and voltage magnitude of the DG output are given as follows, respectively:

$$\omega = \omega_0 - mP, \tag{2.1}$$

$$E = E_0 - nQ, \tag{2.2}$$

where ω_0 and E_0 are the nominal values of the DG angular frequency and DG voltage magnitude, respectively; P and Q are the measured real and reactive powers after the low-pass filter (LPF), respectively; and m and n are the real and reactive power droop slopes, respectively. From (2.1) and (2.2), the instantaneous voltage reference V_{refi} is given as [17, 18]:

$$V_{refi} = E_i sin\left(\int \omega_i dt\right). \tag{2.3}$$

2.1.1.2 Reactive Power-Sharing Analysis

For a simple analysis, the meshed microgrid in Fig. 2.1 is simplified using two DG units having the same power rating, as shown in Fig. 2.2, and their voltage magnitudes E_1 and

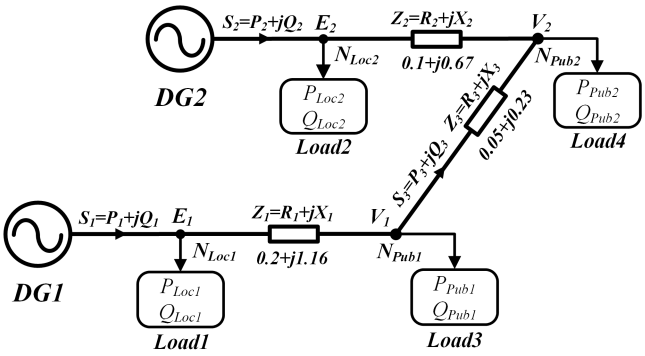

Figure 2.2: Meshed microgrid with two DGs.

E_2 are given in (2.4) and (2.5), respectively, from (2.2):

$$E_1 = E_0 - nQ_1, \tag{2.4}$$

$$E_2 = E_0 - nQ_2, \tag{2.5}$$

where Q_1 and Q_2 are the output reactive powers of DG1 and DG2, respectively.

When the power $S = P + jQ$ is delivered through the line impedance $Z = R + jX$, the voltage drop ΔV due to the line impedance is given approximately as [18, 36]

$$\Delta V \approx \frac{XQ + RP}{E_0}. \tag{2.6}$$

From Fig. 2.2, the voltages at the local loads become

$$E_1 = V_1 + \frac{X_1 (Q_1 - Q_{Loc1}) + R_1 (P_1 - P_{Loc1})}{E_0}, \tag{2.7}$$

$$E_2 = V_2 + \frac{X_2 (Q_2 - Q_{Loc2}) + R_2 (P_2 - P_{Loc2})}{E_0}, \tag{2.8}$$

and the voltage difference between public loads is

$$V_1 - V_2 = \frac{X_3 Q_3 + R_3 P_3}{E_0}. \tag{2.9}$$

When the active load power is shared accurately between the DG units by the droop controller, the active powers of DG1 and DG2, P_1 and P_2, respectively, are calculated as follows by neglecting the feeder loss:

$$P_1 = P_2 = \frac{1}{2} P_{total} = \frac{1}{2} (P_{Loc1} + P_{Loc2} + P_{Pub1} + P_{Pub2}). \tag{2.10}$$

Table 2.1: Sensitivity of ΔQ_{12} with respective to the change in the real and reactive powers.

Symbol	$\frac{\partial \Delta Q_{12}}{\partial Q_{Loci}}$	$\frac{\partial \Delta Q_{12}}{\partial Q_{Pubi}}$	$\frac{\partial \Delta Q_{12}}{\partial P_{Loci}}$	$\frac{\partial \Delta Q_{12}}{\partial P_{Pubi}}$
$i = 1$	0.74	-0.09	0.13	-0.02
$i = 2$	-0.74	-0.26	-0.13	-0.05

By considering the power balancing at the nodes, N_{Pub1} and N_{Pub2}, the following relationships are obtained:

$$Q_3 = Q_1 - Q_{Loc1} - Q_{Pub1} = Q_{Pub2} + Q_{Loc2} - Q_2, \tag{2.11}$$

$$P_3 = P_1 - P_{Loc1} - P_{Pub1} = P_{Pub2} + P_{Loc2} - P_2. \tag{2.12}$$

From (2.4) through (2.12), the reactive-power-sharing error ($\Delta Q_{12} = Q_1 - Q_2$) finally becomes

$$\begin{aligned}\Delta Q_{12} =& Q_1 - Q_2 \\ =& \frac{X_1 + X_2 + X_3}{X_1 + X_2 + X_3 + 2nE_0}(Q_{Loc1} - Q_{Loc2}) + \frac{X_2 - X_1}{X_1 + X_2 + X_3 + 2nE_0}(Q_{Pub1} + Q_{Pub2}) \\ &+ \frac{X_3}{X_1 + X_2 + X_3 + 2nE_0}(Q_{Pub1} - Q_{Pub2}) + \frac{R_1 + R_2 + R_3}{X_1 + X_2 + X_3 + 2nE_0}(P_{Loc1} - P_{Loc2}) \\ &+ \frac{R_2 - R_1}{X_1 + X_2 + X_3 + 2nE_0}(P_{Pub1} + P_{Pub2}) + \frac{R_3}{X_1 + X_2 + X_3 + 2nE_0}(P_{Pub1} - P_{Pub2}).\end{aligned} \tag{2.13}$$

As can be seen in (2.13), the reactive-power-sharing error depends on the following factors: line impedances (Z_1, Z_2, and Z_3), load positions ($X_2 - X_1$, $R_2 - R_1$), mismatched local loads ($Q_{Loc1} - Q_{Loc2}$), and mismatched public loads ($Q_{Pub1} - Q_{Pub2}$). Table 2.1 provides the sensitivities of the reactive power error ΔQ_{12} according to the load power change ($n = 0.00165, E_0 = 220V$). As shown in the table 2.1, for conventional droop control, the sensitivity due to the reactive power change is much higher than that due to the active power change, which means that the reactive-power-sharing error becomes more vulnerable when the reactive power changes. Additionally, the reactive power of the local load has a stronger impact on the reactive-power-sharing error than does that of the public load.

2.1.1.3 Virtual Impedance for Reactive Power Sharing

To improve the power control stability and power sharing accuracy, virtual impedance was introduced [26, 30]. When the virtual impedance is added to the output impedance of a DG, the reactive-power-sharing error is modified from (2.13) as follows:

$$\begin{aligned}\Delta Q_{12} = Q_1 - Q_2 =& \frac{\left[(X_2 + X_{v2}) - (X_1 + X_{v1})\right] Q_{total} + \left[(R_2 + R_{v2}) - (R_1 + R_{v1})\right] P_{total}}{X_1 + X_2 + X_3 + X_{v1} + X_{v2} + 2nE_0} \\ &+ \frac{2\left[(X_1 Q_{Loc1} + R_1 P_{Loc1}) - (X_2 Q_{Loc2} + R_2 P_{Loc2})\right]}{X_1 + X_2 + X_3 + X_{v1} + X_{v2} + 2nE_0} \\ &+ \frac{\left[(Q_{Loc1} + Q_{Pub1}) - (Q_{Loc2} + Q_{Pub2})\right] X_3}{X_1 + X_2 + X_3 + X_{v1} + X_{v2} + 2nE_0} \\ &+ \frac{\left[(P_{Loc1} + P_{Pub1}) - (P_{Loc2} + P_{Pub2})\right] R_3}{X_1 + X_2 + X_3 + X_{v1} + X_{v2} + 2nE_0}.\end{aligned} \tag{2.14}$$

where the virtual impedances of DG1 and DG2 are $Z_{v1} = R_{v1} + jX_{v1}$ and $Z_{v2} = R_{v2} + jX_{v2}$, respectively. To make the line impedances equal in Fig. 2.2, the virtual impedances for the two DGs are assigned opposite signs: $Z_{v1} = -Z_{v2}$. Additionally, we keep the resistive and reactive component ratio at 5 because X_v should be designed much larger than R_v to maintain the microgrid system stability [36,37]. Then, the virtual impedances to eliminate the reactive-power-sharing errors are

$$\begin{aligned} X_v &= X_{v1} = -X_{v2}, \\ R_v &= R_{v1} = -R_{v2} = \frac{X_v}{5}. \end{aligned} \tag{2.15}$$

By substituting (2.15) into (2.14), X_v is obtained as (2.16):

$$\begin{aligned} X_v =& \frac{(X_2 - X_1) Q_{total} + (R_2 - R_1) P_{total}}{2Q_{total} + \frac{2}{5} P_{total}} + \frac{(X_1 Q_{Loc1} + R_1 P_{Loc1}) - (X_2 Q_{Loc2} + R_2 P_{Loc2})}{Q_{total} + \frac{1}{5} P_{total}} \\ &+ \frac{\left[(Q_{Loc1} + Q_{Pub1}) - (Q_{Loc2} + Q_{Pub2})\right] X_3}{2Q_{total} + \frac{2}{5} P_{total}} + \frac{\left[(P_{Loc1} + P_{Pub1}) - (P_{Loc2} + P_{Pub2})\right] R_3}{2Q_{total} + \frac{2}{5} P_{total}}. \end{aligned} \tag{2.16}$$

and R_v is determined from the component ratio in (2.15).

2.1.2 Proposed Control Scheme

To improve the power-sharing performance by using the virtual impedance, some information is needed, such as the feeder impedances, detailed microgrid structure, and load powers. Unfortunately, this information is not easily available and it is generally time

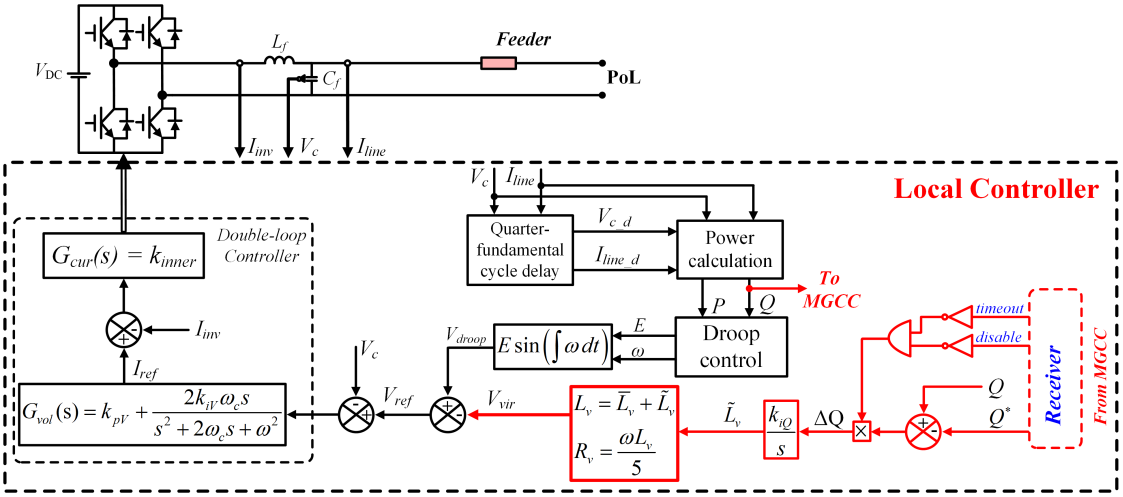

Figure 2.3: Proposed local control scheme.

variable. Furthermore, detection of the feeder impedances increases the computational burden on DG local controllers, and the measurement of loads power increases the cost and complexity of the system. To remove these problems, this section presents an adaptive virtual impedance control method based on centralized control approach.

For general applications, we consider a meshed microgrid with n DG units to describe the proposed control algorithm instead of the microgrid with two DG units shown in Fig. 2.2. As shown in Fig. 2.1, the meshed microgrid is composed of two controllers, the MGCC and the local controller. These two controllers are implemented without using the information of the feeder impedances and the loads.

2.1.2.1 Microgrid Central Controller

The DG units transmit the information of the respective reactive powers (Q_1, Q_2, ..., and Q_n) to the MGCC, as shown in Fig. 2.1. At the MGCC, based on the DG reactive powers and the voltage droop slopes (n_1, n_2, ..., and n_n), the reactive power demand for the i^{th} DG unit to achieve accurate reactive power sharing is calculated as follows:

$$Q_i^* = h_i Q_{total}, \quad i = 1, \cdots, n \tag{2.17}$$

where h_i is the reactive load power distribution factor defined as

$$h_i = \frac{n_i^{-1}}{\sum_{j=1}^{n} n_j^{-1}}; \qquad \sum_{i=1}^{n} h_i = 1. \tag{2.18}$$

From (2.17) and (2.18), the power reference Q_i^* is determined according to the total

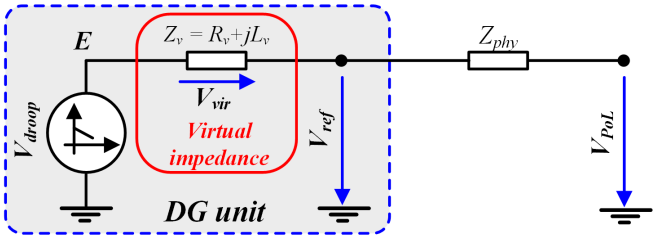

Figure 2.4: Model of DG unit with virtual impedance.

reactive power, and it is periodically sent to the corresponding DG unit.

2.1.2.2 Local Controller

Fig. 2.3 shows the local controller, which has three main control parts to generate the desired voltage reference for the DG unit: power control, adaptive virtual impedance control, and a double-loop voltage tracking scheme.

Power Control: In flexible microgrid operation, a plug-and-play load or DG unit can be connected to any point in the microgrid at any time. By adding a derivative term to the original droop controller in (2.1) and (2.2), the start-up transients and circulating currents between DGs can be reduced [60, 61]:

$$\begin{aligned} \omega &= \omega_0 - mP - m_d \frac{dP}{dt}, \\ E &= E_0 - nQ - n_d \frac{dQ}{dt}, \end{aligned} \tag{2.19}$$

where m_d and n_d are coefficients chosen using the pole placement method.

Adaptive Virtual Impedance Control: Fig. 2.4 shows a model of a DG unit with virtual impedance. To preserve the inductive equivalent feeder impedance and enhance the system stability, the virtual impedance L_v is regulated around its nominal value [23]:

$$L_v = \bar{L}_v + \tilde{L}_v \tag{2.20}$$

where $\bar{L}_v$ is a nominal inductance, and $\tilde{L}_v$ represents its perturbation. $\tilde{L}_v$ is adjusted to completely eliminate the reactive-power-sharing errors:

$$\tilde{L}_v = \frac{k_{iQ}}{s} (Q - Q^*) \tag{2.21}$$

where k_{iQ} is the integral gain to adjust the virtual inductance. Then, the reactive part of the virtual impedance is determined from (2.20) and (2.21), and the resistive part is obtained from the relationship in (2.15):

$$\begin{aligned} L_v =& \bar{L}_v + \frac{k_{iQ}}{s}\left(Q - Q^*\right), \\ R_v =& \frac{\omega L_v}{5}. \end{aligned} \tag{2.22}$$

From Fig. 2.4, the voltage drop V_{vir} due to the virtual impedance becomes

$$V_{vir} = R_v I_{line} - \left(\omega L_v\right) I_{line\_d} \tag{2.23}$$

where I_{line} and I_{line_d} are the DG line current and its delayed component for a quarter fundamental cycle, respectively. Then, the voltage reference V_{ref} for the voltage control loop is obtained as

$$V_{ref} = V_{droop} - V_{vir} = V_{droop} - \left(R_v I_{line} - \omega L_v I_{line\_d}\right). \tag{2.24}$$

Double-Loop Voltage Tracking Scheme: With the voltage reference V_{ref} in (2.24), the double-loop voltage controller in Fig. 2.3 is applied to generate the desired output voltage. In the double-loop voltage controller, the outer loop uses a non-ideal proportional–resonant (PR) controller tuned at the fundamental frequency [21]:

$$G_{Vol}(s) = k_{pv} + \frac{2k_{iv}\omega_c s}{s^2 + 2\omega_c s + \omega_{DG}^2} \tag{2.25}$$

where k_{PV} is the outer loop proportional gain, kiV is the resonant controller gain at the fundamental frequency, and ω_c is the cutoff frequency of the resonant controller. The inner loop has a simple proportional control gain k_{inner} with the filter inductor current feedback, which provides sufficient damping to the output LC filter [21]:

$$G_{Cur}(s) = k_{inner}. \tag{2.26}$$

2.1.2.3 Communication Links Faults

In the case of a communication fault between the i^{th} DG unit and the MGCC, the controller at the MGCC stops updating the DG measured powers, and a binary signal "disable" is sent to all DG units in order to disable the virtual impedance update, as shown in Fig. 2.3. Simultaneously, at the i^{th} DG local controller, a binary signal "timeout" is

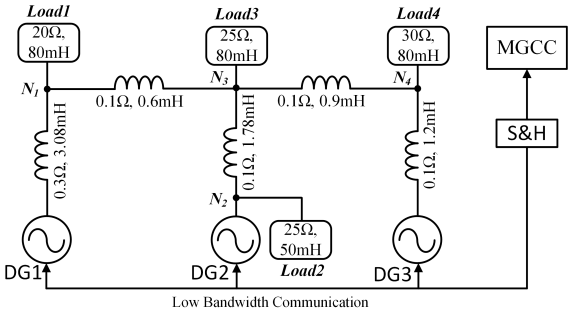

Figure 2.5: Meshed microgrid used in the simulation.

used to disable the virtual impedance regulation ($\Delta Q = 0$). Consequently, the virtual impedance value is retained with the last regulated one until the communication link is restored, and all units continue to operate with the latest virtual impedance.

2.1.3 Simulation Results

We simulated a meshed microgrid with PSIM to validate the proposed control strategy. To show that the control scheme developed for two DG units can be extended to n DG units, we added one more DG to the meshed microgrid shown in Fig. 2.2, and used this configuration in the simulation, as shown in Fig. 2.5. The system parameters used in the simulation are listed in Table 2.2. Data communication was activated every $10ms$, and the reactive power demand was updated every $50ms$.

For simple and easy comparison, we used a normalized reactive power error Q_{err_i} in (2.27):

$$Q_{err\_i} = \left| \frac{Q_i^* - Q_i}{Q_i^*} \right| \times 100\%. \tag{2.27}$$

2.1.3.1 Performance with Conventional Controller

Fig. 2.6 shows power sharing with the conventional droop controller when all DG units in Fig. 2.5 have same power ratings. During stage 1 ($0 < t < 6s$), the microgrid was originally operated with Load3 and Load4 at nodes N_3 and N_4, respectively (the others were disconnected). At $t = 6s$, Load1 was connected to node N_1, which not only invokes a step load change but also changes the microgrid structure. At $t = 9s$, Load2 was connected to node N_2 in order to investigate the performance when a local load was applied. At $t = 12s$ and $15s$, the DG3 was disconnected and reconnected, respectively.

In the steady state, the reactive power sharing shown in Fig. 2.6(a) exhibits poor performance, whereas Fig. 2.6(b) shows accurate active power sharing. Especially, when a local load Load2 is applied at $t = 9s$, the DG2 reactive power increases significantly,

Table 2.2: System Parameters.

System Parameter		Values		
		Simulation	Experiment	
LC filter, L_f/C_f		1.3mH / 10μF	1.3mH / 10μF	
DC link voltage, V_{DC}		300 V	200 V	
Nominal operating voltage, E_0		220 V, 60 Hz	110 V, 60 Hz	
Switching frequency, f_{sw}		10 kHz	10 kHz	
Power Control	**Coefficient**	**Same Power Ratings**	**Different Power Ratings**	
		DG_1=DG_2=DG_3	DG_1=DG_3	DG_2
P - ω	m (rad/W·s)	0.00145	0.00145	0.0029
	m_d (rad/W)	0.0003	0.0003	0.0003
Q - V	n (V/Var)	0.00165	0.00165	0.0033
	n_d (V·s /Var)	0.0001	0.0001	0.0001
Double-Loop Voltage Control Parameter		**Values**		
		Simulation	**Experiment**	
k_{pv}		0.1	0.1	
k_{iv}		30	30	
k_{inner}		20	20	
ω_c		4.1 Rad/s	4.1 Rad/s	
Virtual Impedance Control Parameter		**Values**		
		Simulation	**Experiment**	
$\bar{L}_{vir}$		1mH	1mH	
k_{iQ}		0.000035	0.000035	

which results in DG2 overloading. Moreover, there are large oscillations in the active and reactive powers of transient duration due to the large circulating currents. In Fig. 2.6(c), at Stage 1, the reactive-power-sharing errors Q_{err_i} are 58%, 10%, and 48% for DG1, DG2, and DG3, respectively. However, as Load1 is applied at $t = 6s$, the power-sharing errors decrease to 36% for DG1and 26% for DG3, despite the increased load power; this demonstrates that the microgrid structure significantly affects the power-sharing performance. In the most severe case, when local load Load2 is connected, the DG2 reactive-power-sharing error is sharply increased to 58% from 10%. As Fig. 2.6 shows, the reactive power cannot be shared equally using a conventional controller.

Fig. 2.7 shows the power-sharing performance of the centralized control scheme developed in [40], which is one of the most advanced centralized control scheme up to now, with the same network used in Fig. 2.6. At the beginning, the conventional method was applied under the exactly same operating condition as Stage 1 in Fig. 2.6. At $t = 3s$, the control method in [40] was activated with the same load power. At $t = 6s$, $9s$, $12s$, and $15s$, the load condition changes in the same scenarios as in Fig. 2.6. As can be seen in Fig. 2.7, the centralized method in [40] achieves accurate power-sharing in both active and the reactive powers under any load condition. However, the transient performance is poor when the local load (Load2) and DG3 are connected at $t = 9s$ and $15s$, respectively.

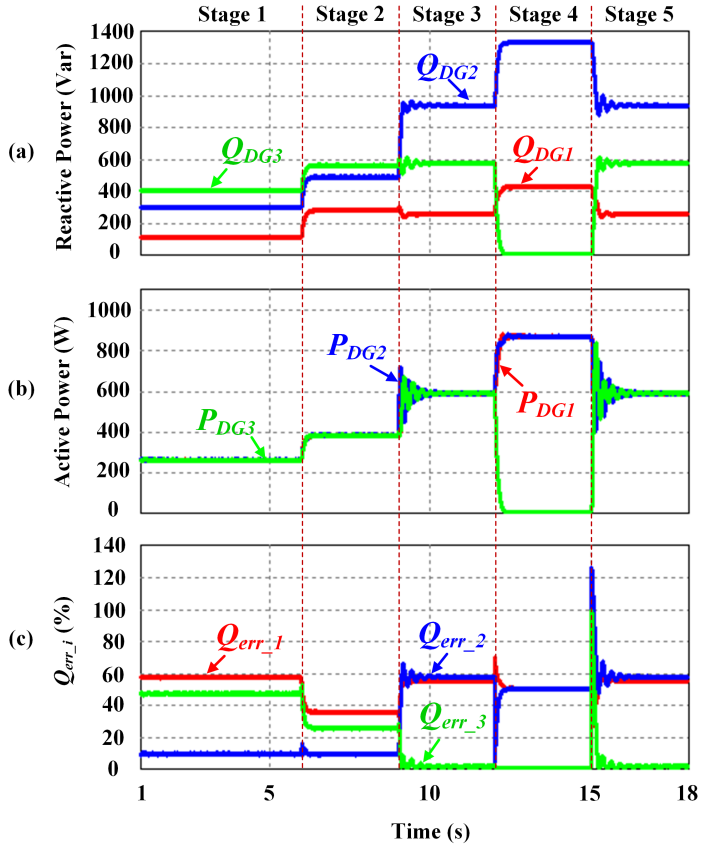

Figure 2.6: Simulated power sharing performance of the conventional droop control. (a) Reactive power. (b) Real power. (c) Q_{err_i} (%).

Particularly, there exist high overshoots and large oscillations in the transient states when active and reactive powers change in Figs. 2.7(a) and 2.7(b).

2.1.3.2 Performance with the Proposed Controller

Figs. 2.8 and 2.9 show the performance with the proposed control method when DG units in Fig. 2.5 have same and different power ratings, respectively. The operating and load conditions change in the same scenarios as in Fig. 2.7. Similar to the method in [40], when the proposed method is applied from $t = 3s$, the total reactive power demand is shared accurately among the DG units according to the DG power rating. This accurate power-sharing for both the active and the reactive powers is guaranteed under any load condition and microgrid configuration. As shown in the Figs. 2.8(a) and 2.8(b), there is no active power oscillation with only small reactive power overshoots in transient periods. Therefore, compared with performances in Figs. 2.6 and 2.7, the proposed method provides a superior transient performance. From Figs. 2.8(c), it is clear that the DG reactive-power-sharing errors are completely eliminated at the steady state

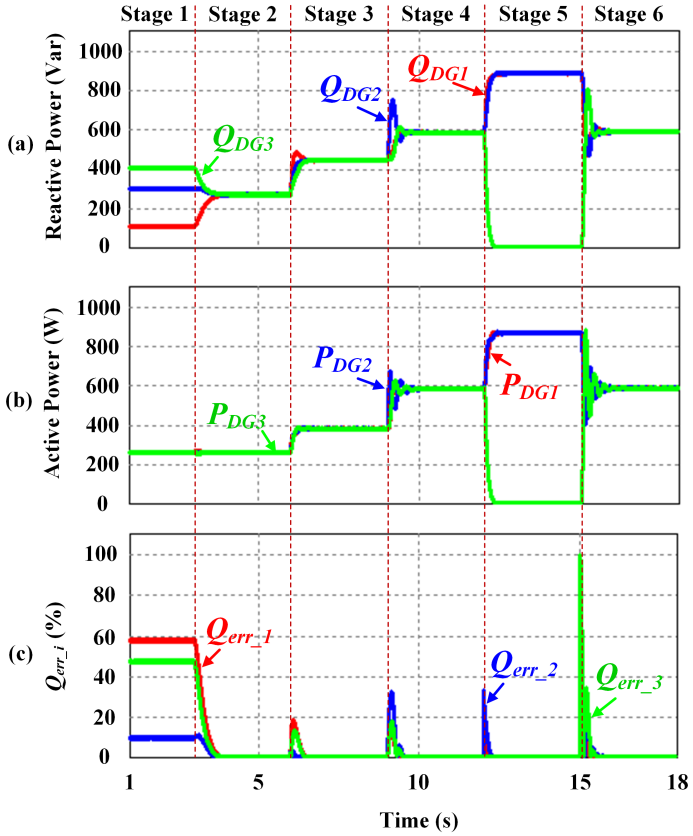

Figure 2.7: Simulated power sharing performance with the centralized control scheme. (a) Reactive power. (b) Real power. (c) Q_{err_i} (%).

when the proposed method is activated. Fig. 2.8(d) shows the variation of the virtual impedance in each DG unit: After the proposed control algorithm is applied at $t = 3s$, the DG virtual impedances are changed adaptively in order to share the reactive power equally.

Fig. 2.9, which shows the performance when DG units in Fig. 2.5 have different power ratings, also provides perfect reactive and active power sharing corresponding to each rated power.

Consequently, the proposed controller provides perfect reactive and active power sharing in both steady state and transient state regardless of DG power ratings and load conditions.

2.1.3.3 Control Performance during a Communication Disruption

The performance of the system during a communication interruption is shown in Fig. 2.10. When there was a communication fault in the meshed microgrid at $t = 6s$, all DG units stopped regulating their virtual impedances and continued to operate with the

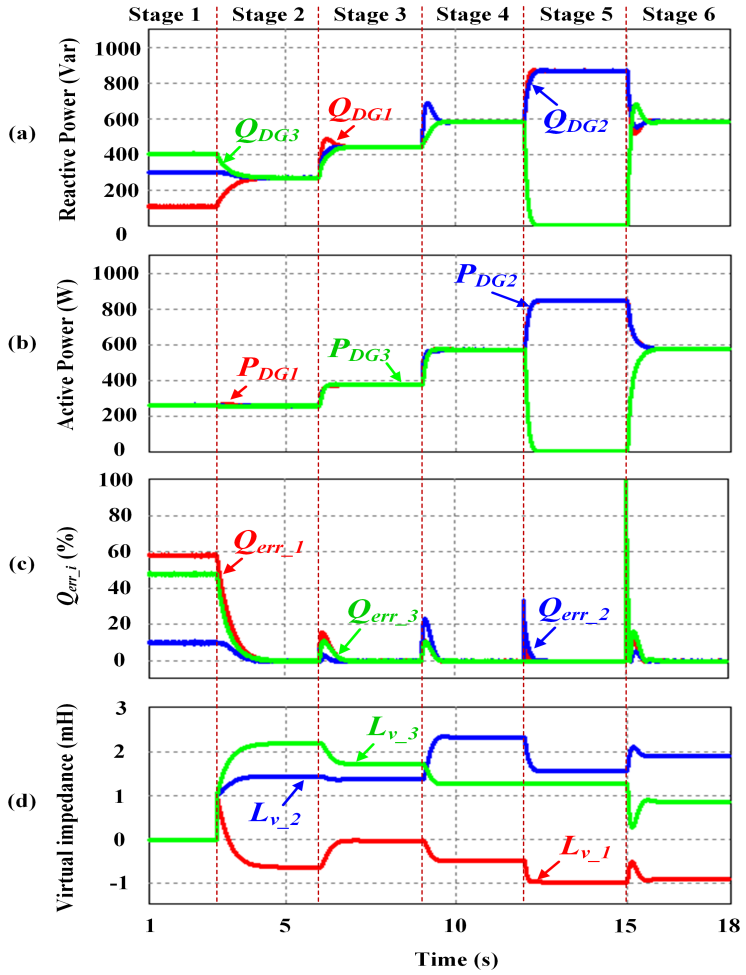

Figure 2.8: Simulated performance of the proposed controller with same DG units. (a) Reactive power. (b) Real power. (c) Q_{err_i} (%). (d) Variation of virtual inductance.

fixed virtual impedance obtained from the last regulation. From $6s$ to $9s$, there was no change in the system, as shown in Fig. 2.10. Then, accurate power sharing was maintained, despite the communication fault. On the other hand, when Load1 and Load2 were respectively connected to the system at $t = 9s$ and $t = 12s$, accurate power sharing no longer occurred; however, the power-sharing performance was better than with the conventional method, as shown in Fig. 2.6. At $t = 15s$, the communication was restored and the enhanced controller was reactivated. As shown in the figure, the reactive power sharing was recovered as the virtual impedance was properly regulated.

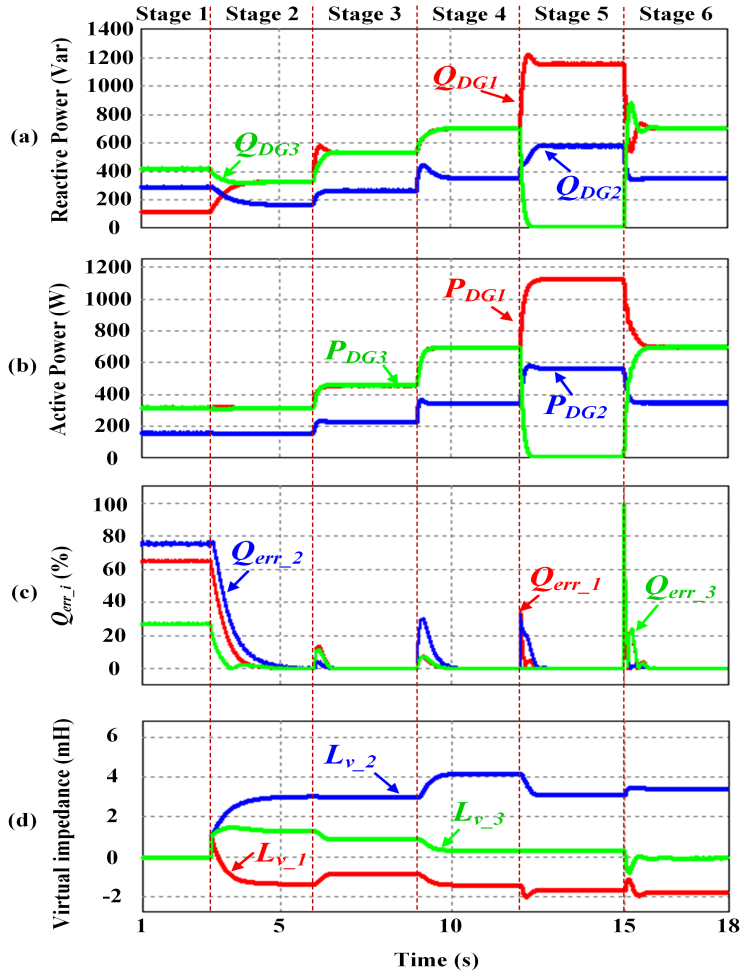

Figure 2.9: Simulated performance of the proposed controller with different DG units. (a) Reactive power. (b) Real power. (c) Q_{err_i} (%). (d) Variation of virtual inductance.

2.1.4 Experimental Varification

In the experiment, we used a simple down-scaled microgrid, shown in Fig. 2.11, to demonstrate the feasibility of the proposed control scheme. The system was controlled by the DSP (TMS320F28335) system. Data communication and the reactive power reference update rate were the same as in the simulation, and the other parameters were listed in Table 2.2.

2.1.4.1 Power-Sharing Performance

Fig. 2.12 shows the power-sharing performance with the proposed method for the same power ratings of two DG units in Fig. 2.11. At the start, the microgrid was controlled by the conventional droop controller with only Load1. As shown in Fig. 2.12, before $t = t_1$,

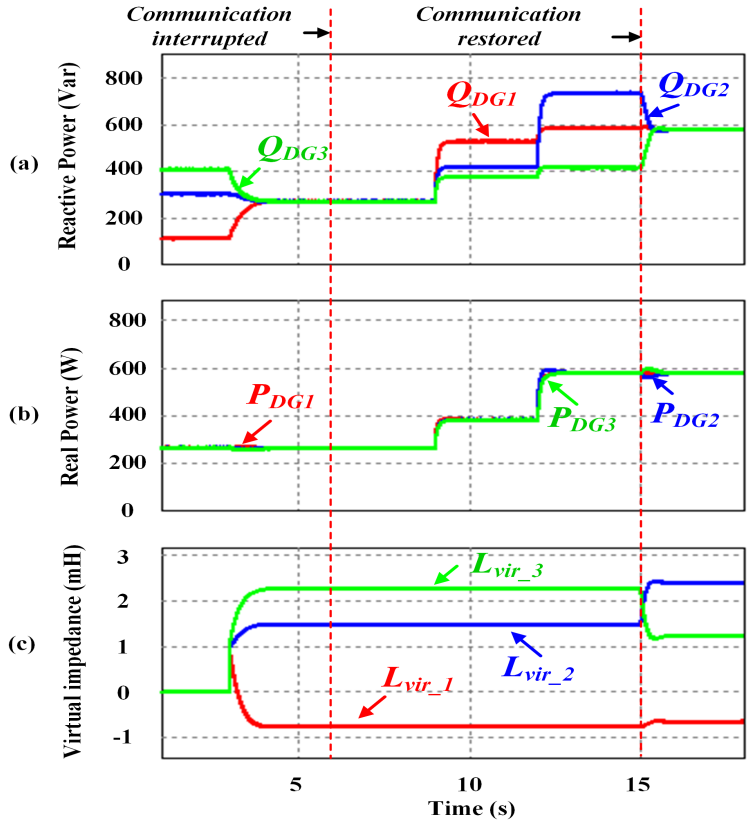

Figure 2.10: Simulated performance of the proposed controller before and after losing communications, and after recovering communication.

the reactive load power was not shared between two DG units. When the proposed method was activated at t_1, accurate reactive power sharing was achieved. Even when Load2 and Load3 were applied to the system at t_2 and t_3, respectively, which changed the microgrid configuration from a traditional single-bus to a meshed form, perfect reactive power sharing was always achieved, thanks to the proposed control scheme.

Fig. 2.13 shows the current-sharing waveforms corresponding to Fig. 2.12. Using the conventional method, the magnitude and phase of the DG currents were not the same. But they became nearly the same once the proposed method was utilized (Fig. 2.13(b)). Additionally, the DG currents were maintained with the same magnitudes even when the microgrid configuration was changed by applying a public load (Fig. 2.13(c)) or a local load (Fig. 2.13(d)).

Fig. 2.14 shows the control performance when a plug-and-play load was connected to the system during regulation of the virtual impedance. As shown in Fig. 2.14, the microgrid was originally operated with Load1 and Load2 using the conventional method. At t_4, the proposed method was activated, and Load3 was connected at t_5. As can be seen in Fig. 2.14, when the load was changed during the virtual impedance regulation,

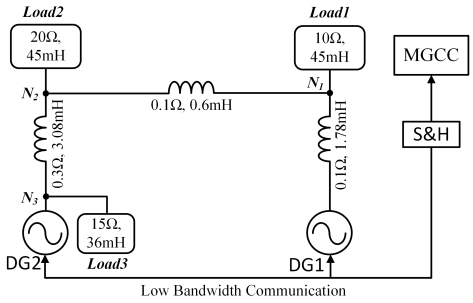

Figure 2.11: Meshed microgrid used in experiment.

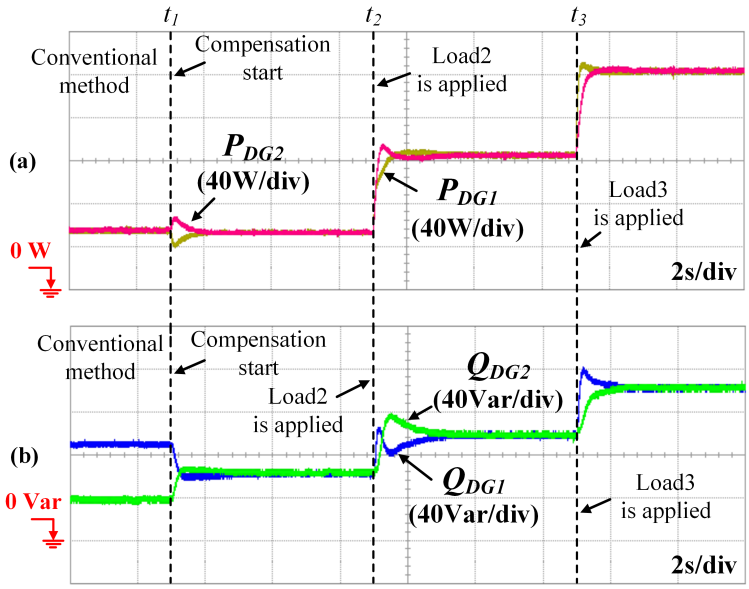

Figure 2.12: Experimental power sharing performance of the proposed controller with same DG units. (a) Real power. (b) Reactive power.

perfect reactive power sharing was maintained.

Fig. 2.15 shows the power-sharing performance with proposed method with different power rating for DGs in Fig. 2.11, and the waveforms are correspond to those in Fig. 2.12. We can see that, in spite of different power ratings, the proposed method shows a good performance similar to those with the same DG units.

2.1.4.2 Plug-and-Play Capability

To investigate the plug-and-play functionality, the load condition was changed sequentially. As shown in Fig. 2.16, the microgrid was originally operated with the same initial load condition as that shown in Fig. 2.12. The DG2 was disconnected at t_6, and reconnected at t_7. Then, Load3 was connected at t_8. As shown in Fig. 2.16, accurate reactive power sharing was always maintained in steady state when using the proposed method

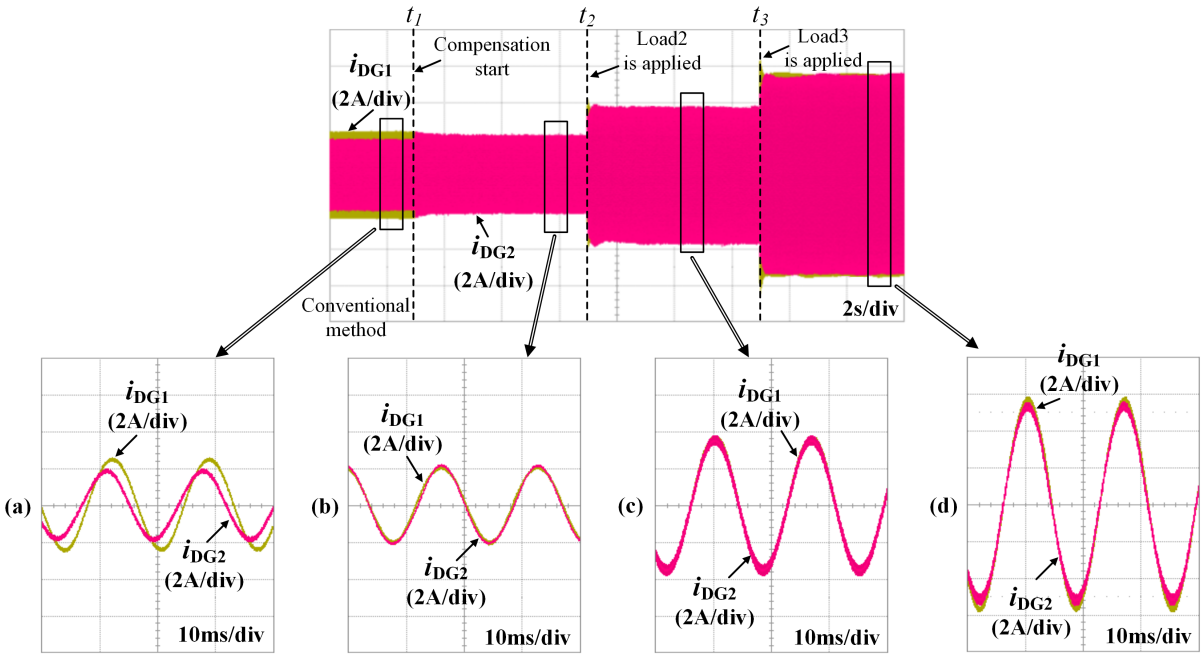

Figure 2.13: Zoom-in DG current waveforms with: (a) Conventional droop method; (b) Proposed method (activated at $t = t_1$); (c) Proposed method under load change operation (Load 1 is connected at $t = t_2$); (d) Proposed method under local load effect (Load 2 is connected $t = t_3$).

even with plug-and-play operation of a DG unit or load.

2.1.5 Conclusion of the Section

In this section, based on analysis of a meshed microgrid, an enhanced virtual impedance control scheme to achieve accurate active and reactive power sharing in a meshed microgrid has been proposed. The reactive component of the virtual impedance was adaptively regulated by using an integral controller, and the resistive component was obtained by maintaining a constant empirical virtual reactance-to-resistance ratio. With the proposed control scheme, accurate reactive power sharing is always achieved, even when the microgrid configuration or load conditions are changed during the regulating process. Furthermore, the proposed control strategy does not require any knowledge of the detailed microgrid configuration, feeder impedances, or load power information, making it highly suitable for complex meshed microgrid systems. The feasibility of the proposed scheme was demonstrated via simulation and experiment.

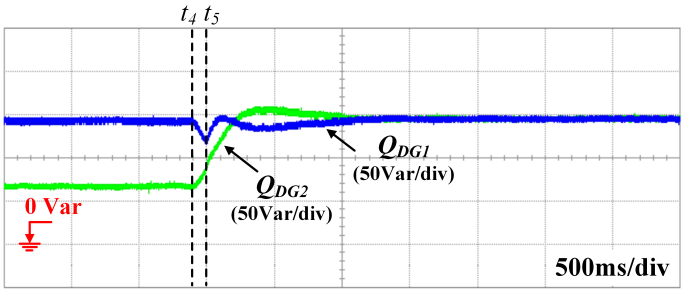

Figure 2.14: Experimental reactive power sharing performance of the proposed controller when a load change during regulating virtual impedance period.

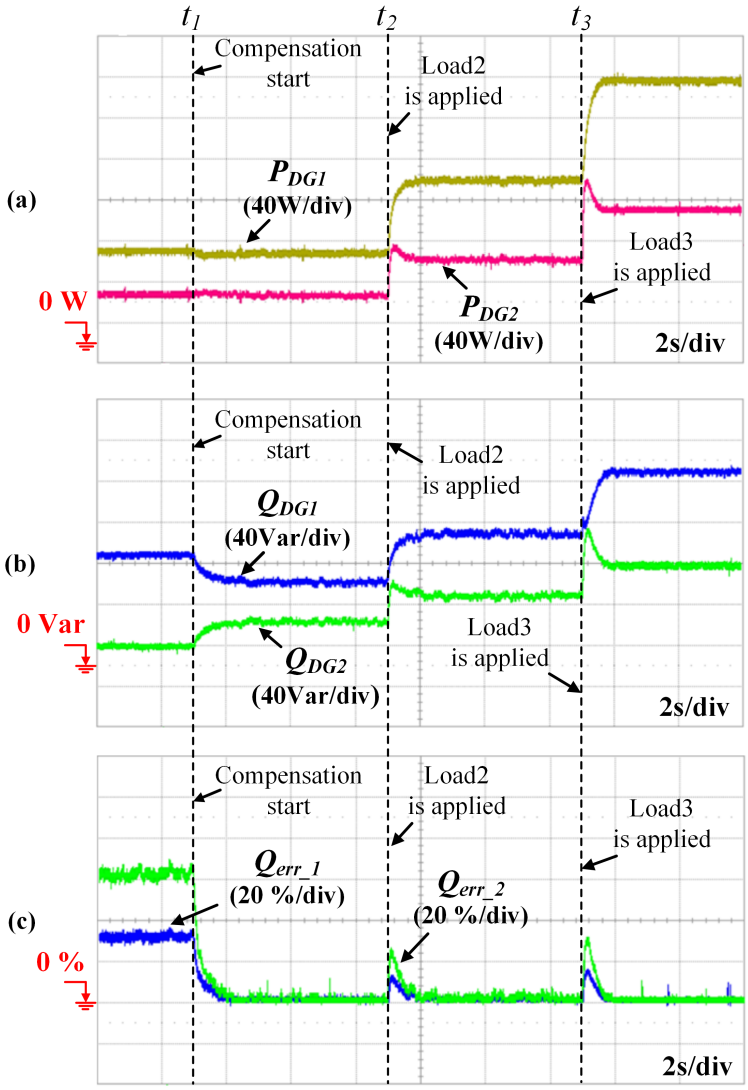

Figure 2.15: Experimental power sharing performance of the proposed controller with different DG units. (a) Real power. (b) Reactive power. (c) Q_{err_i} (%).

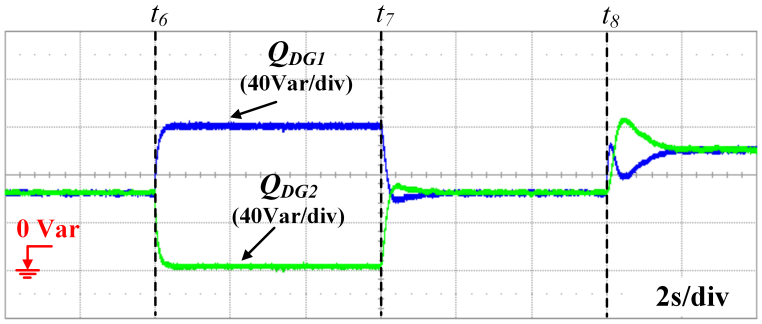

Figure 2.16: Experimental reactive-power-sharing performance under plug-and-play operation.

2.2 Distributed Power Sharing Control Strategy

This section presents a distributed control scheme for islanded microgrids to eliminate the power sharing errors and the frequency and voltage deviations based on distributed cooperative control. A consensus algorithm is developed through adaptive regulation of the virtual impedances for accurate power sharing regardless of the load variations. The proposed power sharing controller is quite easy to implement with only one simple integral gain without using information about the feeder impedances, load powers, or detailed microgrid structure. To remove the deviations in the frequency and voltage magnitude, conventional droop equations are enhanced by adding compensating signals, which are simply determined from the neighbors' droop information without any PI controller. Therefore, the control complexity is reduced significantly. The control performance is theoretically analyzed using a small-signal state-space model to evaluate the system dynamics and stability. A digital simulation is also done using PSIM, and experiments with a scaled-down microgrid prototype are done to verify the proposed scheme.

2.2.1 Preliminaries

2.2.1.1 Power Regulation Capability of Virtual Impedance

Fig. 2.17 shows an equivalent model of a DG unit interfaced to a load bus through a power feeder. The DG unit is represented as a combination of a controllable voltage source (V_{droopi}) and a series virtual impedance (X_{vi}). V_{oi} is the i^{th} DG's output voltage, and V_{PCC} is the PCC voltage. Generally, the feeder line impedance is inductive, and the line resistance can be ignored [22, 23]. The physical impedance between a DG unit and the PCC is described as X_i. In Fig. 2.17, the DG output reactive power can be changed by changing its virtual impedance X_{vi} [19, 20, 23]. Therefore, the DG reactive

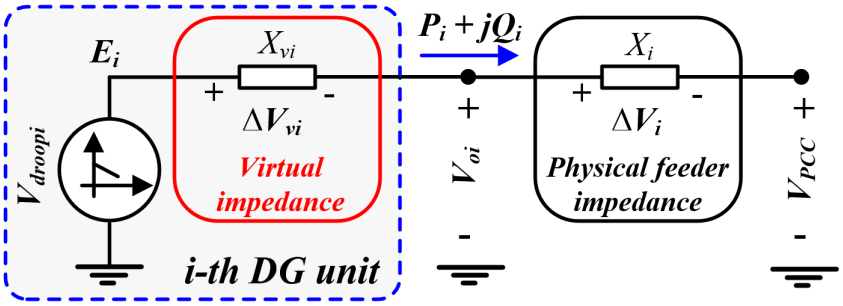

Figure 2.17: Model of a DG unit

power variation with respect to the DG virtual impedance change satisfies the following relationship:

$$\dot{Q}_i = -C_{XQi}\dot{X}_{vi} \tag{2.28}$$

where C_{XQi} is a positive coupling gain.

2.2.1.2 Consensus Control

In the distributed control scheme, all desired information is transferred through a sparse communication network. A diagram is shown on the right-hand side of Fig. 2.18. Based on graph theory [62], the sparse communication network is described by an undirected and connected graph $\Gamma = (\xi, \lambda)$ with a non-empty finite set of n DG nodes $\xi = 1, 2, \cdots, n$ and a set of undirected edges $\lambda \subseteq \xi \times \xi$. If there is a communication link between two nodes i and j, where $(i, j) \in \lambda$, these nodes are called communication neighbors.

Communication neighbors of the i^{th} node constitute the neighbor set $N_i = j \in \xi | (i, j) \in \xi$, and $|N_i|$ is its cardinality. The adjacency matrix of graph Γ is $A = (a_{ij})_{n\times n}$, with $a_{ij} = a_{ji} > 0$ if $(i, j) \in \lambda$; otherwise, $a_{ij} = 0$. The degree matrix of graph Γ is defined by $D = diag(d_i)_{n\times n}$ with $d_i = \sum_{j\in N_i} a_{ij}$ [62]. Thus, the Laplacian matrix $\mathscr{L} = (l_{ij})_{n\times n}$ of graph Γ is given by $\mathscr{L} = D - A$, which is a symmetric and positive semidefinite matrix.

For an undirected and connected graph, all eigenvalues of the Laplacian matrix $\mathscr{L}$ are positive and real except for a simple zero eigenvalue. The right eigenvector corresponding to the simple zero eigenvalue is $1_n = \begin{bmatrix} 1 & 1 & \cdots & 1 \end{bmatrix}^T$; i.e., $\mathscr{L}1_n = 0$ [19], [37]. When a communication network to implement the distributed control strategy is described by a connected graph, a sparse communication network is useful, and the consensus protocol in (2.29) is commonly used for node i to adjust its state variable x_i [62]:

$$\dot{x}_i(t) = -\sum_{j\in N_i} a_{ij}\left(x_i(t - \tau_{ij}) - x_j(t - \tau_{ij})\right) \tag{2.29}$$

where τ_{ij} is the communication time delay between nodes j and i. If this control law is

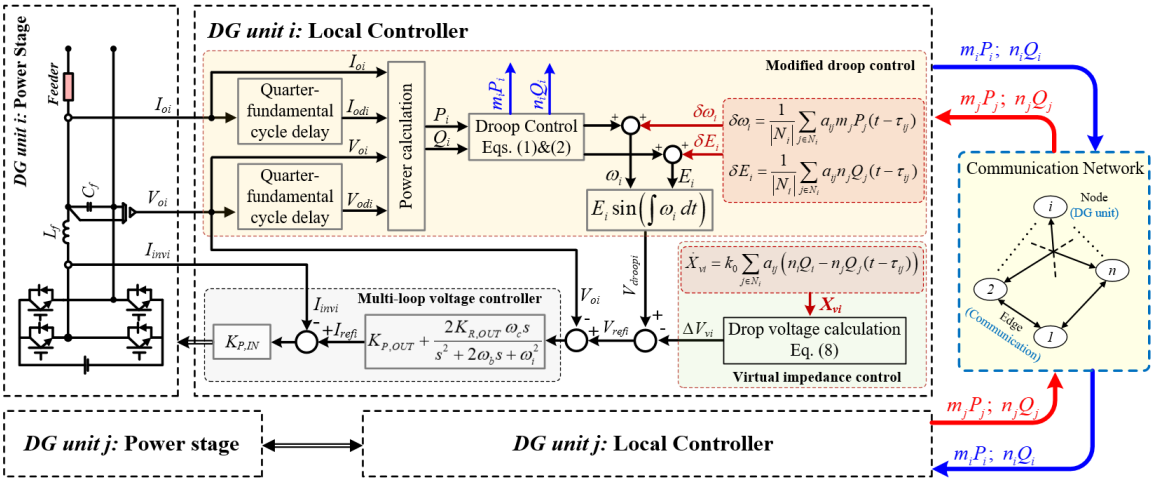

Figure 2.18: Proposed power control scheme for i-th DG unit

generalized and applied to every node in the system, all state variables x_i will converge to a common equilibrium point; i.e., $x_1 = x_2 = \cdots = x_n$ [62].

2.2.2 Proposed Control Scheme

To guarantee accurate power sharing regardless of load conditions and microgrid configurations, the adaptive virtual impedance control method has been used as one of the most advanced techniques [63]. However, most of the virtual impedance control methods are implemented in a centralized control fashion [19, 20, 34, 40] and the distributed virtual impedance-based approach has not sufficiently realized so far. A consensus-based virtual impedance controller was recently introduced [38,39], but the virtual impedance regulator is very complicated due to the many control gains.

To eliminate the frequency and voltage deviations, other DCMs need PI controllers for all DG units, which increase the computational burden on the DG local controllers and the complexity of the control system. Therefore, a simplified distributed control scheme is proposed, as shown in Fig. 2.18. The scheme requires only the DG neighbors' power information and does not use information about the feeder impedances and the loads.

2.2.2.1 Distributed Virtual Impedance-Based Power Sharing Control

Accurate reactive load power sharing ($n_iQ_i = n_jQ_j$) can be realized in a distributed manner by using the consensus protocol in (2.29) with the DG reactive power n_iQ_i as the DG state. In the consensus protocol, the desired state x_i should be directly controlled. However, the selected state, n_iQ_i, cannot be directly controlled because the DG units are operating in $V - f$ mode. Therefore, the consensus protocol uses the virtual impedance

as the controllable quantity instead of from (2.28), and the control law of the i^{th} DG unit is modified from (2.29):

$$\dot{X}_{vi}(t) = k_0 \sum_{j \in N_i} a_{ij} \left(n_i Q_i(t) - n_j Q_j(t - \tau_{ij}) \right) \tag{2.30}$$

where k_0 is the positive control gain.

From (2.30), the update rule of the i^{th} DG virtual impedance is obtained as:

$$X_{vi}(t) = k_0 \int \sum_{j \in N_i} a_{ij} \left(n_i Q_i(t) - n_j Q_j(t - \tau_{ij}) \right) dt. \tag{2.31}$$

The voltage drop $\Delta V_{vi}(t)$ due to the virtual impedance in (2.31) becomes:

$$\Delta V_{vi}(t) = -X_{vi}(t) I_{odi}(t) \tag{2.32}$$

where $I_{odi}(t)$ is the delayed component of the i^{th} DG line current $I_{oi}(t)$ for one quarter of a fundamental cycle. Thus, to implement the virtual impedance $X_{vi}(t)$, the voltage reference $V_{refi}(t)$ for the voltage controller is modified as following:

$$V_{refi}(t) = V_{droopi}(t) - V_{vi}(t) = V_{droopi}(t) + X_{vi}(t) I_{odi}(t). \tag{2.33}$$

2.2.2.2 Compensation of Frequency and Voltage Deviations

To remove the frequency and voltage deviations in a distributed fashion, compensating signals from the distributed secondary controller, $\delta\omega_i$ and δE_i, are usually added to the conventional droop controllers [45–48, 50, 51, 64]:

$$\omega_i = \omega_0 - m_i P_i + \delta\omega_i, \tag{2.34}$$

$$E_i = E_0 - n_i Q_i + \delta E_i. \tag{2.35}$$

To generate suitable compensating signals, conventional DCM needs PI controllers in the DG local controller and additional information such as the frequency and voltage magnitude of its neighbors, which increase the computational burden and complexity. Therefore, the compensating signals are determined based on the neighbors' powers information

without using any PI controller:

$$\delta\omega_i = \frac{1}{|N_i|}\sum_{j\in N_i} a_{ij} m_j P_j\left(t-\tau_{ij}\right), \tag{2.36}$$

$$\delta E_i = \frac{1}{|N_i|}\sum_{j\in N_i} a_{ij} n_j Q_j\left(t-\tau_{ij}\right). \tag{2.37}$$

After plugging (2.36) and (2.37) into (2.34) and (2.35), the angular frequency and voltage magnitude become:

$$\omega_i(t) = \omega_0 - m_i P_i(t) + \frac{1}{|N_i|}\sum_{j\in N_i} a_{ij} m_j P_j\left(t-\tau_{ij}\right), \tag{2.38}$$

$$E_i(t) = E_0 - n_i Q_i(t) + \frac{1}{|N_i|}\sum_{j\in N_i} a_{ij} n_j Q_j\left(t-\tau_{ij}\right). \tag{2.39}$$

2.2.2.3 Multi-Loop Voltage Controller

With (2.38) and (2.39), the instantaneous voltage reference in (2.33) becomes:

$$V_{refi}(t) = E_i(t)\sin\left(\int \omega_i(t)dt\right) + X_{vi}(t) I_{odi}(t). \tag{2.40}$$

The multi-loop voltage controller in Fig. 2.18 is applied to generate the desired output voltage for the DG unit according to the voltage reference in (2.40) [19, 20]. In the multi-loop voltage controller, the outer loop uses a non-ideal proportional-resonant (PR) controller that is tuned at the fundamental frequency:

$$G_{OUT}(s) = K_{P,OUT} + \frac{2K_{R,OUT}\omega_b s}{s^2 + 2\omega_b s + \omega_i^2}, \tag{2.41}$$

where $K_{P,OUT}$ and $K_{R,OUT}$ are the outer loop proportional and resonant controller gains, respectively, and ω_b is the cutoff frequency of the resonant controller. The inner loop is a simple proportional controller with gain $K_{P,IN}$ and filter inductor current feedback:

$$G_{IN}(s) = K_{P,IN}. \tag{2.42}$$

2.2.3 Steady-State and Small-Signal Analysis

2.2.3.1 Steady-State Performance Investigation

Assuming that the microgrid operates in steady state for $t \geq t_0$, the following important results are obtained with the proposed control strategy.

Theorem 1: Accurate reactive power sharing is realized with the consensus-based virtual impedance controller in (2.30).

Proof : We define global variables for the whole n DG microgrid system as: $\dot{X}_v \triangleq col\left(\dot{X}_{vi}(t)\right)$ and $Q_{norm} \triangleq col\left(n_i Q_i(t)\right)$ where $col(x_i) \triangleq \begin{bmatrix} x_1 & x_2 & \cdots & x_n \end{bmatrix}^T$. In steady state, $\dot{X}_{vi}(t) = 0$ and $Q_j(t - \tau_{ij}) = Q_j(t)$. Hence, the entire system can be described as follows from (2.30):

$$\dot{X}_v = k_0 \mathcal{L} Q_{norm} = 0. \tag{2.43}$$

Considering that $\mathscr{L} \in \mathbb{R}^{n \times n}$ is the Laplacian matrix of an undirected graph, it has a simple zero eigenvalue with a corresponding right eigenvector, $\mu 1_n$, $\mu \in \mathbb{R} \setminus \{0\}$, and other eigenvalues are positive and real [19], [37]. Hence, (2.43) becomes:

$$0 = k_0 \mathcal{L} Q_{norm} \Leftrightarrow Q_{norm} = \mu 1_n \Leftrightarrow n_i Q_i(t) = n_j Q_j(t), \forall i, j \in \xi. \tag{2.44}$$

which shows for the reactive load power demand to be shared accurately among DG units.

Theorem 2 : With the modified frequency droop controller in (2.38), perfect active power sharing is maintained without frequency deviation.

Proof : Let N be an $n \times n$ matrix defined as $N \triangleq diag(|N_i|^{-1})$, and let the following be column vectors: $e_\omega \triangleq col(\omega_0 - \omega_i(t))$ and $P_{norm} \triangleq col(m_i P_i(t))$. In steady state, $P_j(t - \tau_{ij}) = P_j(t)$, which means that (2.38) can be modified for n DG system as follows:

$$e_\omega = N \mathcal{L} P_{norm}. \tag{2.45}$$

Furthermore, the entire system operates at the same frequency in steady state. Hence, for $\rho \in \mathbb{R}$, the condition in (2.46) is satisfied:

$$e_\omega = \rho 1_n. \tag{2.46}$$

By substituting (2.46) into (2.45) and multiplying both sides with $1_n^T N^{-1}$, the following equation is derived:

$$1_n^T N^{-1} \rho 1_n = 1_n^T N^{-1} N \mathcal{L} P_{norm} \Leftrightarrow \rho 1_n^T N^{-1} 1_n = 1_n^T \mathcal{L} P_{norm}. \tag{2.47}$$

In the case of a balanced Laplacian matrix (i.e., $1_n^T \mathcal{L} = 0$) (2.47) becomes:

$$\rho 1_n^T N^{-1} 1_n = 0. \tag{2.48}$$

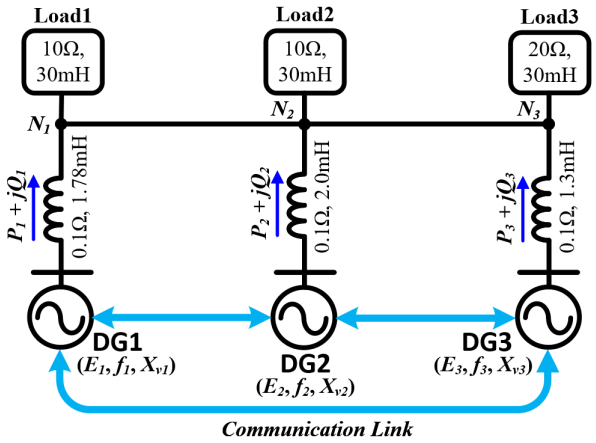

Figure 2.19: The islanded microgrid used in stability analysis and experiment

Since $1_n^T N^{-1} 1_n = |N_1| + |N_2| + \cdots + |N_n| > 0$, (2.48) yields:

$$\rho = 0 \Leftrightarrow e_\omega = 0 \Leftrightarrow \omega_i(t) = \omega_0, \ \forall\, i \in \xi. \tag{2.49}$$

When $e_\omega = 0$, (2.50) is derived from (2.45):

$$0 = N\mathcal{L}P_{norm} \Leftrightarrow P_{norm} = \gamma 1_n \Leftrightarrow m_i P_i(t) = m_j P_j(t), \ \forall\, i, j \in \xi \tag{2.50}$$

where $\gamma \in \mathbb{R} \setminus \{0\}$.

Equations (2.49) and (2.50) demonstrate that frequency restoration and active power sharing are achieved with the proposed strategy.

Theorem 3: With the modified voltage droop controller in (2.39), the microgrid voltage deviation is eliminated once accurate reactive power sharing is realized with the virtual impedance control in (2.30).

Proof : As proven in *Theorem* 1, (2.44) is achieved with DG virtual impedance control in (2.30). With $Q_j(t - \tau_{ij}) = Q_j(t)$ in steady state, substituting (2.44) into (2.39) yields $E_i(t) = E_0, \forall i \in \xi$, which demonstrates that the microgrid voltage deviation is eliminated with the proposed control method.

In summary, the proposed control method guarantees accurate power sharing among DG units and restoration of the frequency and voltage, regardless of the load conditions.

2.2.3.2 Small-Signal State-Space Model

The system dynamic performance and stability are investigated by deriving a small-signal state-space model using a modeling approach from previous studies [65, 66]. The DG's instantaneous active and reactive power, p_i and q_i, are determined from the equivalent

Table 2.3: System parameters

System parameter	**Simulation**	**Experiment**	
LC filter, L_f/C_f	1.3 mH/ 10 μF	1.3 mH/ 10 μF	
DC link voltage, V_{dc}	400 V	280 V	
Nominal voltage, E_0	220 V, 60 Hz	110 V, 60 Hz	
Switching frequency, f_{sw}	10 kHz	10 kHz	
Droop Control	**Simulation**		**Experiment**	
	DG1=DG2	**DG3=DG4**	**DG1=DG3**	**DG2**
m (rad/W·s)	0.001	0.0005	0.0015	0.003
n (V/Var)	0.005	0.0025	0.007	0.014
Double-Loop Voltage Control		**Simulation**	**Experiment**	
$K_{PO}/K_{RO}/K_{IN}$		0.1/ 40/ 30	0.1/ 30/ 25	
ω_b		12.5 rad/s	12.5 rad/s	
Virtual Impedance Control		**Simulation**	**Experiment**	
k_0		15	12	

circuit in Fig. (2.17) [15, 22]:

$$p_i = \frac{E_i V_{PCC}}{X_i + X_{vi}} \sin \varphi_i, \tag{2.51}$$

$$q_i = \frac{V_{PCC}\left(E_i \cos \varphi_i - V_{PCC}\right)}{X_i + X_{vi}}, \tag{2.52}$$

where φ_i is the phase-shift angle between E_i and V_{PCC}. By linearizing (2.51) and (2.52), the small-signal variations $\Delta P_i(t)$ and $\Delta Q_i(t)$ of the measured active and reactive power after low-pass filtering are obtained:

$$\Delta P_i(t) = \frac{\omega_{LPF}}{s + \omega_{LPF}} \left(\alpha_{pi} \Delta E_i(t) + \beta_{pi} \Delta \varphi_i(t) + \gamma_{pi} \Delta X_i(t)\right), \tag{2.53}$$

$$\Delta Q_i(t) = \frac{\omega_{LPF}}{s + \omega_{LPF}} \left(\alpha_{qi} \Delta E_i(t) + \beta_{qi} \Delta \varphi_i(t) + \gamma_{qi} \Delta X_i(t)\right), \tag{2.54}$$

where $\alpha_{pi} = \partial p_i/\partial E_i$, $\beta_{pi} = \partial p_i/\partial \varphi_i$, $\gamma_{pi} = \partial p_i/\partial X_{vi}$, $\alpha_{qi} = \partial q_i/\partial E_i$, $\beta_{qi} = \partial q_i/\partial \varphi_i$, $\gamma_{qi} = \partial q_i/\partial X_{vi}$, the operator Δ indicates a small-signal perturbation around the system's operating equilibrium point, and ω_{LPF} is the cutoff angular frequency of the low-pass filter.

For simple analysis, the communication delay is assumed to be equal for all links ($\tau_{ij} = \tau$). Thus, the frequency and voltage variations, $\Delta\omega_i(t)$ and $\Delta E_i(t)$, are obtained

by linearizing (2.38) and (2.39), respectively:

$$\Delta\omega_i(t) = -m_i\Delta P_i(t) + \frac{1}{|N_i|}\sum_{j\in N_i} a_{ij}m_j\Delta P_j(t-\tau), \tag{2.55}$$

$$\Delta E_i(t) = -n_i\Delta Q_i(t) + \frac{1}{|N_i|}\sum_{j\in N_i} a_{ij}n_j\Delta Q_j(t-\tau). \tag{2.56}$$

The small-signal variation $\Delta\dot{X}_i(t)$ of the virtual impedance $\dot{X}_i(t)$ is derived by linearizing the control law in (2.30):

$$\Delta\dot{X}_{vi}(t) = k_0\sum_{j\in N_i} a_{ij}\left(n_i\Delta Q_i(t) - n_j\Delta Q_j(t-\tau)\right). \tag{2.57}$$

From (2.53)-(2.57), the small-signal state-space model of the proposed control system becomes the following by using $\Delta\omega_i(t) = s\Delta\varphi_i(t)$:

$$\dot{x}_{MG}(t) = \Omega_{MG}x_{MG}(t) + \Omega_{MG\_d}x_{MG}(t-\tau) \tag{2.58}$$

where $x_{MG}(t)$ is $4n$ state variables defined by $x_{MG}(t) = [\Delta P_1(t)\ \Delta P_2(t)\cdots\ \Delta P_n(t)\ \Delta Q_1(t)\ \Delta Q_2(t)\cdots\ \Delta Q_n(t)\ \Delta\varphi_1(t)\ \Delta\varphi_2(t)\cdots\ \Delta\varphi_n(t)\ \Delta X_{v1}(t)\ \Delta X_{v2}(t)\cdots\ \Delta X_{vn}(t)]^T$. Ω_{MG} and Ω_{MG_d} are $4n\times 4n$ state matrices and are shown in the Appendix A.

2.2.3.3 Controller Gain Design and Stability Analysis

Based on the small-signal state-space model in (2.58), the controller gain design and stability for the proposed method are considered by using the microgrid with three DG units, as shown in Fig. 2.19. The system parameters are listed in Table 2.3.

Controller gain design: It is very simple to design the controller because the proposed control system has only one control gain k_0. Initially, the controller gain is determined with zero communication delay (i.e., $\tau = 0$). The state matrices of the three-DG unit system in Fig. 2.19 (Ω_{3DG} and Ω_{3DG_d}) are derived from the generalized modeling approach in (2.58). In the case of $\tau = 0$, the small-signal state-space model for the microgrid in Fig. 2.19 becomes:

$$\dot{x}_{3DG}(t) = Mx_{3DG}(t) \tag{2.59}$$

where $x_{3MG}(t) = [\Delta P_1(t)\ \Delta P_2(t)\ \Delta P_3(t)\ \Delta Q_1(t)\ \Delta Q_2(t)\ \Delta Q_3(t)\ \Delta\varphi_1(t)\ \Delta\varphi_2(t)\ \Delta\varphi_3(t)\ \Delta X_{v1}(t)\ \Delta X_{v2}(t)\ \Delta X_{v3}(t)]^T$, $M = \Omega_{3DG} + \Omega_{3DG\_d}$.

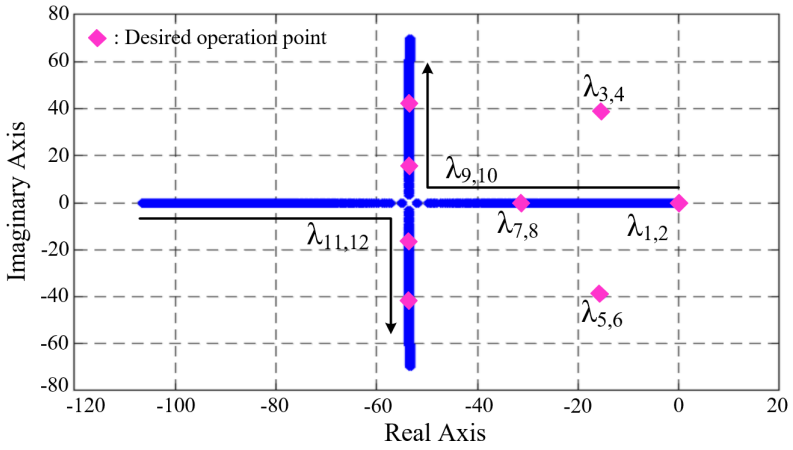

Figure 2.20: Root locus diagram according to control gain k_0 with negligible communication delay ($\tau = 0$): $0 \leq k_0 \leq 20$, $m_1 = 0.5m_2 = m_3 = 0.0015 rad/W \centerdot s$, $n_1 = 0.5n_2 = n_3 = 0.007 V/Var$, $\omega_{LPF} = 31.5 rad/s$.

From (2.59), the characteristic equation of the system is:

$$\det\left(M - sI\right) = 0. \tag{2.60}$$

From (2.60), the characteristic roots for a given controller gain k_0 are obtained using the Matlab $eig(M)$ function to obtain the eigenvalues of M. Fig. 2.20 shows a plot of the trajectories of all eigenvalues obtained by increasing the gain k_0 from 0 to 20 with small intervals. The control system is stable because all the eigenvalues are kept in the left haft plane except two zero eigenvalues λ_1 and λ_2 caused by the singularity of the state matrix M. The dynamic performance is mainly determined by the dominant poles $\lambda_9 - \lambda_{12}$ because the other poles ($\lambda_1 - \lambda_8$) are fixed, and these poles move along the direction of the arrow as k_0 increases. As k_0 increases, the system stability improves with an underdamped response. k_0 is selected as 12 to provide the desired system damping and stability performance.

Stability with communication delay: Next, the system stability is evaluated with various communication delays. The small-signal state-space model for the microgrid in Fig. 2.19 with communication delay becomes a delay differential equation:

$$\dot{x}_{3DG}\left(t\right) = \Omega_{3DG} x_{3DG}\left(t\right) + \Omega_{3DG\_d} x_{3DG}\left(t - \tau\right). \tag{2.61}$$

The characteristic equation for the system in (2.61) becomes [65]:

$$\det\left(-sI + \Omega_{3DG} + \Omega_{3DG\_d} e^{-s\tau}\right) = 0. \tag{2.62}$$

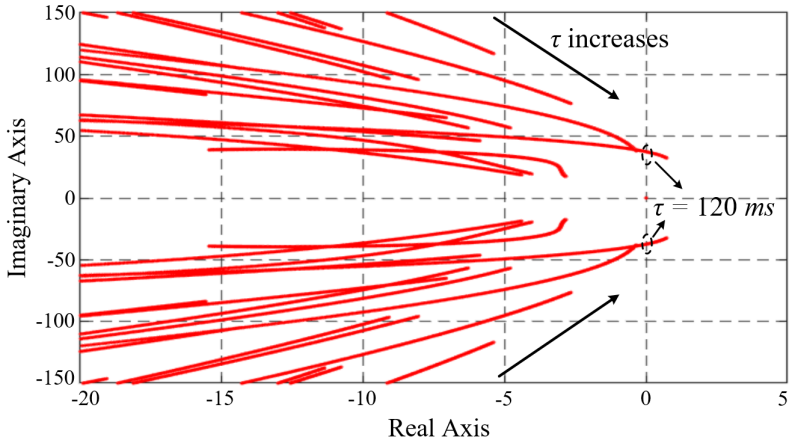

Figure 2.21: Root locus diagram according to communication delay τ: $0 \leq \tau \leq 150ms$, $m_1 = 0.5m_2 = m_3 = 0.0015rad/W \centerdot s$, $n_1 = 0.5n_2 = n_3 = 0.007V/Var$, $\omega_{LPF} = 31.5rad/s$, $k_0 = 12$.

It difficult to find the exact characteristic roots of the system in (2.61) because the characteristic equation in (2.62) has infinite solutions. The eigenvalues of (2.62) are obtained for a specific communication delay from a previous numerical approach [65], and Fig. 2.21 shows the trajectories of all eigenvalues obtained by increasing the communication delay τ from 0 to $150ms$. The eigenvalues approach the right half plane as the communication delay increases and remain in the left haft plane until $\tau = 120ms$. Therefore, the system is stable if the communication delay is less than $120ms$.

2.2.4 Simulation Results

An islanded microgrid with a meshed structure is simulated in the PSIM environment to evaluate the proposed control strategy. As shown in Fig. 2.22, the microgrid used in the simulation is composed of four DG units. DG units 3 and 4 are rated for twice as much power as units 1 and 2. There are also different loads at points $N_1 - N_4$. The system parameters are listed in Table 2.3. A delay of $1ms$ is included in the communication links of the DG units.

2.2.4.1 Control Performance with the Proposed Method

The power sharing performance of the system with the proposed control scheme is illustrated in Fig. 2.23. Four simulation stages are considered. Stage 1 occurs at $0-5s$, where the microgrid is originally operated with the conventional droop controller with loads 1-4 at nodes $N_1 - N_4$. Stage 2 occurs at $5 - 10s$. The proposed control method is applied at $5s$. Stage 3 occurs at $10 - 15s$, where load 1 is disconnected from node N_1. Stage 4

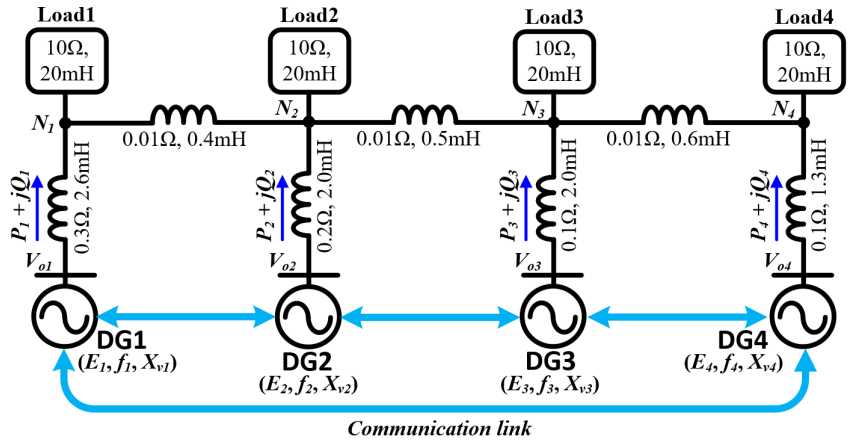

Figure 2.22: The islanded microgrid used in simulation.

occurs at $15 - 20s$, where load 1 is reconnected to the system.

As shown in Figs. 2.23(a) and (b), the real power demands are always shared accurately by DG units in steady state, but the reactive power sharing shows poor performance with the conventional method in stage 1. However, when the proposed control method is activated at $5s$, the total reactive power demand is shared accurately among DG units after a short transient period.

Accurate reactive power sharing is maintained even though the microgrid configuration and total load demand are changed, as shown in stages 3 and 4. With the proposed control scheme, perfect active and reactive power sharing is always guaranteed in steady state (see Figs. 2.23(a) and (b)). Fig. 2.23(c) shows the variation of the DG virtual impedances. After the proposed control scheme is applied at $5s$, the DG virtual impedances are changed adaptively to share the reactive power accurately, as in Fig. 2.23(b).

Figs. 2.23(d) and (e) demonstrate the frequency and voltage restoration performance with the proposed control method. The set points of the frequency and the voltage magnitude are less than the nominal values in stage 1 with the conventional droop control method. However, when using the proposed method at $5s$, they are restored to the nominal values in steady state in spite of the load conditions and the microgrid structure in stages 3 and 4.

2.2.4.2 Performance during a Communication Link Failure

The performance of the system during a communication link interruption is shown in Fig. 2.24. Initially, the system is operated under the same operating conditions as in stage 4 in Fig. 2.23. At $5s$, the communication link between DG1 and DG2 fails. At $10s$ and

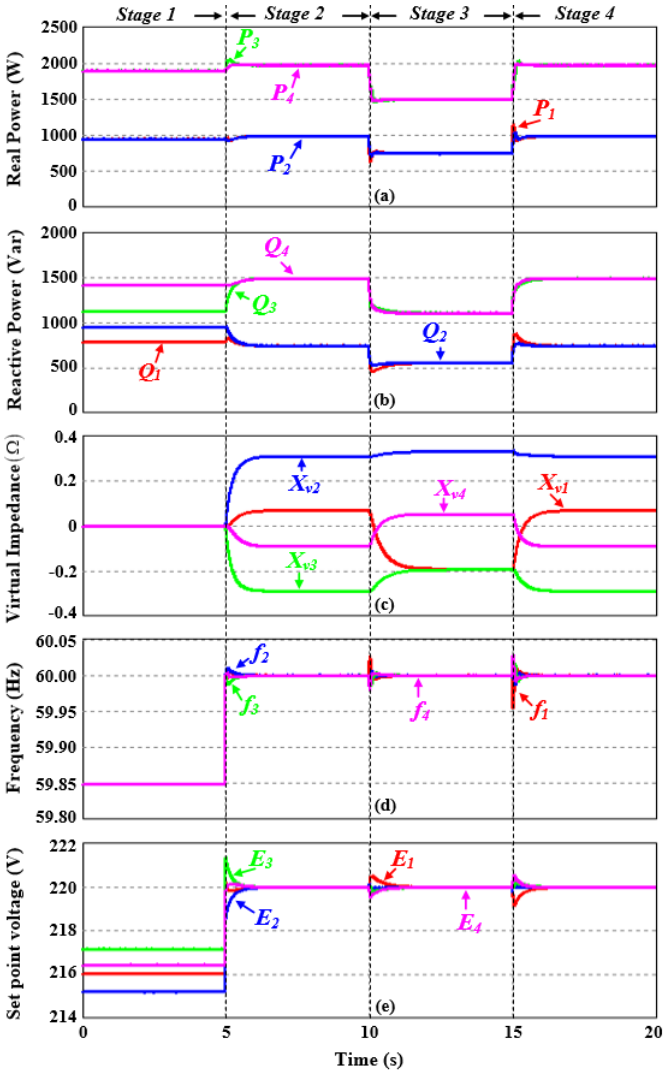

Figure 2.23: Control performance with proposed control scheme: (a) active power; (b) reactive power; (c) DG virtual impedance; (d) frequency set point; (e) voltage magnitude set point.

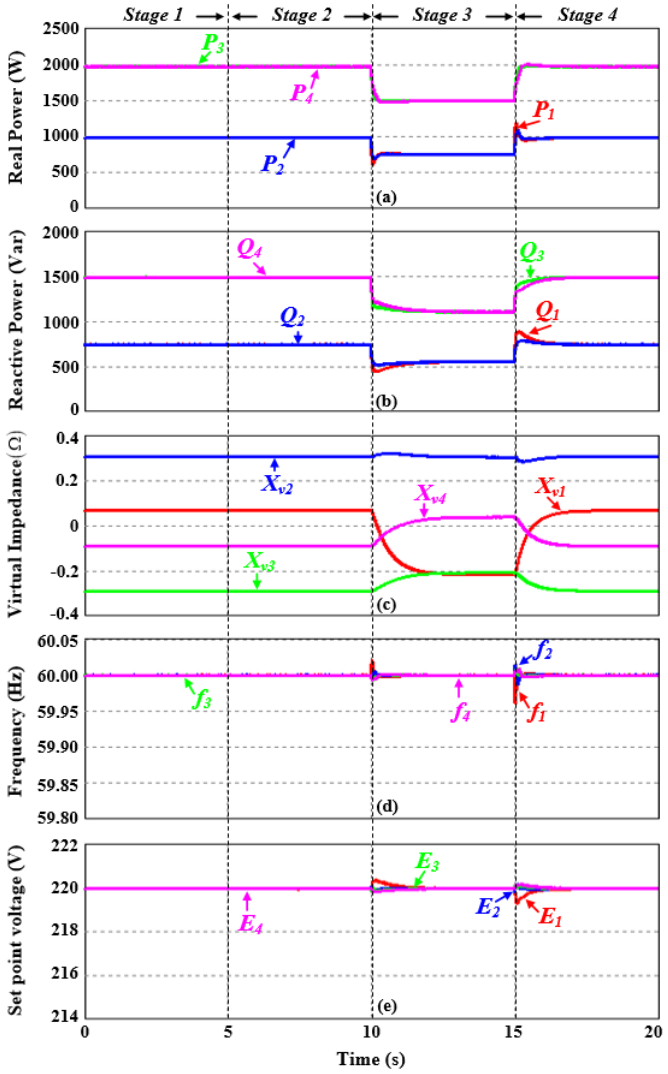

Figure 2.24: Control performance with proposed control scheme during a communication link failure: (a) active power; (b) reactive power; (c) DG virtual impedance; (d) frequency set point; (e) voltage magnitude set point.

15s, the load conditions change in the same scenarios as in Fig. 2.23. As shown in Fig. 2.24, the proposed method shows good performance similar to those in Fig. 2.23 in spite of the communication link failure.

2.2.4.3 Plug-and-Play Operation

Fig. 2.25 shows the control performance when a DG unit is disconnected from and reconnected to the microgrid system. At $t = 0$, the microgrid operates under the same conditions as in stage 4 in Fig. 2.23. The DG2 is disconnected at 5s and reconnected at 10s. The proposed method shows good performance that is the same as in Fig. 2.23 irrespective of the plug-and-play operation.

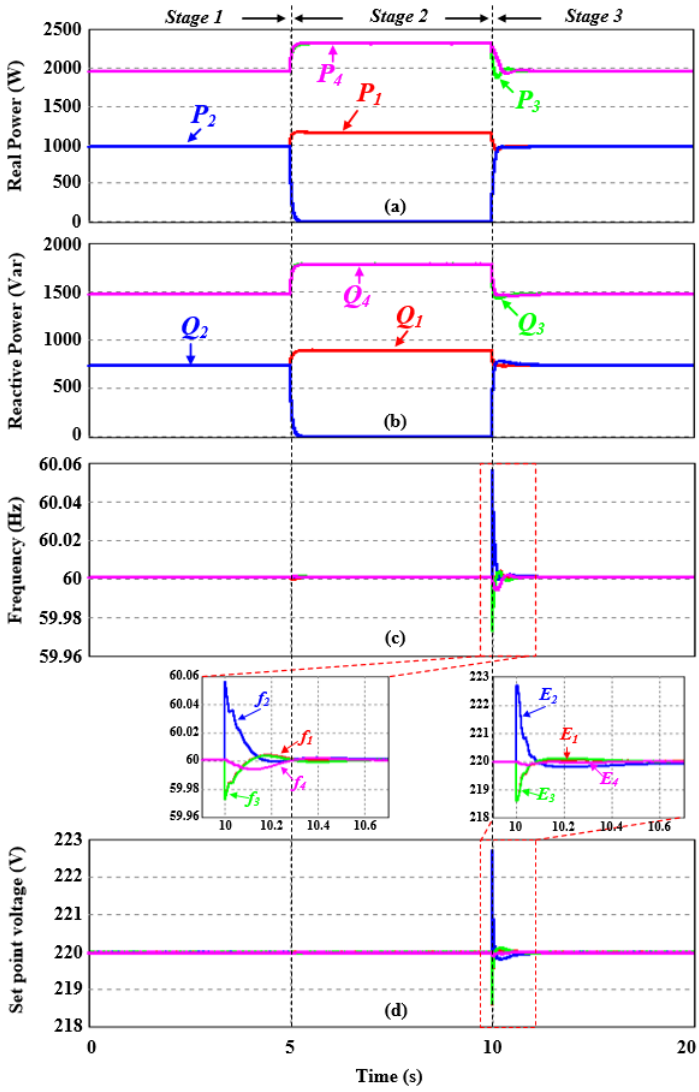

Figure 2.25: Control performance in plug-and-play operation: (a) active power; (b) reactive power; (c) frequency set point; (d) voltage magnitude set point.

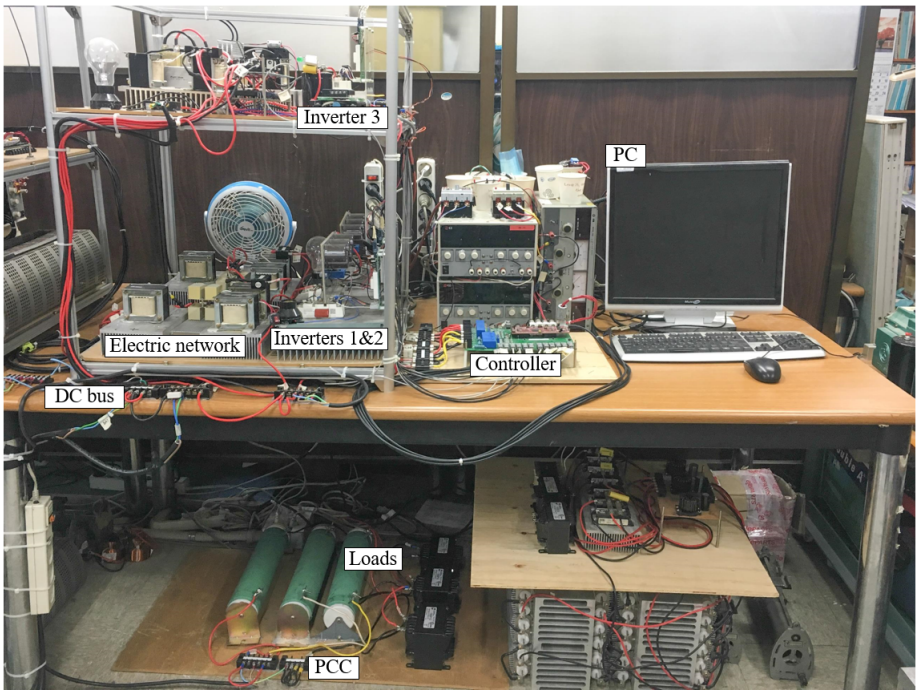

Figure 2.26: The photo of the experimental setup.

2.2.5 Experimental Results

Experiments are conducted with a single-phase scaled-down microgrid prototype with three DG units, as shown in Fig. 2.26. The system diagram is shown in Fig. 2.19, where DG units 1 and 3 are rated for twice as much power as DG unit 2. The proposed control scheme is implemented using a DSP (32-bit floating-point 200MHz TMS320F28379D, Texas Instruments). The delay on the communication links of the DG units is $1ms$. The key parameters of the system are listed in Table 2.3. Figs. 2.27-2.30 shows the results.

In Fig. 2.27, the microgrid system is originally controlled by the conventional $P-\omega$ and $Q-E$ droop controllers with loads 1-3 at the PCC. As shown in Fig. 2.27(b), the reactive power demands cannot be shared accurately among DG units in stage 1. However, the power sharing error is eliminated when the proposed control scheme is activated at t_1 after a short transient period. Accuracy is always realized in both active and reactive power sharing when using the proposed distributed controller, even when load 3 is disconnected and reconnected to the system at t_2 and t_3, respectively (see Figs. 2.27(a) and (b)). In Figs. 2.27(c) and (d), the set points of the frequency and voltage magnitude are also maintained at their nominal values in steady state despite the load variations.

Fig. 2.28 demonstrates the control performance with the proposed control scheme when the communication link between DG1 and DG3 fails. The system originally oper-

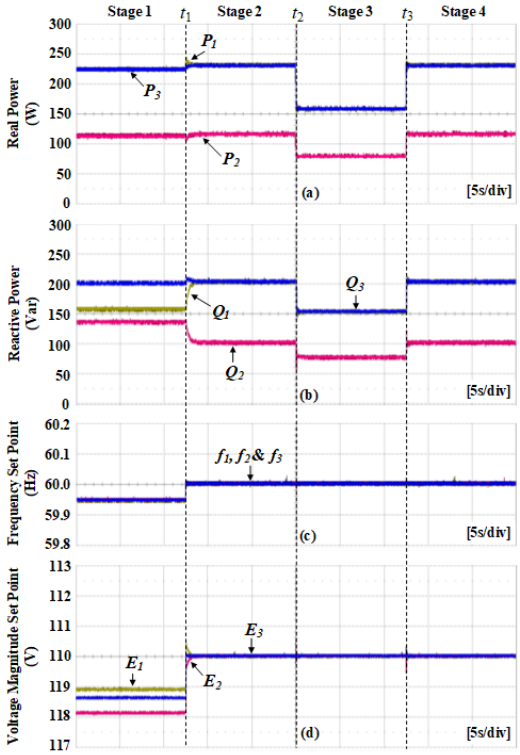

Figure 2.27: Control performance with proposed control scheme: (a) active power; (b) reactive power; (c) frequency set point; (d) voltage magnitude set point.

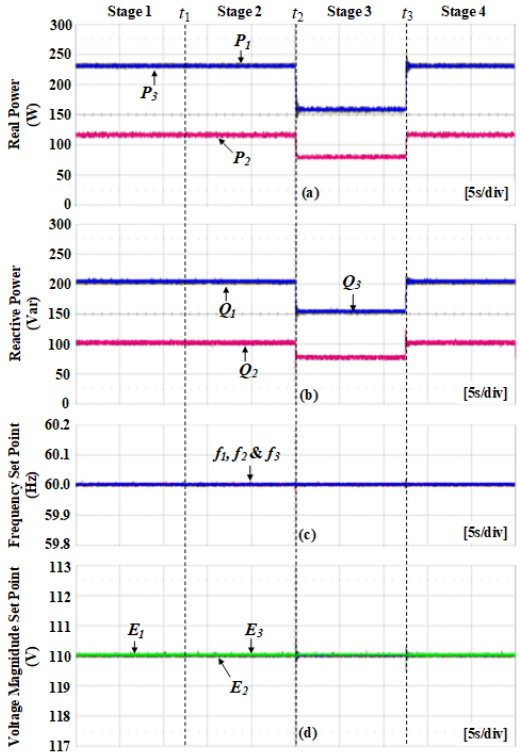

Figure 2.28: Control performance with proposed control scheme during a communication failure: (a) active power; (b) reactive power; (c) frequency set point; (d) voltage magnitude set point.

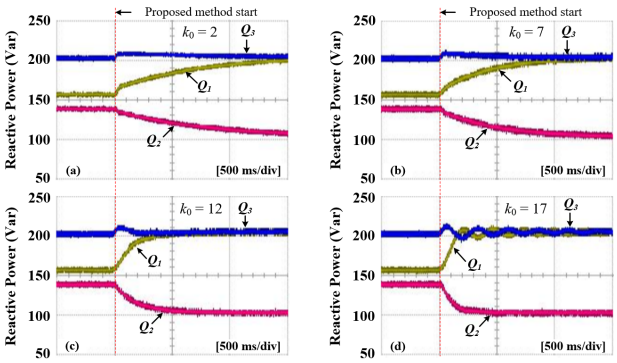

Figure 2.29: The dynamic responses for various values of k_0: (a) $k_0 = 2$; (b) $k_0 = 7$; (c) $k_0 = 12$; (d) $k_0 = 17$.

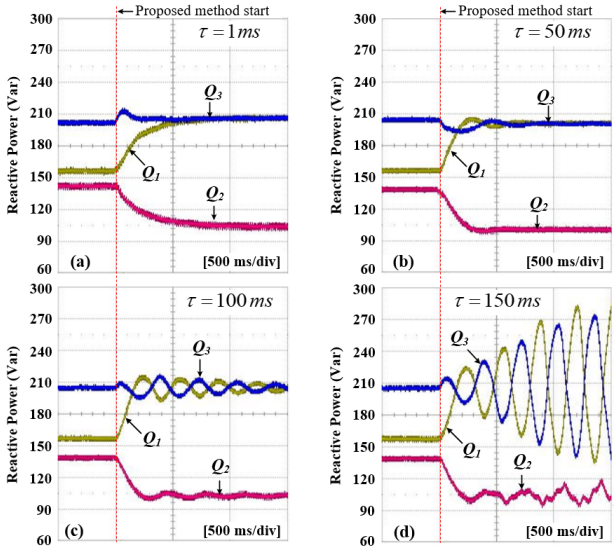

Figure 2.30: The dynamic responses for different communication delays: (a) $\tau = 1ms$; (b) $\tau = 50ms$; (c) $\tau = 100ms$; (d) $\tau = 150ms$.

ates under the same operating conditions as in stage 4 in Fig. 2.27. At t_1, the communication link between DG1 and DG3 is interrupted. At t_2 and t_3, the load power demand changes in the same as in Fig. 2.27. As shown in Fig. 2.28, the proposed scheme always guarantees accurate power sharing and restoration of the frequency and voltage despite the communication link failure.

Fig. 2.29 shows the dynamic responses of the system for four different values of the control gain k_0 when the proposed method is activated. A small control gain can slow down the system response, while a large gain can lead to oscillation. The optimal gain value is $k_0 = 12$, which can provide fast response without oscillation (see Fig. 2.29(c)).

Fig. 2.30 shows the DGs' dynamic reactive power responses for various communication delays when the proposed control scheme is applied. With a small communication delay, perfect control performance can be achieved with the proposed control scheme (see Figs. 2.30(a) and (b)), and the system maintains stability even for a long communication delay of $\tau = 100ms$ (see Fig. 2.30(c)). For the case of $\tau = 150ms$, the system becomes unstable, and accurate power sharing cannot be achieved (see Fig. 2.30(d)).

2.2.6 Conclusion of the Section

A distributed control strategy has been proposed for the islanded microgrids. Accurate power sharing and restoration of the frequency and voltage are achieved in spite of changes in the load conditions. A distributed consensus-based virtual impedance controller is developed for accurate power sharing, and the conventional droop equations are modified for the frequency and voltage restorations.

Only one control gain is tuned to regulate the DG virtual impedance, and the frequency and voltage compensating signals are directly determined from the neighbors' droop information without any additional sensors or PI controllers in the local controllers. Therefore, the control system design is extremely simple without degrading the system performance. In addition, the control system's stability with communication delay is analyzed using a generalized small-signal state-space model. The system stability is guaranteed with communication delay less than $120ms$.

Chapter 3

Accurate Harmonic Power Sharing Strategy

This chapter presents an enhanced power sharing control scheme to share accurately dominant harmonic powers for meshed microgrids with the aid of adaptive regulation of the virtual impedances at dominant frequencies. The proposed control method provides accurate harmonic power sharing even when the microgrid configuration or the load condition is changed. Moreover, a simple secondary controller has also been proposed to remove the frequency/voltage deviations without additional voltage measurement at the point of common coupling (PCC). The proposed control scheme can be implemented directly in any type of microgrid structure (single-bus or meshed) without any information about the detailed microgrid configuration, feeder impedances, and the load powers, which decreases complexity and system cost. The proposed control method is theoretically investigated, and its feasibility and effectiveness are validated via simulation and experiment.

The rest of this chapter is outlined as follows: The system configuration along with an analysis of the power sharing control by using virtual impedance is described in Section 3.1. In Section 3.2, the proposed controller is presented, followed by simulation and experimental results based on the proposed strategy in sections 3.3 and 3.4, respectively. Finally, concluding remarks are presented in section 3.5.

3.1 Power Sharing Control Analysis

For simple analysis, an islanded meshed microgrid with two DG units with the same power rating is considered as shown in Fig. 3.1. There are two local loads, $Loc1$ and $Loc2$, located at the points, N_{L1} and N_{L2}, respectively; and two public loads, $Pub1$ and $Pub2$, are connected to the points N_{P1} and N_{P2}, respectively. We assume that line impedances in Fig. 3.1 are inductive ($R \approx 0$).

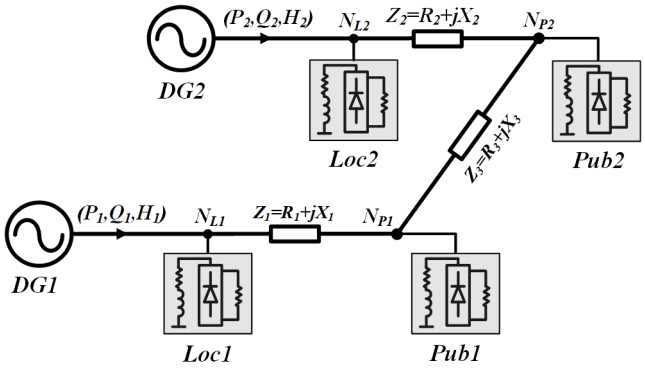

Figure 3.1: A meshed microgrid with two DG units.

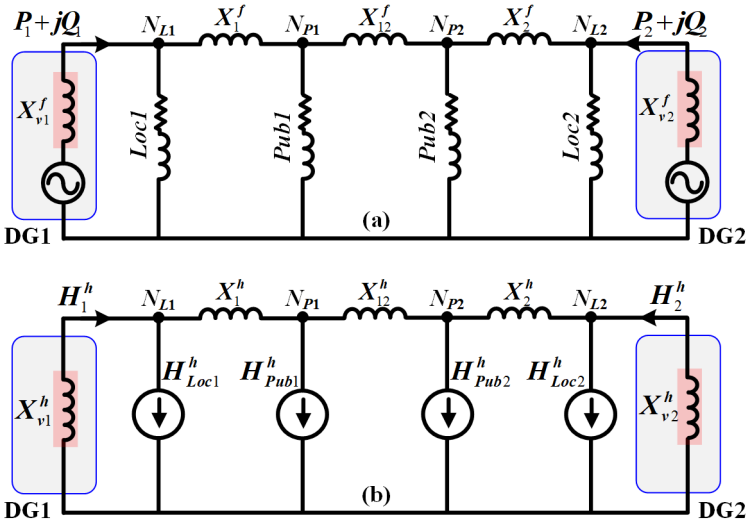

Figure 3.2: Equivalent circuits of the microgrid at different frequencies: (a) at fundamental frequency, (b) at harmonic frequencies.

Fig. 3.2(a) illustrates the equivalent circuit of the microgrid at the fundamental frequency, where the DG unit is modelled by a controlled voltage source with a series virtual impedance. Meanwhile, the load is a passive RL load. It should be noted that the inaccurate reactive power sharing issue in the meshed microgrid system is not discussed here because it is clearly analyzed in the previous chapter.

Fig. 3.2(b) shows the equivalent circuits of the microgrid at h-order harmonic frequency. In Fig. 3.2(b), the DG unit is modelled as an adjustable virtual impedance, and the nonlinear load is considered as a harmonic power source. To facilitate the power flow analysis, the circuit in Fig. 3.2(b) is decomposed into Figs. 3.3(a)–(d) according to the superposition theory, in which power flow produced by each power source is considered separately. From Fig. 3.3(a), power flows of two DG units to the local load of DG1, *Loc*1,

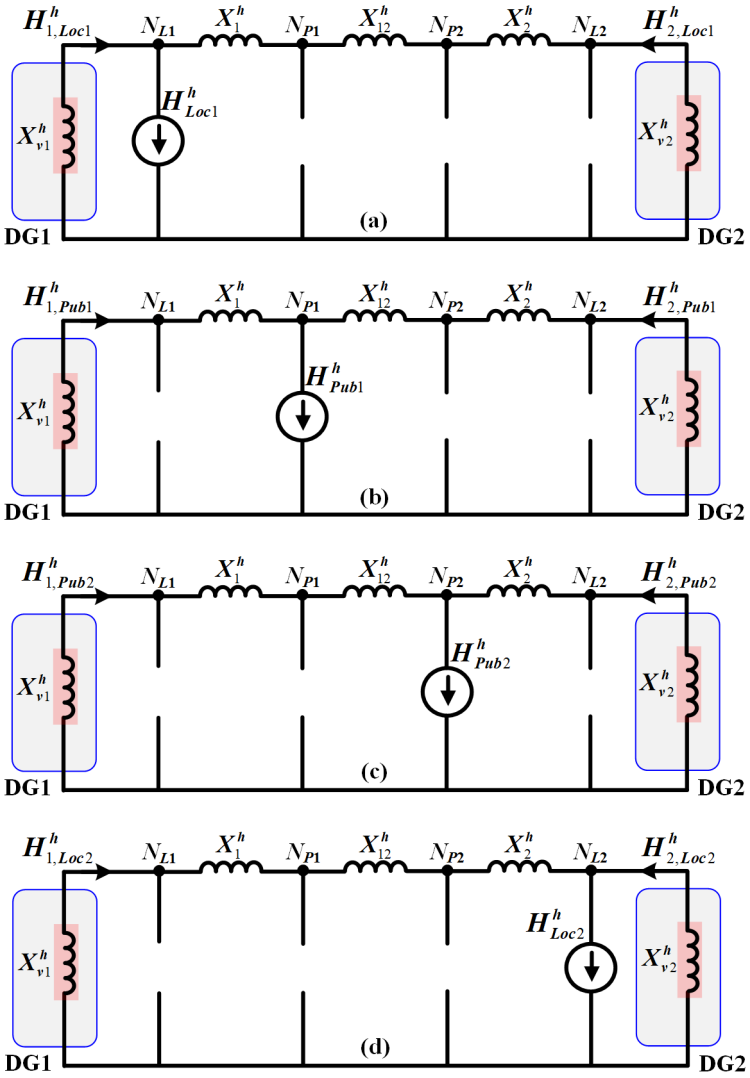

Figure 3.3: Equivalent circuit of the microgrid at harmonic frequencies when each nonlinear load is separately analyzed.

are calculated as follows:

$$H^h_{1,Loc1} = \frac{X^h_1 + X^h_{12} + X^h_2 + X^h_{v,2}}{X^h_1 + X^h_{v,1} + X^h_{12} + X^h_2 + X^h_{v,2}} H^h_{Loc1} \tag{3.1}$$

$$H^h_{2,Loc1} = \frac{X^h_{v,1}}{X^h_1 + X^h_{v,1} + X^h_{12} + X^h_2 + X^h_{v,2}} H^h_{Loc1} \tag{3.2}$$

From Fig. 3.3(b), the harmonic powers supplied to the public load, $Pub1$, by DG1 and DG2 are calculated, respectively, as follows:

$$H^h_{1,Pub1} = \frac{X^h_{12} + X^h_2 + X^h_{v,2}}{X^h_1 + X^h_{v,1} + X^h_{12} + X^h_2 + X^h_{v,2}} H^h_{Pub1} \tag{3.3}$$

$$H^h_{2,Pub1} = \frac{X^h_1 + X^h_{v,1}}{X^h_1 + X^h_{v,1} + X^h_{12} + X^h_2 + X^h_{v,2}} H^h_{Pub1} \tag{3.4}$$

Similarly, the shared powers to the public load, $Pub2$, by two DG units are determined from Fig. 3.3(c):

$$H^h_{1,Pub2} = \frac{X^h_2 + X^h_{v,2}}{X^h_1 + X^h_{v,1} + X^h_{12} + X^h_2 + X^h_{v,2}} H^h_{Pub2} \tag{3.5}$$

$$H^h_{2,Pub2} = \frac{X^h_1 + X^h_{v,1} + X^h_{12}}{X^h_1 + X^h_{v,1} + X^h_{12} + X^h_2 + X^h_{v,2}} H^h_{Pub2} \tag{3.6}$$

And, from Fig. 3.3(d), harmonic powers injected to the local load of DG2, $Loc2$, by two DG units are

$$H^h_{1,Loc2} = \frac{X^h_{v,2}}{X^h_1 + X^h_{v,1} + X^h_{12} + X^h_2 + X^h_{v,2}} H^h_{Loc2} \tag{3.7}$$

$$H^h_{2,Loc2} = \frac{X^h_1 + X^h_{v,1} + X^h_{12} + X^h_2}{X^h_1 + X^h_{v,1} + X^h_{12} + X^h_2 + X^h_{v,2}} H^h_{Loc2} \tag{3.8}$$

Then, from (3.1)-(3.8), the output harmonic powers of two DG units are determined as following:

$$\begin{aligned} H^h_1 =& H^h_{1,Loc1} + H^h_{1,Pub1} + H^h_{1,Pub2} + H^h_{1,Loc2} \\ =& \frac{\left(X^h_2 + X^h_{v,2}\right) H^h_{total}}{X^h_1 + X^h_{v,1} + X^h_{12} + X^h_2 + X^h_{v,2}} + \frac{X^h_{12}\left(H^h_{Loc1} + H^h_{Pub1}\right)}{X^h_1 + X^h_{v,1} + X^h_{12} + X^h_2 + X^h_{v,2}} \\ &+ \frac{X^h_1 H^h_{Loc1} - X^h_2 H^h_{Loc2}}{X^h_1 + X^h_{v,1} + X^h_{12} + X^h_2 + X^h_{v,2}}, \end{aligned} \tag{3.9}$$

$$\begin{aligned} H^h_2 =& H^h_{2,Loc1} + H^h_{2,Pub1} + H^h_{2,Pub2} + H^h_{2,Loc2} \\ =& \frac{\left(X^h_1 + X^h_{v,1}\right) H^h_{total}}{X^h_1 + X^h_{v,1} + X^h_{12} + X^h_2 + X^h_{v,2}} + \frac{X^h_{12}\left(H^h_{Loc2} + H^h_{Pub2}\right)}{X^h_1 + X^h_{v,1} + X^h_{12} + X^h_2 + X^h_{v,2}} \\ &+ \frac{X^h_2 H^h_{Loc2} - X^h_1 H^h_{Loc1}}{X^h_1 + X^h_{v,1} + X^h_{12} + X^h_2 + X^h_{v,2}}. \end{aligned} \tag{3.10}$$

Finally, the harmonic power sharing error ($\Delta H^h_{12} = H^h_1 - H^h_2$) is obtained from (3.9) and (3.10) as in (3.11):

$$\Delta H_{12}^h = \frac{\left[\left(X_2^h + X_{v,2}^h\right) - \left(X_1^h + X_{v,1}^h\right)\right] H_{total}^h}{X_1^h + X_{v,1}^h + X_{12}^h + X_2^h + X_{v,2}^h} + \frac{X_{12}^h \left[\left(H_{Loc1}^h + H_{Pub1}^h\right) - \left(H_{Loc2}^h + H_{Pub2}^h\right)\right]}{X_1^h + X_{v,1}^h + X_{12}^h + X_2^h + X_{v,2}^h} + \frac{2\left(X_1^h H_{Loc1}^h - X_2^h H_{Loc2}^h\right)}{X_1^h + X_{v,1}^h + X_{12}^h + X_2^h + X_{v,2}^h}. \tag{3.11}$$

As can be seen in (3.11), the harmonic power sharing error ΔH_{12}^h complexly depends on numerous factors such as mismatch in feeder impedances, load powers, load positions, and total line impedance, which are all time variables. Fortunately, from (3.9) and (3.10), it is possible to control the DG output harmonic powers by regulating the virtual impedances to keep the power sharing error ΔH_{12}^h to be zero. In order to avoid the contradiction when regulating the virtual impedances, the virtual impedances for the two DG units should be assigned opposite signs, i.e., $X_{v1}^h = -X_{v2}^h = X_v^h$. And, the regulation capability ($k_{\Delta HX}$) is defined by taking the derivative of ΔH_{12}^h with respect to X_v^h:

$$k_{\Delta HX} = \frac{d\Delta H_{12}^h}{dX_v^h} = -\frac{2H_{total}^h}{X_1^h + X_{12}^h + X_2^h} < 0; \quad \forall X_v^h. \tag{3.12}$$

Since $k_{\Delta HX}$ is always negative, in case $\Delta H_{12}^h > 0$ ($H_1^h > H_2^h$), the power sharing error $\Delta H_{12}^h > 0$ is reduced by increasing the virtual impedance X_v^h; otherwise, when $\Delta H_{12}^h < 0$ ($H_1^h < H_2^h$), it reaches zero by decreasing the virtual impedance X_v^h. Finally, the harmonic power sharing error in (3.11) is eliminated ($\Delta H_{12}^h = 0$) when the virtual impedance satisfies the relationship in (3.13):

$$X_{v,1}^h = -X_{v,2}^h = \frac{\left(X_2^h - X_1^h\right)}{2} + \frac{X_1^h H_{Loc1}^h - X_2^h H_{Loc2}^h}{H_{total}^h} + \frac{X_{12}^h \left[\left(H_{Loc1}^h + H_{Pub1}^h\right) - \left(H_{Loc2}^h + H_{Pub2}^h\right)\right]}{2H_{total}^h}. \tag{3.13}$$

3.2 Proposed Control Scheme

To enhance the power sharing performance by using the virtual impedance, we need further information such as the feeder impedances, detailed microgrid structure, and load powers. Unfortunately, they are not easy to obtain and are generally time varying ones. On the other hand, in order to solve frequency/voltage deviations, the additional sensors are usually required to detect the frequency and voltage magnitude at the PCC [42, 43], which increases the cost and complexity of system. To remove these problems, an en-

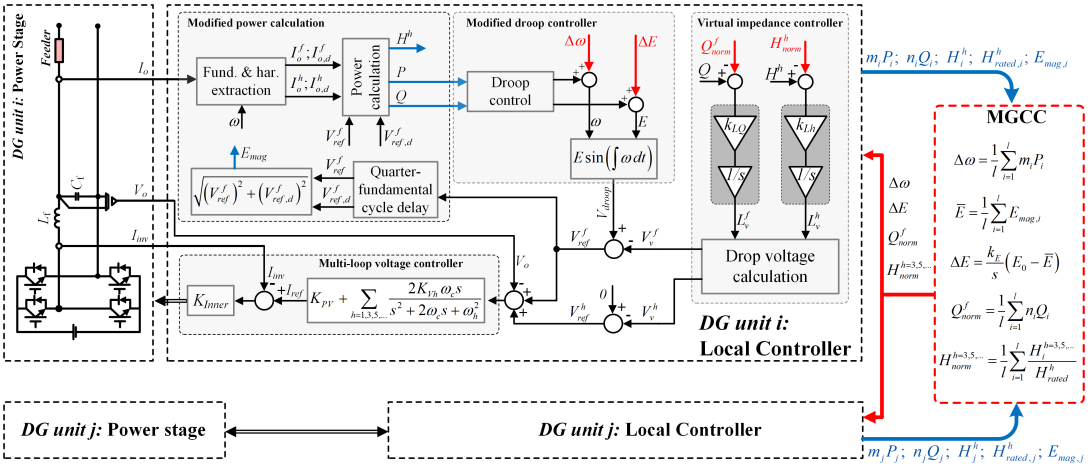

Figure 3.4: Proposed control scheme.

hanced control scheme is introduced. The proposed method does not require any knowledge of line impedances, the load powers, system frequency, or PCC voltage.

For general purposes, we consider a meshed microgrid with l DG units instead of the microgrid with two DG units shown in Fig. 3.1. The overall control block diagram of the proposed control scheme is shown in Fig. 3.4, in which two controllers, the MGCC and the local controller, are included.

3.2.1 Microgrid Central Controller

In Fig. 3.4, the DG units transmit the information relating to the active powers (m_1P_1, m_2P_2,$\cdots$, m_lP_l), reactive powers (n_1Q_1, n_2Q_2,$\cdots$, n_lQ_l), harmonic powers (H_1^h, H_2^h,$\cdots$, H_l^h), and fundamental DG output voltage magnitudes ($E_{mag,1}$, $E_{mag,2}$,$\cdots$, $E_{mag,l}$) to the microgrid central controller (MGCC). At the MGCC, the control signal for DG units to compensate frequency deviation is calculated as the following:

$$\Delta\omega = \frac{1}{l}\sum_{i=1}^{l} m_i P_i \tag{3.14}$$

Meanwhile, the compensation signal to eliminate the voltage magnitude deviation is produced by an integral controller:

$$\Delta E = k_E \int (E_0 - \bar{E}_{MG})dt \tag{3.15}$$

where k_E is the controller gain and $\bar{E}_{MG}$ is average voltage across the microgrid which is calculated as following:

Table 3.1: System Parameters.

System Parameter	Simulation	Experiment
LC filter, L_f; C_f	2.0 mH; 20 μF	1.3 mH; 10 μF
DC link voltage, V_{DC}	400 V	280 V
Nominal operating voltage, E_0	220 V, 60 Hz	110 V, 60 Hz
Switching frequency, f_{sw}	10 kHz	5 kHz

Droop Control	Coefficient	Simulation		Experiment		
				Case I	Case II	
		DG1=DG2	DG3=DG4	DG1=DG2=DG3	DG1=DG3	DG2
P-ω	$m\left(\frac{rad}{W \cdot s}\right)$	0.0015	0.00075	0.0015	0.0015	0.003
Q-V	$n\left(\frac{V}{Var}\right)$	0.0015	0.00075	0.001	0.001	0.002
H^h_{rated} (Var)		750	1500	700	700	350

Secondary & Virtual Impedance Control	Simulation	Experiment
Fund. virtual impedance control, $\bar{L}^f_v$; k_{LQ}	0.5 mH; 0.006	1.0 mH; 0.035
Har. virtual impedance control, k_{L3}; k_{L5}	0.00003; 0.00005	0.0002; 0.0005
Vol. restoration control, k_E	4.0	3.0

Double-Loop Voltage Control	Simulation	Experiment
K_{PV}; K_{Vf}; K_{Inner}	0.1; 30; 50	0.1; 20; 10
K_{Vh}	25 (h = 3); 20 (h = 5)	15 (h = 3); 10 (h = 5)
ω_c	10 rad/s	10 rad/s

$$\bar{E}_{MG} = \frac{1}{l}\sum_{i=1}^{l} E_{mag,i} \tag{3.16}$$

Moreover, the normalized reactive power and harmonic power are calculated as follows:

$$Q^f_{norm} = \frac{1}{l}\sum_{i=1}^{l} n_i Q_i \tag{3.17}$$

$$H^h_{norm} = \frac{1}{l}\sum_{i=1}^{l} \frac{H^h_i}{H^h_{rated,i}} \tag{3.18}$$

where $H^h_{rated,i}$ is the harmonic power rating of the ith DG unit.

Finally, compensation signals in (3.14), (3.15) and normalized powers in (3.17), (3.18) are periodically broadcasted to all DG units to perform control algorithm.

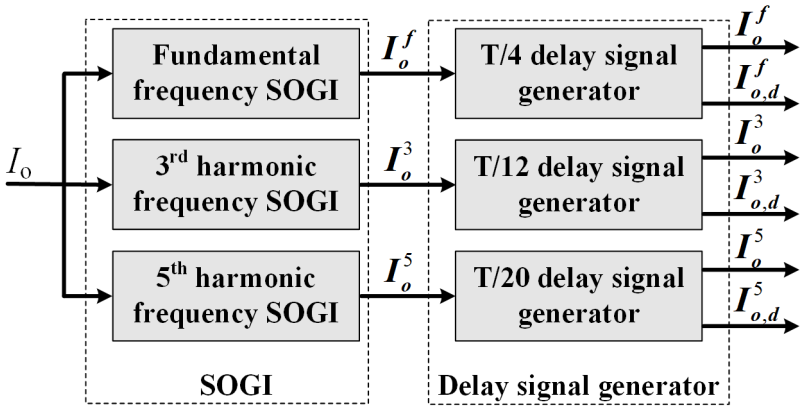

Figure 3.5: Decomposition of fundamental and harmonic components (T denotes the fundamental cycle time).

3.2.2 Local Controller

As shown in Fig. 3.4, the local controller consists of four main control parts to generate the desired output voltage for the DG unit: modified power calculation, modified droop control, selected virtual impedance control, and a double-loop voltage tracking scheme.

3.2.2.1 Modified DG unit Power Calculation

Fundamental and harmonic line current components, I_o^f and I_o^h, are extracted from the second order generalized integrator (SOGI) [38]. And, their conjugated signals, $I_{o,d}^f$ and $I_{o,d}^h$, are obtained by delaying I_o^f and I_o^h for a quarter fundamental and h-order harmonic cycle, respectively [39]. A simplified fundamental and harmonic extraction principle is sketched in Fig. 3.5.

Furthermore, since the voltage waveforms of DG units are harmonic polluted, the DG fundamental voltage should be also extracted together with harmonic current in order to calculate the DG power. For easy implementation without DG fundamental voltage extraction, we calculate the active and reactive power by using the fundamental voltage reference V_{ref}^f instead of the DG fundamental voltage V_o^f:

$$P = \frac{\omega_{LPF}}{2\left(s+\omega_{LPF}\right)}\left(V_{ref}^f I_o^f + V_{ref,d}^f I_{o,d}^f\right) \tag{3.19}$$

$$Q = \frac{\omega_{LPF}}{2\left(s+\omega_{LPF}\right)}\left(V_{ref,d}^f I_o^f - V_{ref}^f I_{o,d}^f\right) \tag{3.20}$$

where $V_{ref,d}^f$ is obtained by delaying the reference voltage V_{ref}^f for a quarter fundamental cycle; ω_{LPF} is the cutoff frequency of the low pass filter.

And, the h-order harmonic power of DG unit is calculated based on approximation

of $V^f_{o,rms} = E_0/\sqrt{2}$ and the h-order harmonic line current I^h_o and its conjugated signal $I^h_{o,d}$ [41, 67, 68]:

$$H^{h=3,5,\cdots} = V^f_{o,rms} I^h_{o,rms} = \frac{1}{2} E_0 \sqrt{(I^h_o)^2 + \left(I^h_{o,d}\right)^2} \tag{3.21}$$

where $V^f_{o,rms}$ and $I^h_{o,rms}$ are the rms values of the fundamental voltage and the h-order harmonic line current of DG unit, respectively.

Finally, the DG output voltage magnitude (E_{mag}) can be calculated from V^f_{ref} and $V^f_{ref,d}$:

$$E_{mag} = \sqrt{\left(V^f_{ref}\right)^2 + \left(V^f_{ref,d}\right)}. \tag{3.22}$$

3.2.2.2 Modified Droop Controller

From the compensation signals ($\Delta\omega$ and ΔE) from MGCC, the droop equations are modified to remove the deviations as follows:

$$\omega = \omega_0 - mP + \Delta\omega \tag{3.23}$$

$$E = E_0 - nQ + \Delta E \tag{3.24}$$

Because all DG units have same compensation signals ($\Delta\omega$ and ΔE), the secondary controller does not affect the power-sharing characteristics of the droop controller in both transient and steady state. On the other hand, since the whole system operates at the same frequency, accurate active power sharing is achievable with the droop control in the steady state, i.e., $m_i P_i = m_j P_j; \forall i, j$, and the following condition is satisfied from (3.14):

$$\Delta\omega = m_1 P_1 = m_2 P_2 = \cdots = m_l P_l. \tag{3.25}$$

Then, from (3.23) and (3.25), the control objective $\omega_i = \omega_0$ is obtained. As we can see, the compensation signal in (3.14) is simply calculated from only active powers without frequency detection as well as integral operation such as PI controller. Furthermore, the voltage compensation signal (ΔE) in (3.15) does not require any information about voltage at the PCC. Consequently, the frequency/voltage deviations are solved by the proposed secondary controller without any measurement or detection of the PCC voltage.

3.2.2.3 DG Virtual Impedance Control

The virtual impedance at fundamental sequence L_v^f consists of two components, the nominal inductance $\bar{L}_v^f$ and the adjustable inductance $\tilde{L}_v^f$:

$$L_v^f = \bar{L}_v^f + \tilde{L}_v^f. \tag{3.26}$$

In (3.26), $\bar{L}_v^f$ is a fixed one which is dedicated to ensuring the fundamental equivalent impedance inductive [69], and $\tilde{L}_v^f$ is adaptively regulated to eliminate the reactive power sharing errors by means of an integral controller:

$$\tilde{L}_v^f = k_{LQ} \int \left(nQ - Q_{norm}^f\right) dt \tag{3.27}$$

where k_{LQ} is the integral gain. Then, the virtual inductance is determined from (3.26) and (3.27), and the virtual resistance is obtained by empirically maintaining the virtual reactance-to-resistance ratio with five [19]:

$$\begin{aligned} L_v^f =& \bar{L}_v^f + k_{LQ} \int \left(nQ - Q_{norm}^f\right) dt, \\ R_v^f =& \frac{\omega L_v^f}{5}. \end{aligned} \tag{3.28}$$

Similarly, the virtual impedance at h-order harmonic frequency L_v^h is regulated to remove the respective harmonic power sharing errors as follows:

$$L_v^h = k_{Lh} \int \left(\frac{H^h}{H_{rated}^h} - H_{norm}^h\right) dt \tag{3.29}$$

where k_{Lh} is the integral gain.

From (3.28) and (3.29), it is obvious that the inputs of the integral controllers become zero at the steady state. Therefore, the following conditions are satisfied for l-DG system:

$$\begin{aligned} n_1 Q_1 =& n_2 Q_2 = \cdots = n_l Q_l = Q_{norm}^f, \\ \frac{H_1^h}{H_{rated,1}^h} =& \frac{H_2^h}{H_{rated,2}^h} = \cdots = \frac{H_l^h}{H_{rated,l}^h} = H_{norm}^h, \end{aligned} \tag{3.30}$$

which demonstrates that both accurate fundamental and h-order harmonic power sharing are achieved in the steady state, thanks to the virtual impedance control laws in (3.28) and (3.29).

Once the fundamental and h-order virtual impedances are determined, their associated

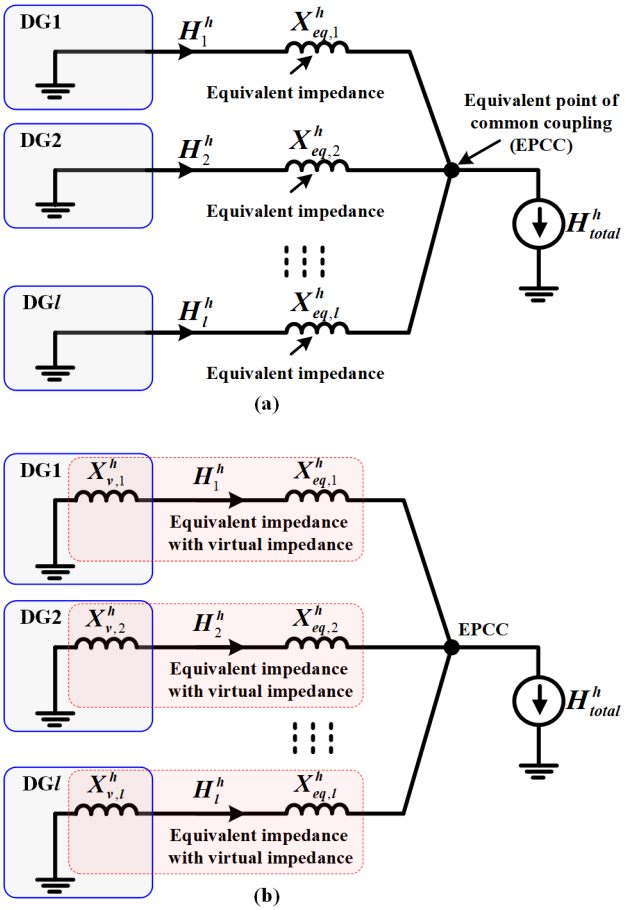

Figure 3.6: Equivalent model of the microgrid in Fig. 1 for h-order harmonic frequency: (a) without the virtual impedance; (b) with the virtual impedance.

voltage drops (V_v^f and V_v^h) are calculated as following:

$$V_v^f = R_v^f I_o^f - \omega L_v^f I_{o,d}^f, \tag{3.31}$$

$$V_v^h = -h\omega L_v^h I_{o,d}^h. \tag{3.32}$$

Then, the reference voltage for the double-loop voltage controller is modified as

$$\begin{aligned} V_{ref} =& V_{droop} - V_v^f - V_v^h \\ =& \underbrace{V_{droop} - \left(R_v^f I_o^f - \omega L_v^f I_{o,d}^f\right)}_{V_{ref}^f} + \underbrace{h\omega L_v^h I_{o,d}^h}_{V_{ref}^h}. \end{aligned} \tag{3.33}$$

3.2.2.4 Closed-Loop DG Voltage Control

In the double-loop voltage controller that generates the desired output voltage for DG unit with the voltage reference (V_{ref}) in (3.33), the outer loop uses proportional controller and multiple quasi–resonant (M-PR) controllers [23]:

$$G_{Vol}(s) = K_{PV} + \sum_{h=1,3,5,...} \frac{2K_{Vh}\omega_c s}{s^2 + 2\omega_c s + \omega_h^2} \tag{3.34}$$

where K_{PV} is the outer loop proportional gain, K_{Vh} is the resonant controller gain at the different frequencies, and ω_c is the cutoff frequency of the resonant controllers. The inner loop has a simple proportional control gain K_{Inner} with the filter inductor current feedback, which aims to provide sufficient damping to the output LC filter [23]:

$$G_{Cur}(s) = K_{Inner}. \tag{3.35}$$

3.2.3 Stability Analysis by Investigating the Effective Harmonic Impedance

It is pointed out that inserting the positive virtual impedance into the output of DG unit enhances the system stability, while inserting negative one may deteriorate the system stability because the equivalent feeder impedance may be negative [30, 69]. Therefore, to ensure the system stable, it is important to guarantee the equivalent feeder impedance positive regardless of inserting the negative virtual impedance [67]. In order to evaluate the stability, we investigate the equivalent feeder impedance for the meshed system with l DG units with arbitrary circuit configuration in Fig. 2.1.

The meshed microgrid in 2.1 is equivalently modelled as in Fig. 3.6(a) for h-order harmonic frequency in which the mismatched factors in the electrical distribution network in Fig. 2.1 are reflected into the mismatched equivalent feeder impedances ($X^h_{eq,i} > 0$, for $i = 1 \sim l$).

In case of the i-th DG unit, the parameters in (3.29) as $L^h_{v,i}$, H^h_i, and $H^h_{rated,i}$ are generalized. Then, with the virtual impedance in (3.29), the equivalent circuit in Fig. 3.6(a) becomes the circuit in Fig. 3.6(b) for h-order harmonic frequency. Then, the equivalent feeder impedance of the i-th DG unit, $\bar{X}^h_{eq,i}$, are given as $\bar{X}^h_{eq,i} = X^h_{v,i} + X^h_{eq,i}$, for $i = 1 \sim l$. And, the following relationship is satisfied to achieve the accurate harmonic power sharing at the steady state [39]:

$$\bar{X}^h_{eq,1} H^h_{rated,1} = \bar{X}^h_{eq,2} H^h_{rated,2} = \cdots = \bar{X}^h_{eq,l} H^h_{rated,l}. \tag{3.36}$$

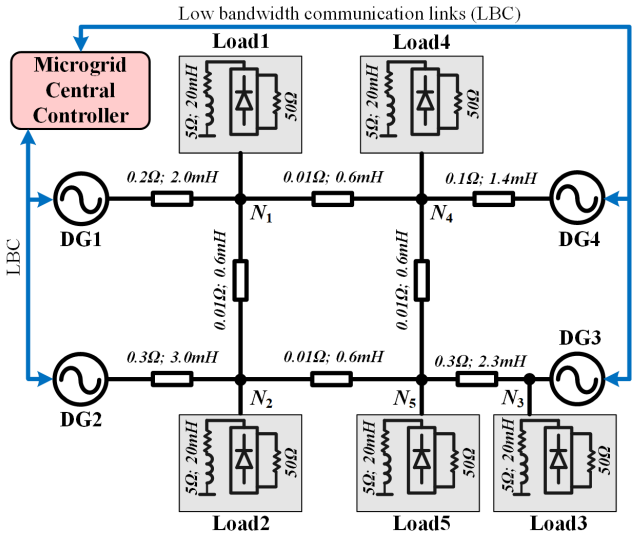

Figure 3.7: Meshed microgrid used in simulation.

From the equations (3.18) and (3.29), the sum of the virtual impedances of the l DG units in Fig. 3.6(b) becomes zero:

$$\sum_{i=1}^{l} X_{v,i}^{h} = jh\omega \sum_{i=1}^{l} L_{v,i}^{h} = jh\omega k_{Lh} \sum_{i=1}^{l} \int \left(\frac{H_i^h}{H_{rated,i}^h} - H_{norm}^h \right) dt = 0. \tag{3.37}$$

From (3.37), even though some DG virtual impedances are negative, there should exist at least one positive DG virtual impedance. If we assume that the virtual impedance of the j^{th} DG unit is positive ($X_{v,j}^h$), the equivalent feeder impedance of the j^{th} DG unit is also positive because $X_{eq,j}^h$ in Fig. 3.6(a) is always positive:

$$\bar{X}_{eq,j}^h = X_{v,j}^h + X_{eq,j}^h > 0. \tag{3.38}$$

Form (3.36) and (3.38), the following results are derived because $H_{rated,j}^h$ is positive:

$$\bar{X}_{eq,i}^h H_{rated,i}^h = \bar{X}_{eq,j}^h H_{rated,j}^h > 0, \; \forall i \in \{1, 2, ..., l\}. \tag{3.39}$$

From (3.39), the equivalent harmonic impedances of all DG units are always maintained positive because the harmonic rated powers are positive. Therefore, the system stability is always guaranteed with the proposed harmonic virtual impedance control method irrespective of the number of DG units and the microgrid structure.

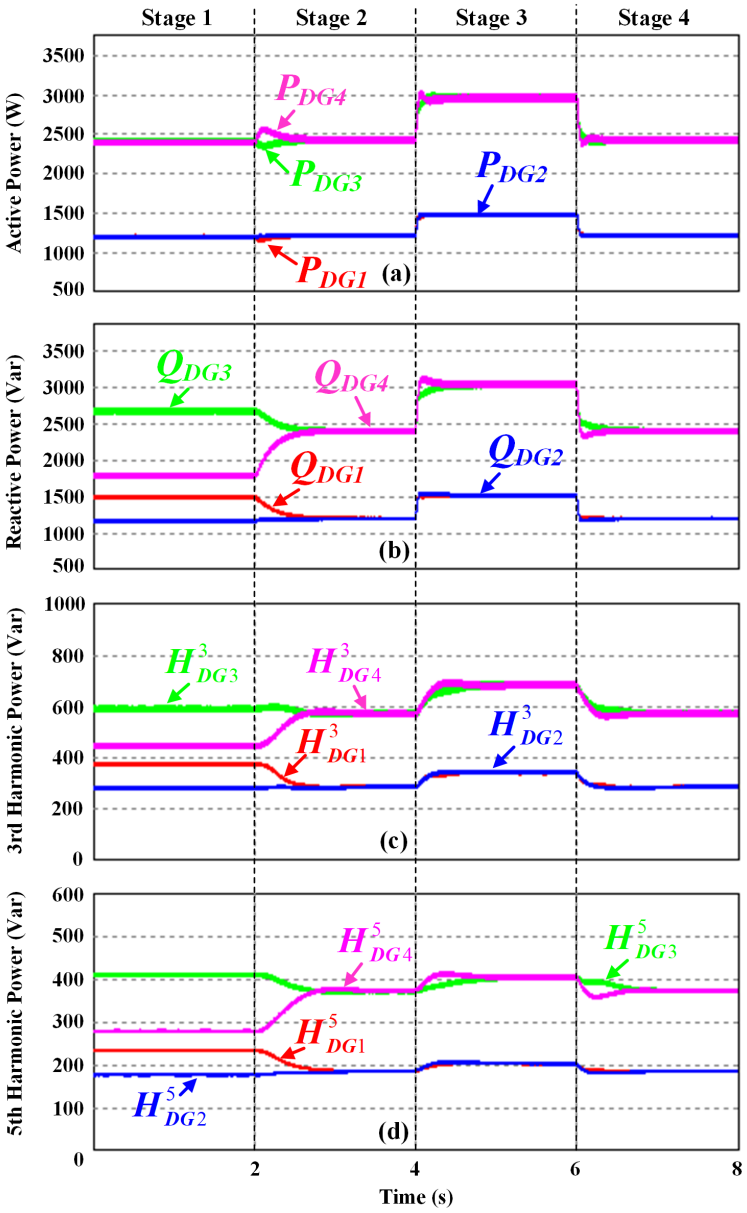

Figure 3.8: Simulated power sharing performance: (a) active power; (b) reactive power; (c) 3rd harmonic power; and (d) 5th harmonic power.

3.3 Simulation Results

The proposed control scheme is applied to an islanded meshed microgrid in Fig. 3.7, which is composed of four DG units and several linear and nonlinear loads. The simulation is done with the aid of the PSIM, and the system parameters are listed in Table 3.1. The information is broadcasted from the MGCC every $50ms$, and there exists $10ms$ delay in the communication links of DG units.

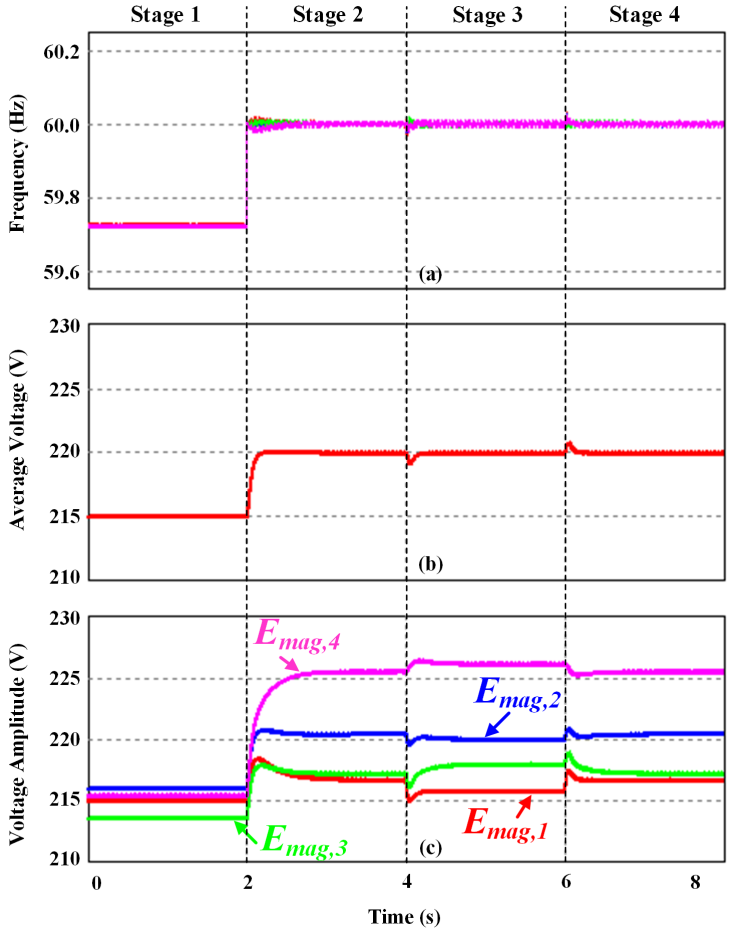

Figure 3.9: Simulated performance of the proposed secondary controller: (a) frequency; (b) average voltage; (c) DG output voltage magnitude.

The performance of the proposed method is shown in Figs. 3.8–3.10. During stage 1 ($0 < t < 2s$), the microgrid is originally operated with the conventional droop controller with various public loads $Load1$, $Load2$, and $Load4$ at nodes N_1, N_2, and N_4, respectively; and a local load, $Load3$, at node N_3. And also, 3rd and 5th order harmonics are selected as dominant harmonics to share the power. At $t = 2s$, the proposed control scheme is activated. $Load5$ is connected to and disconnected from node N_5 at $t = 4s$ and $6s$, respectively, which not only invokes a step load change but also changes the microgrid structure.

Fig. 3.8 demonstrates the power sharing performance with the proposed method. In stage 1, in spite of the accurate active power sharing in Fig. 3.8(a), the reactive, 3rd, and 5th harmonic power are not shared correctly with the conventional method as shown in Figs. 3.8(b)-3.8(d). However, with the proposed method from $2s$, those power sharing errors have been eliminated after a small transient duration, even though load condition or microgrid structure has changes in stage 3.

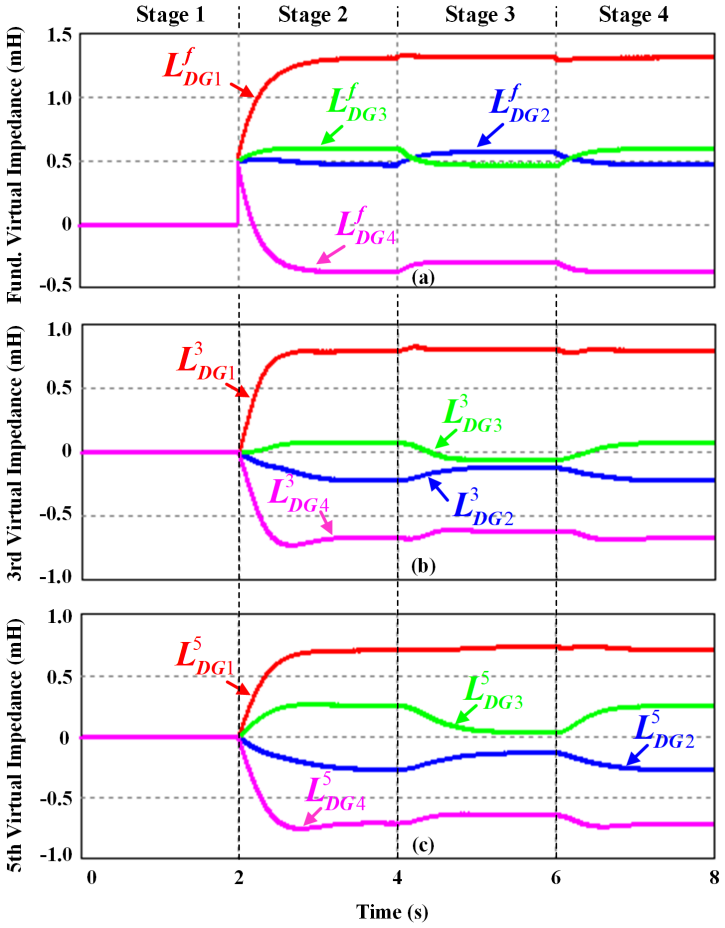

Figure 3.10: Variation of virtual inductances: (a) at fundamental frequency; (b) at 3rd harmonic frequency; (c) at 5th harmonic frequency.

Fig. 3.9 shows frequency/voltage restoration with the proposed secondary controller. During Stage 1, the frequency, fundamental average voltage, and fundamental output voltages of DG units are less than the nominal values as in Figs. 3.9(a), (b), and (c), respectively. When the proposed secondary controller is activated at $t = 2s$, the frequency and averaged voltage are boosted to the nominal values as in Figs. 3.9(a) and 3.9(b). Due to the mismatched line impedances, the DG output voltage magnitudes are slightly different each other. But they are adjusted around the nominal value within a proper margin (e.g., $\pm 5\%$ of the nominal voltage) as in Fig. 3.9(c).

Fig. 3.10 illustrates the variation of the virtual impedances for each DG unit: After the proposed control algorithm is applied at $t = 2s$, the fundamental, 3rd, and 5th harmonic virtual impedances are changed adaptively as shown in Figs. 3.10(a), (b), and (c), respectively. Consequently, the perfect linear and nonlinear power sharing are achieved regardless of the load condition or microgrid structure as clearly verified in Fig. 3.8.

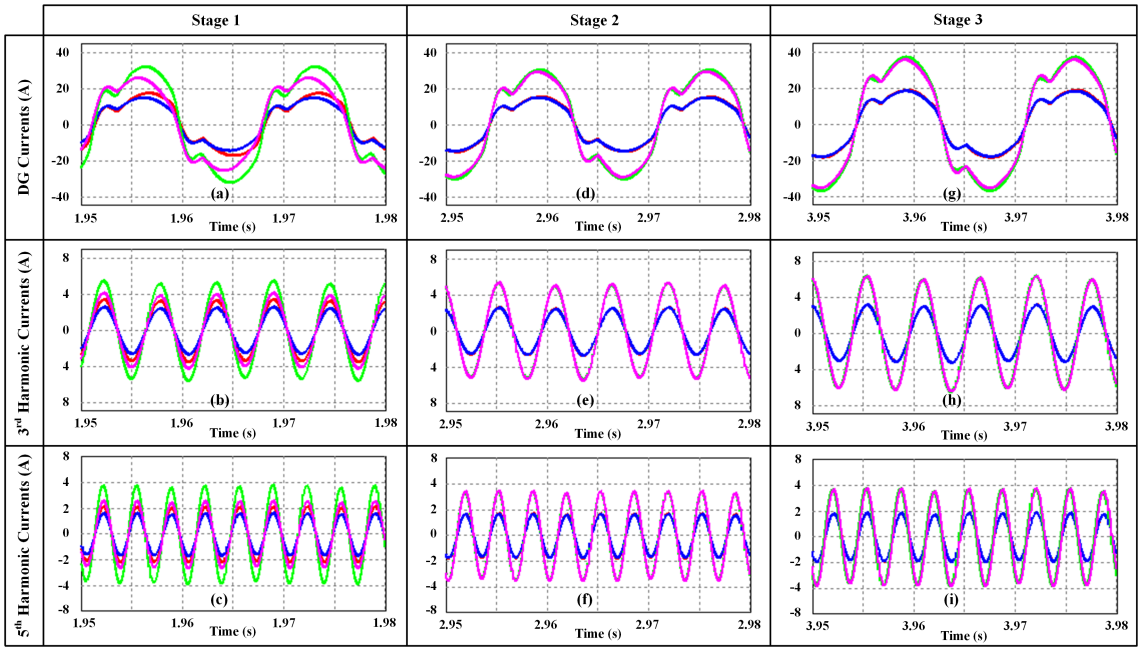

Figure 3.11: Harmonic components of DG currents. (a) DG out currents with conventional droop method. (b) 3rd harmonic currents with conventional droop method. (c) 5th harmonic currents with conventional droop method. (d) DG out currents with proposed method. (e) 3rd harmonic currents with proposed method. (f) 5th harmonic currents with proposed method. (g) DG out currents with proposed method with increased load. (h) 3rd harmonic currents with proposed method with increased load. (i) 5th harmonic currents with proposed method with increased load.

Fig. 3.11 shows the harmonic current-sharing waveforms with same color corresponding to the stages in Fig. 3.8: DG1 (red), DG2 (blue), DG3 (green), DG4 (magenta). As shown in Figs. 3.11(a)-(c), the harmonic current of the loads is not shared accurately among DG units with the conventional droop method in the stage 1. However, the accurate harmonic current sharing is realized once the proposed virtual impedance control method is utilized (Figs. 3.11[d]-[f]). And, the accurate current sharing is maintained even when the microgrid configuration is changed by applying a load (Figs. 3.11[g]-[i]).

Fig. 3.12 shows the performance of the system when a DG unit is sequentially disconnected from and reconnected to the multibus system in Fig. 3.7. At $t = 0$ in Fig. 3.12, the microgrid operates under the same condition of the stage 4 in Fig. 3.8. At $5s$ and $10s$, the DG2 is disconnected from and reconnected to the system, respectively. As shown in Fig. 3.12, irrespective of plug-and-play operation of DG unit, the proposed method shows a good dynamic performance similar to those in Figs. 3.8 and 3.9.

Fig. 3.13 shows the power sharing performance during communication interruption. In Fig. 3.13, the system in Fig. 3.7 is originally operated with the same operating

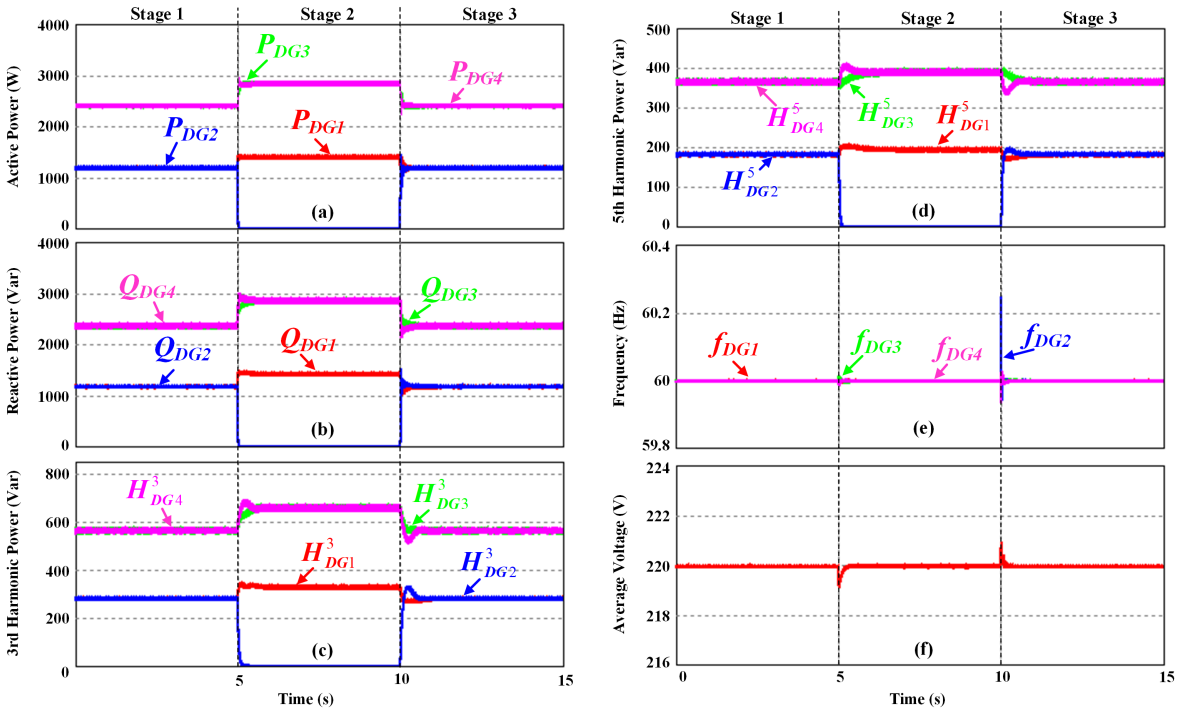

Figure 3.12: Simulation performance with the proposed controller under the plug-and-play operation. (a) Active power. (b) Reactive power. (c) Third harmonic power. (d) Fifth harmonic power. (e) Frequency. (f) Average value of the DG fundamental output voltages.

condition as the stage 4 in Fig. 3.8. When the communication fault occurs at $t = 5s$, all DG units stop regulating their virtual impedances and continue to operate with the fixed virtual impedance which is determined from the last regulation. As we can see, there is no change from 5 to $10s$ in the system, and the accurate power sharing is maintained despite the communication interruption. On the other hand, when $Load5$ is connected at $t = 10s$, the accurate power sharing is no longer guaranteed. However, the power sharing performance is much better than those in the stage 3 in Fig. 3.14 with the conventional droop control method under the same load condition. At $t = 15s$, the communication is restored, and the enhanced controller is reactivated. As shown in Fig. 3.13, the perfect power sharing is recovered with effective virtual impedance regulation.

3.4 Experimental Verification

In order to avoid hardware complexity, we used a simple down-scaled microgrid, shown in Fig. 3.15, which is enough to demonstrate the feasibility of the proposed control scheme. The system is controlled by the floating-point DSP (TMS320F28335 by Texas

Instruments) system. The data communication rate is the same as with the simulation, and the other parameters used in the experiment are listed in Table 3.1.

Two cases are investigated for the performance evaluation: the DGs in Fig. 3.15 have same power ratings (Case I) and different power ratings (Case II).

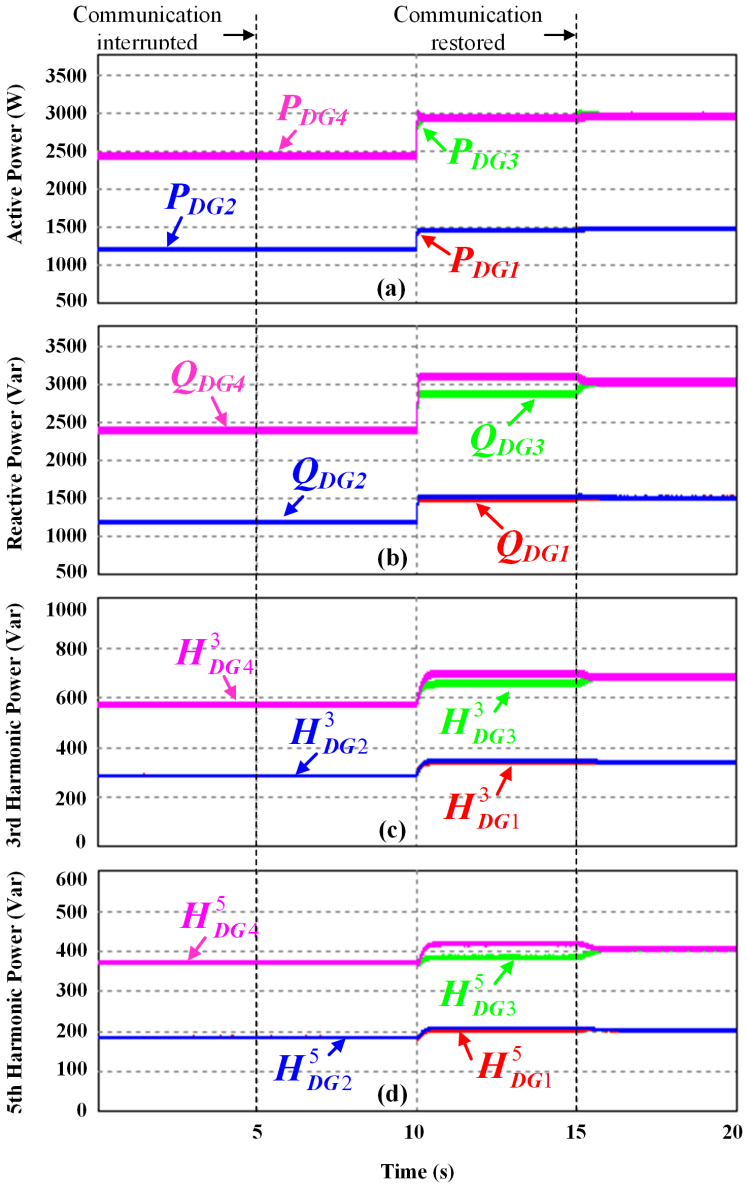

Figure 3.13: Simulated power sharing performance of the proposed controller before and after losing communication, and after recovering communication. (a) Active power. (b) Reactive power. (c) Third harmonic power. (d) Fifth harmonic power.

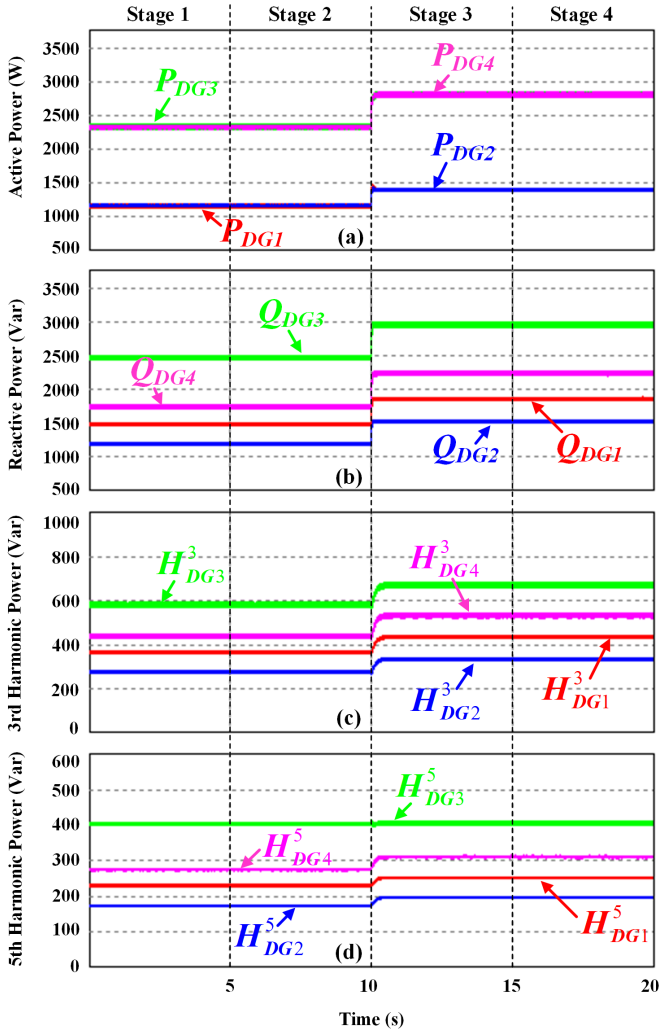

Figure 3.14: Simulated power sharing performance of the conventional droop controller. (a) Active power. (b) Reactive power. (c) Third harmonic power. (d) Fifth harmonic power.

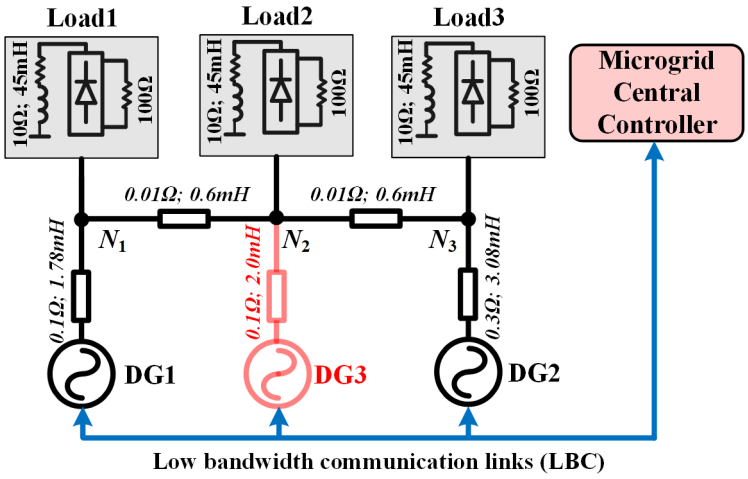

Figure 3.15: Meshed microgrid used in the experiment.

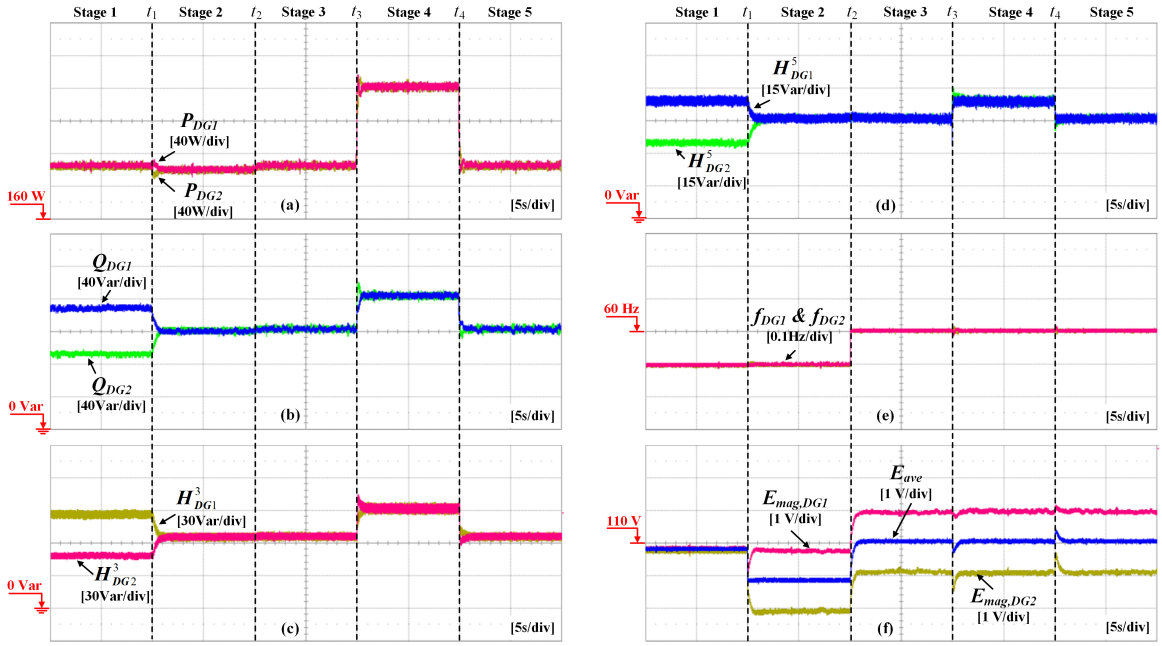

Figure 3.16: Experimental performance with the proposed controller (Case I). (a) Active power. (b) Reactive power. (c) Third harmonic power. (d) Fifth harmonic power. (e) Frequency. (f) Average and DG output voltage magnitudes.

3.4.1 Case I: Same Power Ratings

Fig. 3.16 shows the control performance of the proposed method. At the beginning, the microgrid is controlled by the conventional droop controller with DG units 1 and 2 (DG3 is disconnected) and with loads 1 and 2 at nodes, N_1 and N_2, respectively. As shown in Fig. 3.16, before $t = t_1$, the reactive load power (see Fig. 3.16[b]), 3rd and 5th harmonic powers (Figs. 3.16[c] and [d], respectively) are not equally shared between two DG units. On the other hand, when the proposed selected virtual impedance regulator is activated at t_1, accurate fundamental and selected dominant harmonic power sharing performance is achieved. Even when the secondary controller is activated at t_2 or when *Load*3 is connected to and disconnected from the system at t_3 and t_4, respectively, the perfect power sharing is always achieved for both linear and nonlinear loads, thanks to the proposed control scheme. As can be seen in Figs. 3.16(e) and (f), the frequency and fundamental output voltage of DG deviate from its nominal values in stage 1. Furthermore, the voltage deviation becomes more severe in the stage 2 due to the drop voltage across the fundamental virtual impedance (see Fig. 3.16[f]). However, once the proposed secondary controller is activated at $t = t_2$, the frequency and average voltage are restored to the nominal values while DG output voltage magnitudes are kept around the nominal value.

Fig. 3.17 demonstrates the DG current waveforms corresponding to the stages in

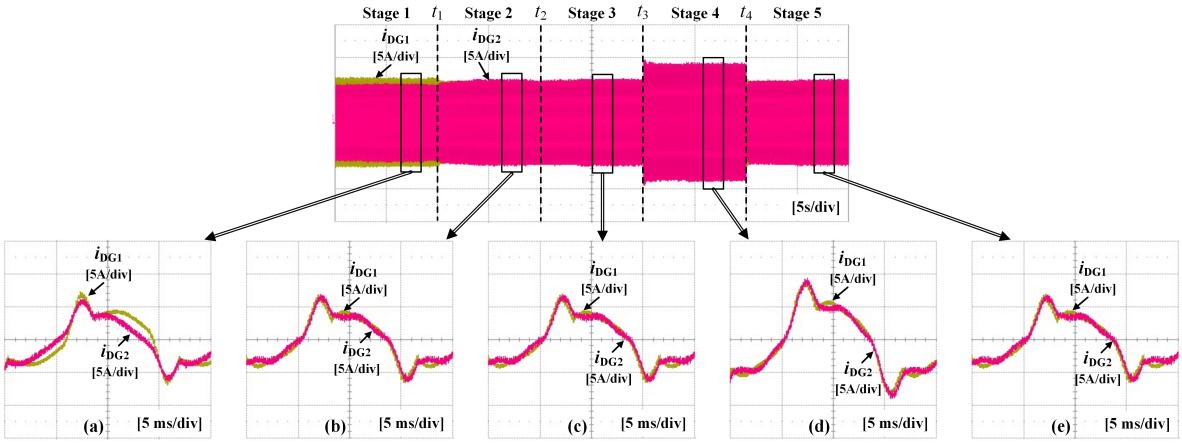

Figure 3.17: Zoomed-in view of DG current waveforms with (Case I). (a) Conventional droop method. (b) Proposed virtual impedance control method (activated at $t = t_1$). (c) Proposed secondary controller (activated at $t = t_2$). (d) Proposed method with increased load (Load3 is connected at $t = t_3$). (e) Proposed method with decreased load (Load3 is disconnected at $t = t_4$).

Fig. 3.16. In Fig. 3.17(a), the magnitude and phase of the DG currents are not the same with the conventional droop method. But, they become nearly the same once the proposed virtual impedance control method is utilized (Fig. 3.17[b]). And, the secondary controller has no effect on the power sharing performance (Fig. 3.17[c]). Additionally, the DG currents with the same magnitudes are maintained even when the microgrid configuration is changed by applying a load (Fig. 3.17[d]) or disconnecting a load (Fig. 3.17[e]).

Fig. 3.18 shows the control performance with the proposed method under the plug-and-play operation of DG unit. In Fig. 3.18, the system originally operates under the same condition of the stage 5 in Fig. 3.16. The DG3 is connected to and disconnected from system at t_5 and t_6, respectively. As clearly shown in Fig. 3.18, the proposed method guarantees the accurate power sharing and restorations of voltage and frequency even with plug-and-play operation of a DG unit.

3.4.2 Case II: Different Power Ratings

Fig. 3.19 shows the control performance with the proposed method with different power ratings for DG units shown in Fig. 3.15, and the waveforms correspond to those in Fig. 3.16. As shown in Fig. 3.19, the proposed method provides a good performance similar to those with the same DG units, irrespective of different power ratings.

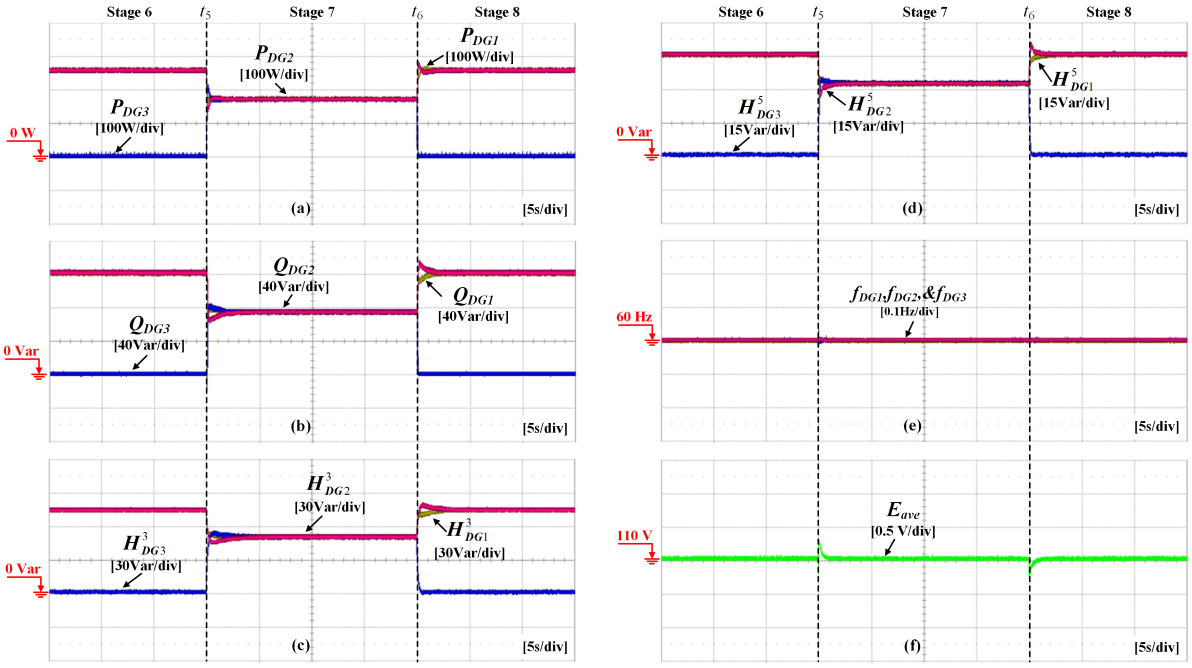

Figure 3.18: Experimental performance with the proposed controller under the plug-and-play operation (Case I). (a) Active power. (b) Reactive power. (c) Third harmonic power. (d) Fifth harmonic power. (e) Frequency. (f) Average value of the DG fundamental output voltages.

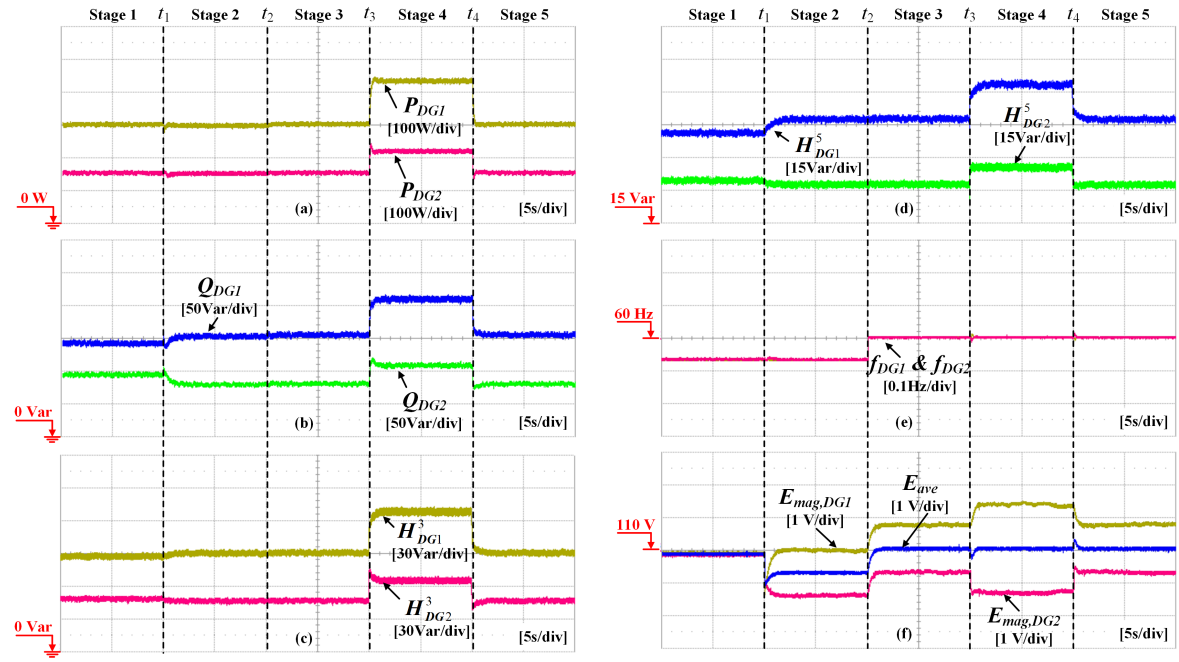

Figure 3.19: Experimental performance with the proposed controller (Case II). (a) Active power. (b) Reactive power. (c) Third harmonic power. (d) Fifth harmonic power. (e) Frequency. (f) Average and DG output voltage magnitudes.

3.5 Conclusion of the Chapter

In this chapter, we propose an enhanced control scheme to achieve accurate power sharing along with no frequency/voltage deviations in the islanded multibus microgrids. In the proposed control scheme, the virtual impedances at fundamental and selected harmonic frequencies are adaptively regulated to achieve accurate active, reactive, and harmonic power sharing, and the secondary controller is developed to restore the frequency and voltage deviations caused by droop equations and virtual impedances. With the proposed method, accurate power sharing and no frequency/voltage deviation are always obtained in spite of the microgrid configuration or load condition changes. Moreover, the proposed control method does not require any information about the feeder impedances, detailed microgrid configuration, load powers, or the PCC voltage information, so it is very suitable for complex microgrid systems. Simulation and experimental results have been also provided to verify the effectiveness of the proposed control strategy.

Chapter 4

PCC Voltage Harmonic Compensation Strategy

In case of voltage harmonic compensation at the point of common coupling (PCC) in islanded microgrids, it is important to share the harmonic load power correctly among the distributed generators (DGs) to use the DGs' capacity effectively. In previous DG control schemes, it is impossible to satisfy the requirements of PCC voltage quality and accurate harmonic power sharing simultaneously with only a virtual impedance controller (VIC). In this chapter, we propose an enhanced DG VIC to provide accurate harmonic power sharing along with voltage harmonic compensation in islanded microgrids. The proposed VIC is developed based on simple integral controllers with two controllable parts and no information about the feeder impedances or load currents. The control performance is theoretically analyzed using a small-signal state-space model to evaluate the system dynamics and stability. The feasibility and effectiveness of the method are validated by simulated and experimental results.

Section 4.1 describes the system configuration and analyses of the power sharing control and the PCC voltage harmonics attenuation by using virtual impedance. Section 4.2 presents the proposed virtual impedance controller. The simulation and experimental results are shown in sections 4.3 and 4.4, and concluding remarks are presented in section 4.5.

4.1 Islanded Microgrid Analysis

Fig. 4.1 shows a simplified diagram of an islanded microgrid, where n DG units are interfaced to the PCC through different DG feeders. Each DG unit consists of a DC source, an inverter, and an LC filter. The microgrid also includes several linear and nonlinear loads placed at the PCC. In a practical microgrid, the nonlinear load is significant, so it

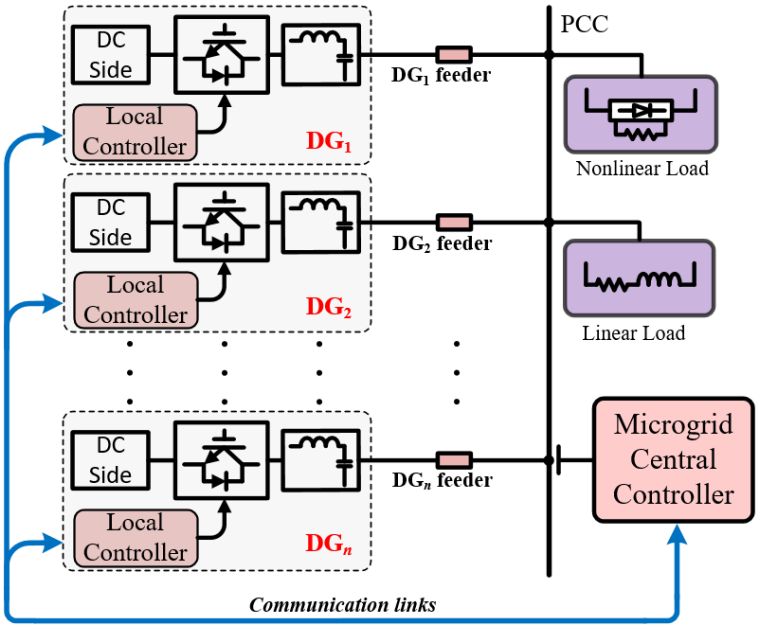

Figure 4.1: Configuration of the islanded microgrid.

is important to maintain accurate harmonic power sharing and high PCC voltage quality, besides accurate fundamental power sharing for the islanded microgrid.

4.1.1 Active and Reactive Power Sharing

In islanded microgrids, the i^{th} DG unit ($i = 1, \cdots, n$) is conventionally controlled by the $P - \omega$ and $Q - E$ droop controllers:

$$\omega_i = \omega_0 - m_i P_i, \tag{4.1}$$

$$E_i = E_0 - n_i Q_i, \tag{4.2}$$

where ω_0 and E_0 are the nominal values of the DG angular frequency and DG voltage magnitude, P_i and Q_i are the measured real and reactive powers after the low pass filter (LPF), and m_i and n_i are the real and reactive power droop slopes of the DG unit, respectively. From (4.1) and (4.2), the output of the droop controller $v_{droop,i}$ is obtained as follows [19, 23]:

$$v_{droop,i} = E_i sin\left(\int \omega_i dt\right). \tag{4.3}$$

With the conventional droop controller, accurate active power sharing is always achieved, but accuracy in reactive power sharing cannot be provided due to the mismatch in feeder impedances. To realize accurate reactive power sharing, the fundamental virtual

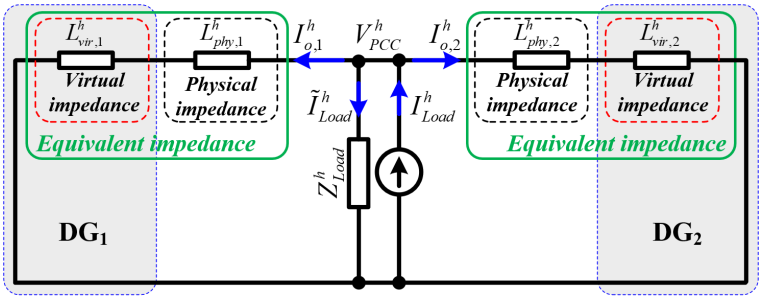

Figure 4.2: Equivalent circuit of two DG units at h-order harmonic frequency.

impedance $L^f_{vir,i}$ is applied [19]. Then, the reference signal from the droop controller is modified as follows:

$$v^f_{ref,i} = v_{droop,i} - v^f_{vir,i} = E_i sin\left(\int \omega_i dt\right) + \omega_i L^f_{vir,i} i^f_{od,i}, \tag{4.4}$$

where $v^f_{ref,i}$ is the DG fundamental voltage reference for the voltage controller, and $i^f_{od,i}$ is the conjugated signal of the DG fundamental current $i^f_{o,i}$, which is obtained by delaying $i^f_{o,i}$ for one quarter of the fundamental cycle [20].

4.1.2 Harmonic Power Sharing Analysis

Fig. 4.2 shows the equivalent circuit of an islanded microgrid with two DG units at h-order harmonic frequency. The DG unit is represented as an adjustable virtual impedance $L^h_{vir,i}$, and the nonlinear load is considered as a current source I^h_{Load} and a passive load Z^h_{Load} [41, 59]. $L^h_{phy,i}$ is the physical impedance between DGi and PCC [20].

From Fig. 4.2, the DG equivalent impedance $L^h_{eq,i}$ at the h-order harmonic frequency becomes:

$$L^h_{eq,i} = L^h_{vir,i} + L^h_{phy,i}. \tag{4.5}$$

The DG harmonic current magnitude $I^h_{o,i}$ is determined as:

$$I^h_{o,i} = \frac{V^h_{PCC}}{h\omega L^h_{eq,i}} \tag{4.6}$$

where V^h_{PCC} is the PCC harmonic voltage magnitude, and ω is the angular system frequency.

According to the IEEE 1459-2010 standard [68], the DG harmonic power H^h_i is calculated as:

$$H_i^h = \frac{1}{2} V_{o,i}^f I_{o,i}^h \approx \frac{1}{2} E_0 I_{o,i}^h \tag{4.7}$$

where $V_{o,i}^f$ is the DG fundamental voltage magnitude. Equation (4.8) is obtained by substituting (4.6) into (4.7):

$$H_i^h = \frac{E_0 V_{PCC}^h}{2h\omega L_{eq,i}^h}. \tag{4.8}$$

For the system with two identical DG units in Fig. 4.2, the power sharing error (ΔH_{12}^h) is obtained from (4.8):

$$\Delta H_{12}^h = H_1^h - H_2^h = \frac{E_0 V_{PCC}^h \left(L_{eq,2}^h - L_{eq,1}^h\right)}{2h\omega L_{eq,1}^h L_{eq,2}^h}. \tag{4.9}$$

In (4.9), the power sharing error is eliminated ($\Delta H_{12}^h = 0$) if the DG equivalent feeder impedances are equal ($L_{eq,1}^h = L_{eq,2}^h$). Fortunately, from (4.5), the DG equivalent impedance $L_{eq,i}^h$ is controllable by the DG virtual impedance $L_{vir,i}^h$. Therefore, by properly regulating the DG virtual impedances, the mismatch in feeder impedances can be compensated to realize accurate harmonic power sharing.

4.1.3 PCC Voltage Harmonic Compensation Analysis

From Fig. 4.2, the h-order harmonic voltage at PCC is obtained as (4.10) by considering that Z_{Load}^h is much higher than $h\omega L_{eq,1}^h$ and $h\omega L_{eq,2}^h$:

$$V_{PCC}^h = \frac{I_{Load}^h}{\frac{1}{h\omega L_{eq,1}^h} + \frac{1}{h\omega L_{eq,2}^h}} = \frac{h\omega I_{Load}^h}{\frac{1}{L_{eq,1}^h} + \frac{1}{L_{eq,2}^h}}. \tag{4.10}$$

Equation (4.10) demonstrates that it is possible to attenuate the PCC voltage harmonic V_{PCC}^h by minimizing the DG equivalent impedances $L_{eq,1}^h$ and $L_{eq,2}^h$. Fortunately, from (4.5), the DG equivalent impedances $L_{eq,1}^h$ and $L_{eq,2}^h$ can be reduced if the DG virtual impedances $L_{vir,1}^h$ and $L_{vir,2}^h$ are assigned negative values. Therefore, the PCC voltage quality can be enhanced by means of negative virtual impedances.

4.2 Proposed Virtual Harmonic Impedance Scheme

Proper DG virtual impedances can simultaneously improve the harmonic power sharing and attenuate the PCC voltage harmonics, but the virtual impedance technique has mainly been used for harmonic power sharing. There has been no virtual impedance

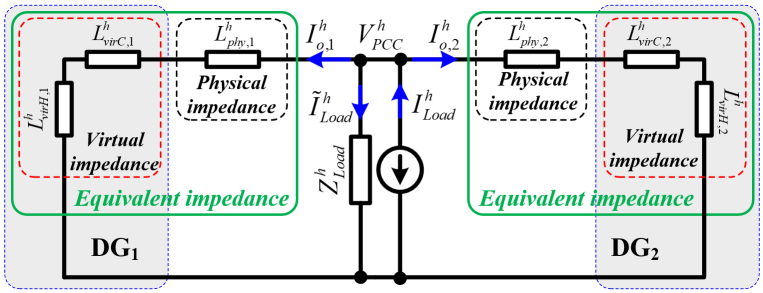

Figure 4.3: Equivalent circuit of two DG units at h-order harmonic frequency with the proposed virtual harmonic impedance.

control scheme that can simultaneously solve the issues of harmonic power sharing and PCC voltage quality. Therefore, an enhanced control scheme is proposed, which carries out two functions through only one virtual impedance control loop.

4.2.1 Proposed Virtual Impedance with Two Controllable Parts

To realize accurate harmonic power sharing and PCC voltage quality enhancement, the i^{th} DG virtual harmonic impedance ($L^h_{vir,i} = 1, \cdots, n$) contains two controllable parts:

$$L^h_{vir,i} = L^h_{virH,i} + L^h_{virC,i}, \tag{4.11}$$

where $L^h_{virH,i}$ is used for accurate harmonic power sharing and $L^h_{virC,i}$ is a negative inductance for improving the PCC voltage quality. With the proposed virtual impedance in (4.11), the microgrid in Fig. 4.2 is represented as in Fig. 4.3. The DG equivalent harmonic impedance becomes the following:

$$L^h_{eq,i} = L^h_{virH,i} + L^h_{virC,i} + L^h_{phy,i}. \tag{4.12}$$

To achieve accurate harmonic power sharing, $L^h_{eq,1}$ and $L^h_{eq,2}$ are designed to keep the DG equivalent harmonic impedances equal:

$$L^h_{eq,1} = L^h_{eq,2} \Leftrightarrow L^h_{virH,1} + L^h_{virC,1} + L^h_{phy,1} = L^h_{virH,2} + L^h_{virC,2} + L^h_{phy,2}. \tag{4.13}$$

By using the virtual impedances with $L^h_{virH,1} = -L^h_{virH,2}$ [20], the solution to (4.13) is:

$$\begin{cases} L^h_{virH,1} = \frac{(L^h_{phy,2} - L^h_{phy,1}) + (L^h_{virC,2} - L^h_{virC,1})}{2}, \\ L^h_{virH,2} = \frac{(L^h_{phy,1} - L^h_{phy,2}) + (L^h_{virC,1} - L^h_{virC,2})}{2}. \end{cases} \tag{4.14}$$

The h-order harmonic voltage at the PCC in Fig. 4.3 is determined as:

$$V_{PCC}^{h} = h\omega L_{eq,i}^{h} I_{o,i}^{h}. \tag{4.15}$$

From (4.15), the PCC voltage harmonic is reduced to the desired value $V_{PCC,ref}^{h}$ by using the following equivalent impedances $L_{eq,i}^{h}$ in (4.12):

$$L_{eq,i}^{h} = L_{virH,i}^{h} + L_{virC,i}^{h} + L_{phy,i}^{h} = \frac{V_{PCC,ref}^{h}}{h\omega I_{o,i}^{h}}. \tag{4.16}$$

When harmonic power sharing is realized by the virtual impedances in (4.14), (4.17) is satisfied:

$$I_{o,1}^{h} = I_{o,2}^{h} = \frac{I_{Load}^{h}}{2}. \tag{4.17}$$

Substituting (4.17) into (4.16) leads to:

$$L_{eq,i}^{h} = L_{virH,i}^{h} + L_{virC,i}^{h} + L_{phy,i}^{h} = \frac{2V_{PCC,ref}^{h}}{h\omega I_{Load}^{h}}. \tag{4.18}$$

The harmonic compensating parts of the virtual impedances, $L_{virC,i}^{h}$ are made equal for two DG units:

$$L_{virC,1}^{h} = L_{virC,2}^{h}. \tag{4.19}$$

Then, (4.14) becomes:

$$\begin{cases} L_{virH,1}^{h} = \frac{L_{phy,2}^{h} - L_{phy,1}^{h}}{2}, \\ L_{virH,2}^{h} = \frac{L_{phy,1}^{h} - L_{phy,2}^{h}}{2}. \end{cases} \tag{4.20}$$

$L_{virC,1}^{h}$ and $L_{virC,2}^{h}$ are determined from (4.18) – (4.20):

$$L_{virC,1}^{h} = L_{virC,2}^{h} = \frac{2V_{PCC,ref}^{h}}{h\omega I_{Load}^{h}} - \frac{L_{phy,1}^{h} + L_{phy,2}^{h}}{2}. \tag{4.21}$$

Finally, by substituting (4.20) and (4.21) into (4.11), the DG virtual impedances to achieve harmonic power sharing and harmonics compensation are:

$$\begin{cases} L_{vir,1}^{h} = \frac{2V_{PCC,ref}^{h}}{h\omega I_{Load}^{h}} - L_{phy,1}^{h}, \\ L_{vir,2}^{h} = \frac{2V_{PCC,ref}^{h}}{h\omega I_{Load}^{h}} - L_{phy,2}^{h}. \end{cases} \tag{4.22}$$

As shown in (4.22), it is possible to find $L_{vir,1}^{h}$ and $L_{vir,2}^{h}$ that simultaneously satisfy the conditions in (4.13) and (4.16) with given values of $L_{phy,1}^{h}$, $L_{phy,2}^{h}$, and I_{Load}^{h}. Therefore, DG virtual impedances can be used to realize harmonic power sharing and PCC voltage

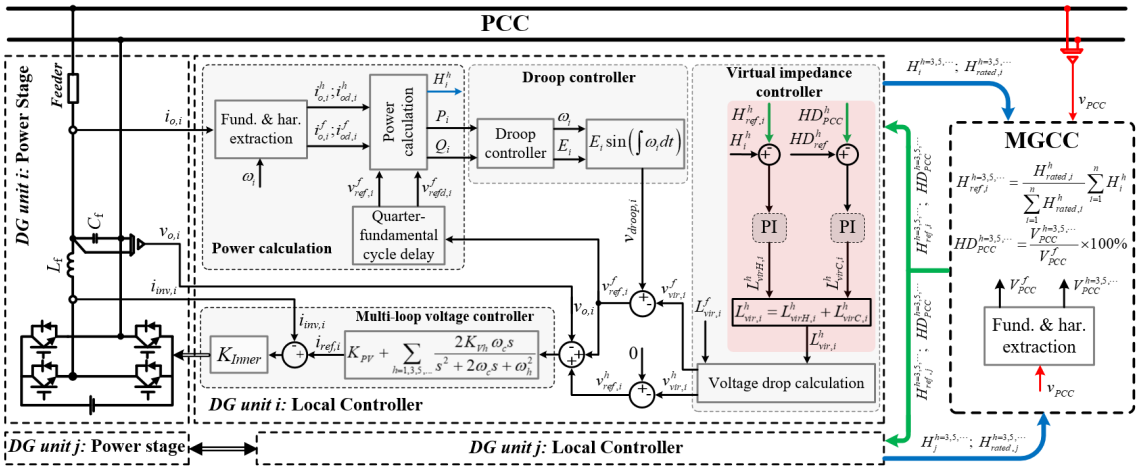

Figure 4.4: Proposed control scheme.

quality enhancement.

4.2.2 Proposed Virtual Harmonic Impedance Controller

Fig. 4.4 shows the proposed control scheme to regulate $L^h_{virH,i}$ and $L^h_{virC,i}$ without information about the feeder impedances and load current. The DG units transmit information related to the h-order harmonic power to the microgrid's central controller (MGCC). The MGCC calculates the harmonic power reference $H^h_{ref,i}$ for the DG unit in (4.23) and sends it back to each DG unit:

$$H^h_{ref,i} = \frac{H^h_{rated,i}}{\sum_{i=1}^{n} H^h_{rated,i}} \sum_{i=1}^{n} H^h_i, \tag{4.23}$$

where $H^h_{rated,i}$ is the DGi harmonic power rating. Each DG unit uses the received harmonic power reference to adaptively adjust the first virtual impedance part $L^h_{virH,i}$ by using an integral controller:

$$L^h_{virH,i} = k^h_H \int \left(H^h_i - H^h_{ref,i}\right) dt \tag{4.24}$$

where k^h_H is the integral gain.

In addition, the MGCC extracts the individual components of the PCC voltage and calculates the h-order harmonic distortion HD^h_{PCC} as follows:

$$HD^h_{PCC} = \frac{V^h_{PCC}}{V^f_{PCC}} \times 100\% \tag{4.25}$$

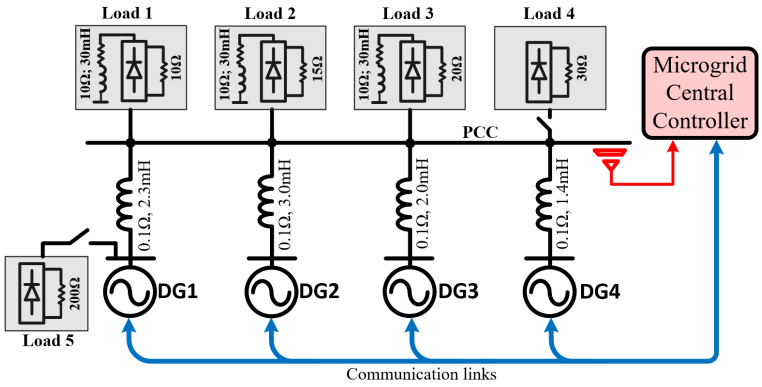

Figure 4.5: The islanded microgrid used for small-signal analysis and simulations.

where V^h_{PCC} and V^f_{PCC} are the magnitudes of the h-order harmonic and fundamental PCC voltage, respectively. Then, HD^h_{PCC} is broadcast to DG units to perform the control algorithm. From HD^h_{PCC}, the DG's local controller regulates its second virtual impedance part $L^h_{virC,i}$ to maintain the harmonic distortion at the desired level HD^h_{ref} by means of the following integral controller:

$$L^h_{virC,i} = \frac{k^h_C}{H^h_{rated,i}} \int \left(HD^h_{ref} - HD^h_{PCC}\right) dt \tag{4.26}$$

where k^h_C is the integral gain.

Finally, by substituting (4.24) and (4.26) into (4.11), the virtual impedance at the h-order harmonic frequency is obtained:

$$L^h_{vir,i} = k^h_H \int \left(H^h_i - H^h_{ref,i}\right) dt + \frac{k^h_C}{H^h_{rated,i}} \int \left(HD^h_{ref} - HD^h_{PCC}\right) dt. \tag{4.27}$$

Once the virtual harmonic impedance in (4.27) is determined, its associated voltage drop $v^h_{vir,i}$ is calculated as follows:

$$v^h_{vir,i} = -h\,\omega_i\, L^h_{vir,i}\, i^h_{od,i}. \tag{4.28}$$

Then, the harmonic voltage reference for the voltage controller is modified to implement the virtual harmonic impedance:

$$v^h_{ref,i} = 0 - v^h_{vir,i} = h\,\omega_i\, L^h_{vir,i}\, i^h_{od,i}. \tag{4.29}$$

Next, a multi-loop voltage controller [20, 23] is applied to generate the desired output voltage for a DG unit with the voltage reference in (4.4) and (4.29).

Table 4.1: System Parameters

System parameter	Simulation	Experiment
LC filter, L_f/C_f	1.3 mH/ 10 μF	1.3 mH/ 10 μF
DC link voltage, V_{dc}	400 V	280 V
Nominal voltage, E_0	220 V, 60 Hz	110 V, 60 Hz
Switching frequency, f_{sw}	10 kHz	10 kHz
Power Control	**Simulation**	**Experiment**
	DG1=DG2 / **DG3=DG4**	**DG1=DG2**
m (rad/W·s)	0.001 / 0.0005	0.0015
n (V/Var)	0.005 / 0.0025	0.0025
H^3_{rated} (Var)	750 / 1500	200
H^5_{rated} (Var)	750 / 1500	200
Double-Loop Voltage Control	**Simulation**	**Experiment**
$K_{PV}/K_{V1}/K_{Inner}$	0.1/ 40/ 30	0.1/ 30/ 25
K_{V3}/K_{V5}	25/ 20	15/ 10
ω_b	4.1 rad/s	4.1 rad/s
Virtual Impedance Control	**Simulation**	**Experiment**
$k^3_H/\ k^3_C$	0.000015/ 20	0.0002/ 5
$k^5_H/\ k^5_C$	0.00035/ 35	0.00035/ 7
$HD^{h=3,5}_{ref}$	1%	1%

4.2.3 Small-Signal Stability Analysis

The system dynamic performance and stability were investigated based on a small-signal state-space model [34, 70]. To guarantee that the harmonic power and the harmonic distortion are ripple-free, (4.7) and (4.25) are rewritten using a low-pass filter (LPF):

$$H_i^h = \frac{\omega_{LPF} E_0}{2\,(s+\omega_{LPF})} I_{o,i}^h, \tag{4.30}$$

$$HD_{PCC}^h = \frac{100\omega_{LPF}}{(s+\omega_{LPF})\,V_{PCC}^f} V_{PCC}^h, \tag{4.31}$$

where ω_{LPF} is the cutoff angular frequency of the LPF. By linearizing (4.30) and (4.31), the small-signal variations of the harmonic power (ΔH_i^h) and the harmonic distortion (ΔHD_{PCC}^h) are obtained as follows:

$$\Delta H_i^h = \frac{\omega_{LPF} E_0}{2\,(s+\omega_{LPF})} \Delta I_{o,i}^h, \tag{4.32}$$

$$\Delta HD_{PCC}^h = \frac{100\omega_{LPF}}{(s+\omega_{LPF})\,V_{PCC}^f} \Delta V_{PCC}^h, \tag{4.33}$$

where the operator Δ denotes a small-signal disturbance around the system equivalent point.

The small-signal variation of the DG equivalent feeder impedance, $\Delta L_{eq,i}^h$, can be

obtained by small-signal analysis after substituting (4.24) and (4.26) into (4.12):

$$\Delta L^h_{eq,i} = \frac{1}{s}\left(k^h_H\,\Delta H^h_i - \frac{k^h_C}{H^h_{rated,i}}\Delta HD^h_{PCC}\right). \tag{4.34}$$

Similarly, the small-signal variation of the DG harmonic current, $\Delta I^h_{o,i}$, is obtained from (4.15):

$$\Delta I^h_{o,i} = \frac{1}{h\omega L^h_{eq,i}}\Delta V^h_{PCC} - \frac{V^h_{PCC}}{h\omega (L^h_{eq,i})^2}\Delta L^h_{eq,i}. \tag{4.35}$$

Equation (4.10) becomes (4.36) for a microgrid with n DG units:

$$V^h_{PCC} = \frac{h\omega I^h_{Load}}{\frac{1}{L^h_{eq,1}} + \frac{1}{L^h_{eq,2}} + \cdots + \frac{1}{L^h_{eq,n}}}. \tag{4.36}$$

The small-signal variation of the PCC harmonic voltage, ΔV^h_{PCC}, is obtained by linearizing (4.36):

$$\Delta V^h_{PCC} = \alpha_1 \Delta L^h_{eq,1} + \alpha_2 \Delta L^h_{eq,2} + \cdots + \alpha_n \Delta L^h_{eq,n}, \tag{4.37}$$

where $\alpha_i = \partial V^h_{PCC}/\partial L^h_{eq,i}, i = 1, 2, \cdots, n$.

By manipulating equations (4.32) to (4.37), the small-signal state-space model of the proposed control system becomes:

$$\dot{x}_{MG} = A_{MG} x_{MG} \tag{4.38}$$

where $x_{MG} = [\Delta L^h_{eq,1}\ \Delta L^h_{eq,2}\ \cdots\ \Delta L^h_{eq,n}\ \Delta H^h_1\ \Delta H^h_2\ \cdots\ \Delta H^h_n\ \Delta HD^h_{PCC}]^T$ and A_{MG} is given in the Appendix B.

Based on the small-signal state-space model in (4.38), the system dynamics and stability of the proposed controller are considered using a microgrid with four DG units, as shown in Fig. 4.5. The system parameters are listed in Table 4.1. The impact of the control gains on the system dynamics was investigated using root locus diagrams with different k^3_H and k^3_C, as illustrated in Figs. 4.6 and 4.7.

Fig. 4.6 shows the trajectories of all eigenvalues obtained when increasing the gain k^3_H from 0 to 0.000018 with small intervals. The dynamic performance is mainly determined by the dominant poles $\lambda_1 - \lambda_3$ and $\lambda_7 - \lambda_9$ because the other poles $\lambda_4 - \lambda_6$ are fixed, and these poles move along the direction of the arrows as k^3_H increases. In Fig. 4.6, the control system is stable because all the eigenvalues remain in the left-haft plane. Fig. 4.7 shows the root locus diagram for different k^3_C from 0 to 50. In Fig. 4.7, the increase of k^3_C mainly influences the eigenvalues λ_1 and λ_8. Figs. 4.6 and 4.7 show that when increasing

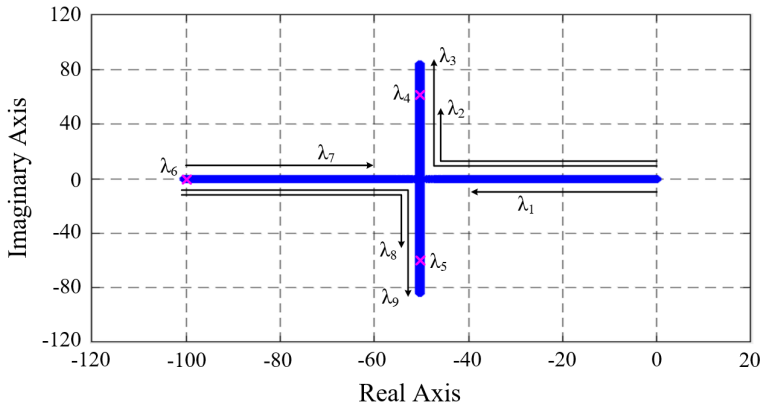

Figure 4.6: Root locus diagram according to control gain k_H^3 with: $0 < k_H^3 < 0.000018$, $\omega_{LPF} = 100 rad/s$ and $k_C^3 = 20$.

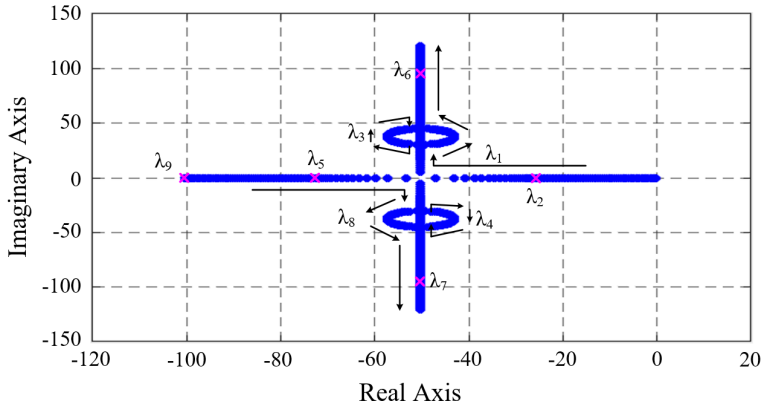

Figure 4.7: Root locus diagram according to control gain k_C^3 with: $0 < k_C^3 < 50$, $\omega_{LPF} = 100 rad/s$ and $k_H^3 = 0.000015$.

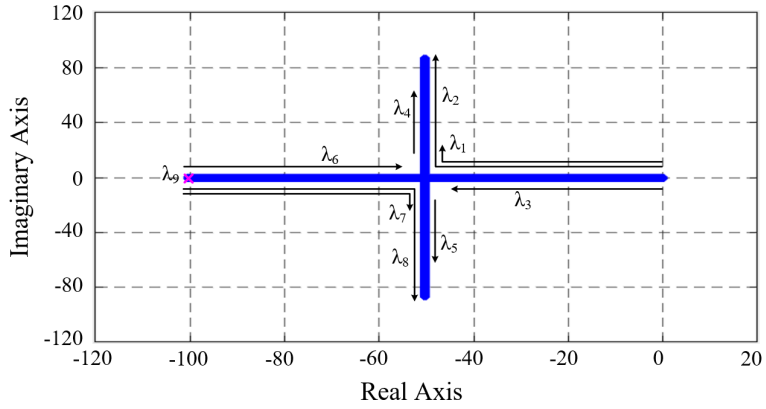

Figure 4.8: Root locus diagram according to control gain k_H^5 with: $0 < k_H^5 < 0.0005$, $\omega_{LPF} = 100 rad/s$ and $k_C^5 = 35$.

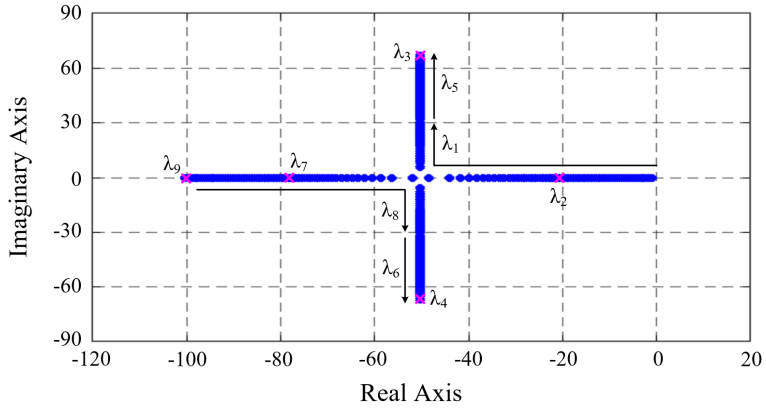

Figure 4.9: Root locus diagram according to control gain k_C^5 with: $0 < k_C^5 < 80$, $\omega_{LPF} = 100 rad/s$ and $k_H^5 = 0.00035$.

the gains, the system stability is improved with faster dynamics, but the system becomes underdamped. Therefore, the desired system damping and stability performance were obtained by selecting values of 0.000015 and 20 for the 3rd harmonic virtual impedance control gains, k_H^3 and k_C^3. Similarly, the 5th harmonic virtual impedance control gains, k_H^5 and k_C^5, were chosen as 0.00035 and 35 based on the system dynamics in Figs. 4.8 and 4.9, respectively.

4.2.4 Stability with Communication Delay

When considering communication delay $\tau > 0$ in communication links, the small-signal variation of DG equivalent feeder impedance in (4.34) becomes:

$$\Delta L_{eq,i}^h = \frac{1}{s}\left(k_H^h \, \Delta H_i^h - \frac{k_C^h}{H_{rated,i}^h} \Delta H D_{PCC\_d}^h\right) \tag{4.39}$$

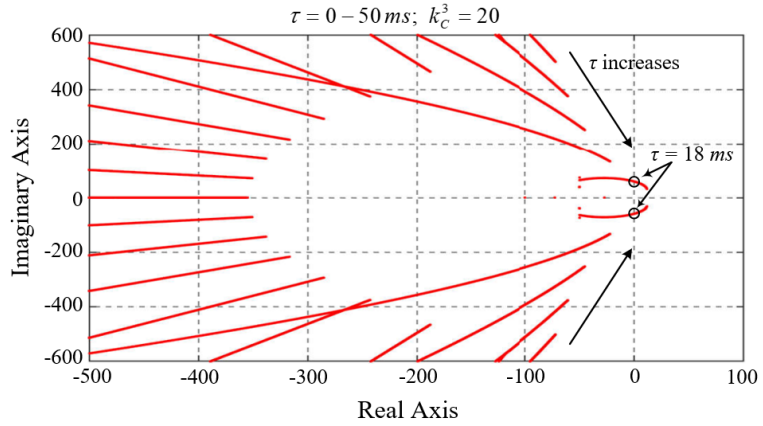

Figure 4.10: Root locus diagram according to communication delay τ: $0 \leq \tau \leq 50ms$, $k_C^3 = 20$, $k_H^3 = 0.000015$, and $\omega_{LPF} = 100rad/s$.

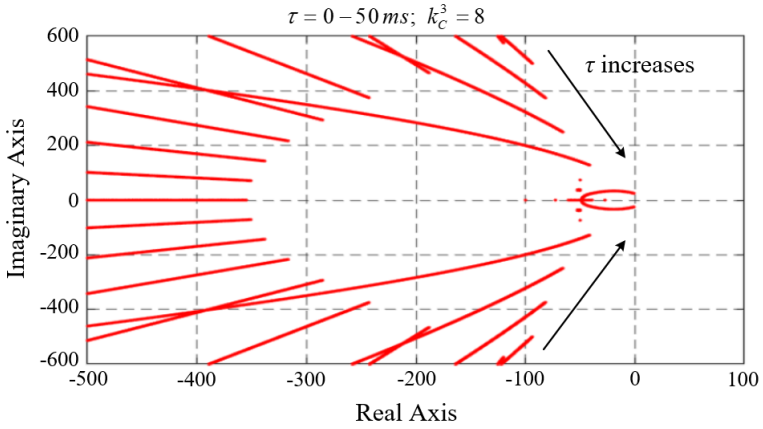

Figure 4.11: Root locus diagram according to communication delay τ: $0 \leq \tau \leq 50ms$, $k_C^3 = 8$, $k_H^3 = 0.000015$, and $\omega_{LPF} = 100rad/s$.

where $HD^h_{PCC\_d} = HD^h_{PCC\_d}(t-\tau)$. Therefore, the small-signal state-space model of the proposed control system in (4.38) is rewritten as follows:

$$\dot{x}_{MG} = \Omega_{MG}\, x_{DG} + \Omega_{MG\_d}\, x_{MG\_d} \tag{4.40}$$

where $x_{MG\_d} = [\Delta L^h_{eq,1\_d}\ \Delta L^h_{eq,2\_d} \cdots\ \Delta L^h_{eq,n\_d}\ \Delta H^h_{1\_d}\ \Delta H^h_{2\_d} \cdots\ \Delta H^h_{n\_d}\ \Delta HD^h_{PCC\_d}]^T$ and the state matrixes Ω_{MG} and Ω_{MG_d} are given in the Appendix B.

The characteristic equation for the system in (4.40) becomes [65]:

$$\det\left(-sI + \Omega_{MG} + \Omega_{MG\_d} e^{-s\tau}\right) = 0. \tag{4.41}$$

It is difficult to find the exact characteristic roots of the system in (4.40) because the characteristic equation in (4.41) has infinite solutions. The eigenvalues of (4.41) are obtained for a specific communication delay from the previous numerical approach

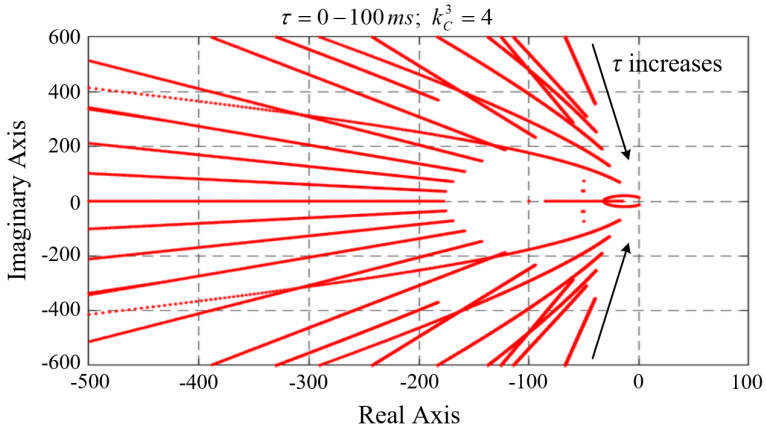

Figure 4.12: Root locus diagram according to communication delay τ: $0 \leq \tau \leq 100ms$, $k_C^3 = 4$, $k_H^3 = 0.000015$, and $\omega_{LPF} = 100rad/s$.

in [65], and Fig. 4.10 shows the trajectories of all eigenvalues for the system in Fig. 4.5 by increasing the communication delay τ from 0 to $50ms$. The eigenvalues approach the right haft plane as the communication delay increases, and they remain in the left haft plane until $\tau = 18ms$. Therefore, the system stability is guaranteed with the communication time delay $10ms$ which is used in simulation and experiment.

Additionally, Fig. 4.11 displays the root locus by increasing the communication delay τ from 0 to $50ms$ with smaller gain $k_C^3 = 8$. As we can see, all poles in the unstable area in Fig. 4.10 ($k_C^3 = 20$) are moved to the stable area. Furthermore, in case of $k_C^3 = 4$, the system is still stable even when $\tau = 100ms$ (Fig. 4.12). Figs. 4.7 and 4.10-4.12 demonstrate that a larger gain provides a faster dynamic response while a smaller gain help to stabilize the system against communication delays.

4.3 Simulation Results

We validated the proposed control scheme using an islanded microgrid with four DG units, four loads 1 - 4 at PCC, and one local load at DG1, as shown in Fig. 4.5. To show the effectiveness of the control scheme for different DG power ratings, the rated powers of DGs 3 and 4 are twice that of DGs 1 and 2. A simulation was carried out using PSIM software, and the system parameters are listed in Table 4.1. The information is broadcast from the MGCC every $10ms$.

4.3.1 Control Performance with the Proposed Method

The control performance of the proposed method is shown in Figs. 4.13-4.18 for three simulation stages. Stage 1 occurs at $0 - 5s$, where the microgrid is originally operated

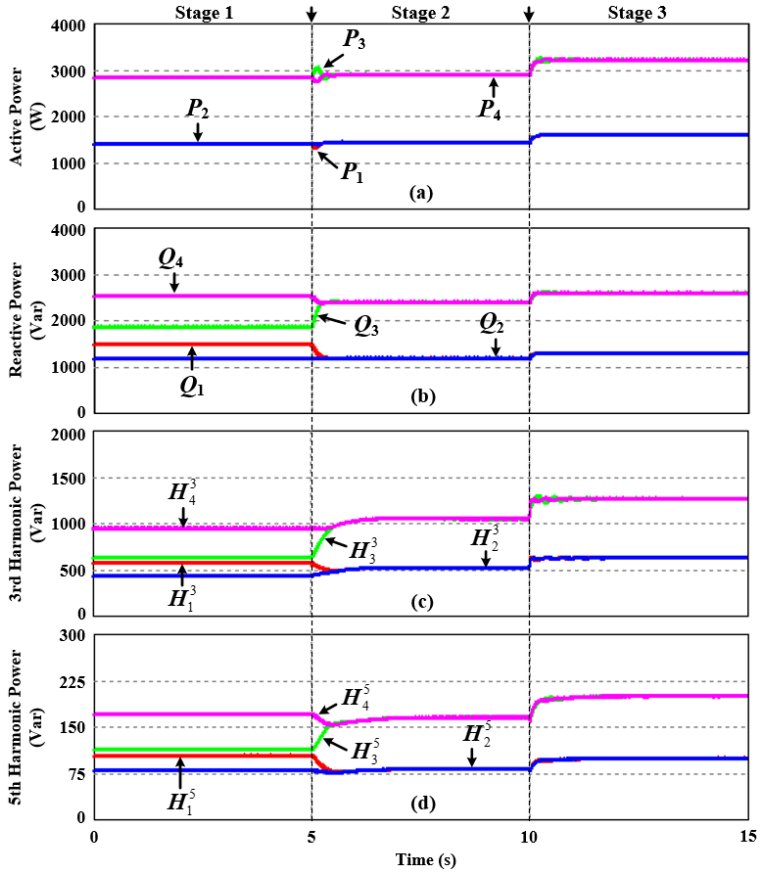

Figure 4.13: Simulated power sharing performance: (a) active power; (b) reactive power; (c) 3rd harmonic power; (d) 5th harmonic power.

with the conventional droop controller with Loads $1-3$. Stage 2 occurs from $5-10s$, and the proposed virtual impedance controller is activated at $5s$. Stage 3 occurs at $10-15s$, where Load 4 is connected to the system at $10s$.

Fig. 4.13 shows the power sharing performance with the proposed method. Despite accurate active power sharing in stage 1 in Fig. 4.13(a), the reactive, 3rd, and 5th harmonic powers are not shared accurately with the conventional droop method (see Figs. 4.13(b)-(d)). Nevertheless, when the proposed method is applied at $5s$, the power sharing errors are eliminated after short transient periods. Perfect fundamental and harmonic power sharing is always maintained even when the load condition is changed in stage 3 (see Figs. 4.13(a)-(d)).

Fig. 4.14 shows the DG current waveforms corresponding to each stage in Fig. 4.13. Using the conventional droop method in stage 1, the harmonic load current is not shared accurately among DG units (see Fig. 4.14(a)). But accurate harmonic current sharing is achieved once the proposed method is applied irrespective of the load variation in stage 3 (see Figs. 4.14(b) and (c)).

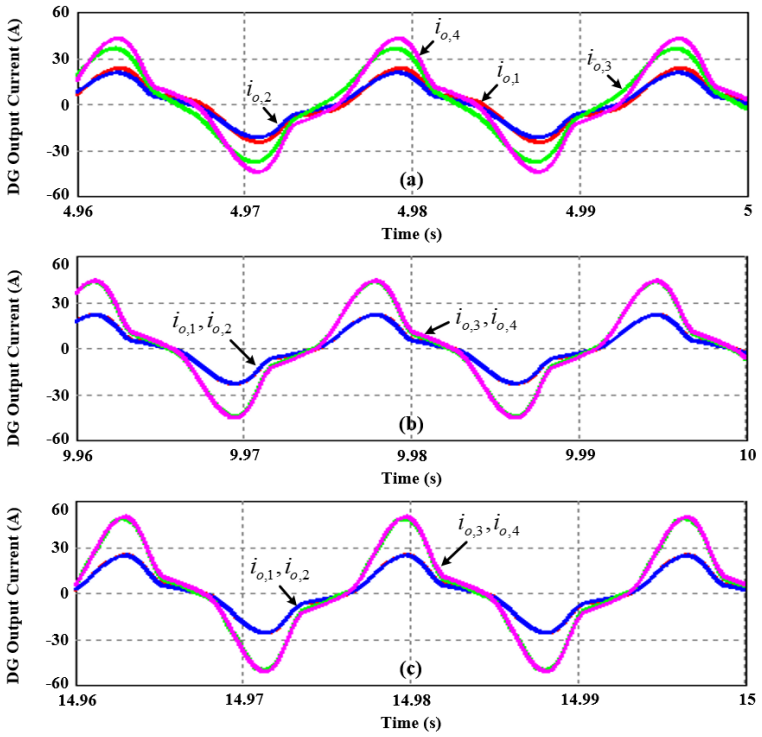

Figure 4.14: Zoon-in DG current waveforms corresponding to stages in Fig. 4.10: (a) stage 1; (b) stage 2; (c) stage 3.

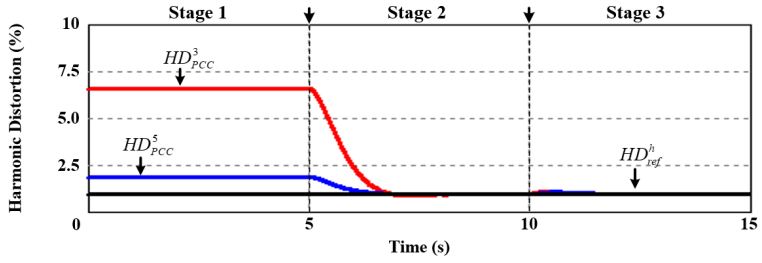

Figure 4.15: PCC harmonic distortion indexes.

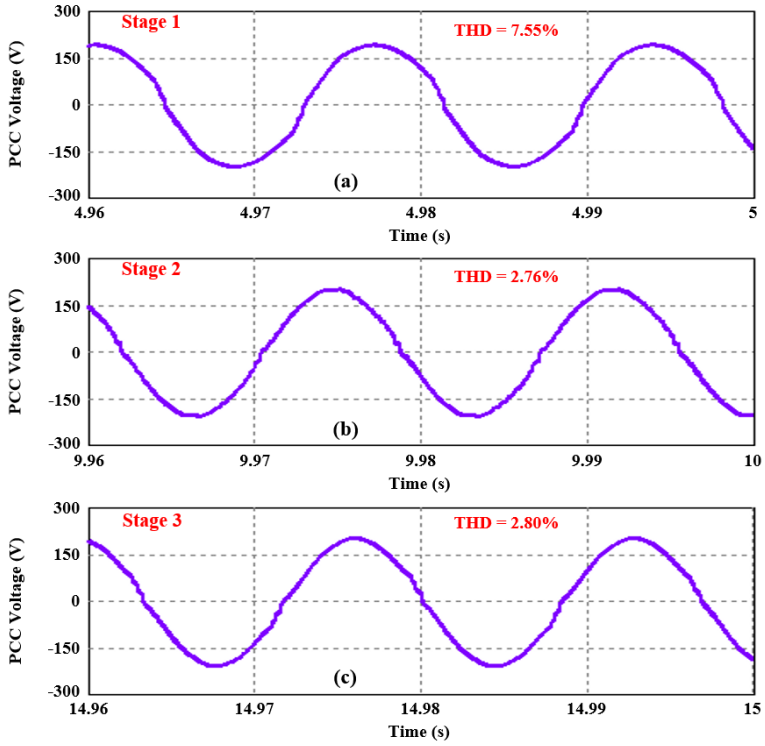

Figure 4.16: Zoon-in PCC voltage waveforms corresponding to stages in Fig. 4.10: (a) stage 1; (b) stage 2; (c) stage 3.

Figs. 4.15 and 4.16 demonstrate the PCC voltage harmonic compensation with the proposed controller. In stage 1, the harmonic distortions (HD^h_{PCC} are 6.80% and 2% for the 3rd and 5th harmonics, respectively (see Fig. 4.15). The PCC voltage is highly distorted with THD = 7.55% (see Fig. 4.16(a)). Nevertheless, when the proposed method is activated at $5s$, the harmonic distortions are reduced to the desired values $HD^h_{PCC,ref}$ = 1% (see Fig. 4.15). Consequently, the PCC voltage becomes nearly sinusoidal with a low THD of 2.76% (see Fig. 4.16(b)). The PCC voltage quality is always maintained even when load 4 is applied in stage 3 thanks to the proposed control scheme (see Figs. 4.15 and 4.16(c)).

Fig. 4.17 illustrates the output voltage waveforms for each DG unit corresponding to the stages in Fig. 4.13: DG1 (red), DG2 (blue), DG3 (green), and DG4 (magenta). The DG output voltages are properly distorted to achieve the sinusoidal PCC voltage, as shown in Figs. 4.15 and 4.16. Fig. 4.18 shows the variation of the virtual impedances for each DG unit: after the proposed virtual impedance controller is activated at $5s$, the DG virtual impedances at the selected 3rd and 5th harmonics are adaptively regulated (see Figs. 4.18(a) and (b)). Consequently, perfect power sharing and PCC voltage quality enhancement are realized simultaneously regardless of the load condition, as shown in Figs. 4.13, 4.15, and 4.16.

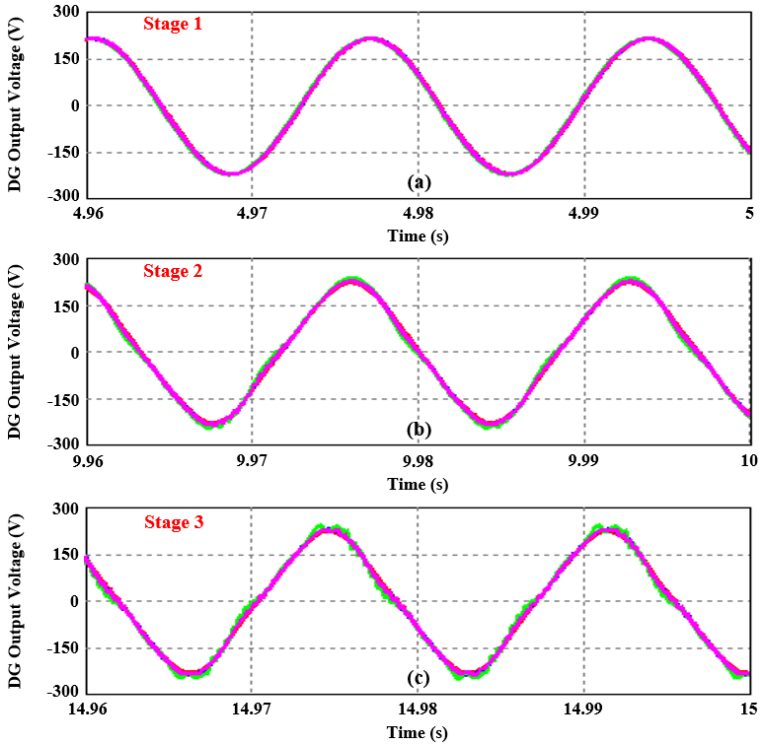

Figure 4.17: Zoon-in DG output voltage waveforms corresponding to stages in Fig. 4.10: (a) stage 1; (b) stage 2; (c) stage 3.

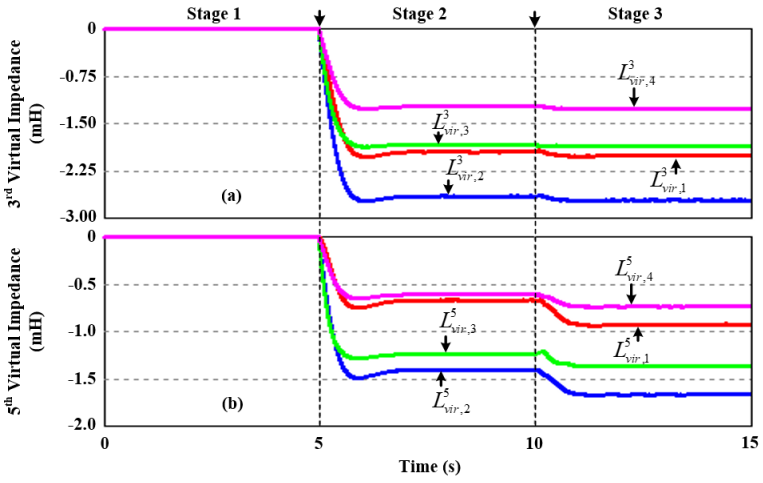

Figure 4.18: Variations of DG virtual impedances: (a) at 3rd harmonic frequency; (b) at 5th harmonic frequency.

Table 4.2: Comparison of the control performance in each stage

	Stage 1	Stage 2	Stage 3
Power sharing accuracy	Low	High	High
PCC voltage quality	Low	High	High

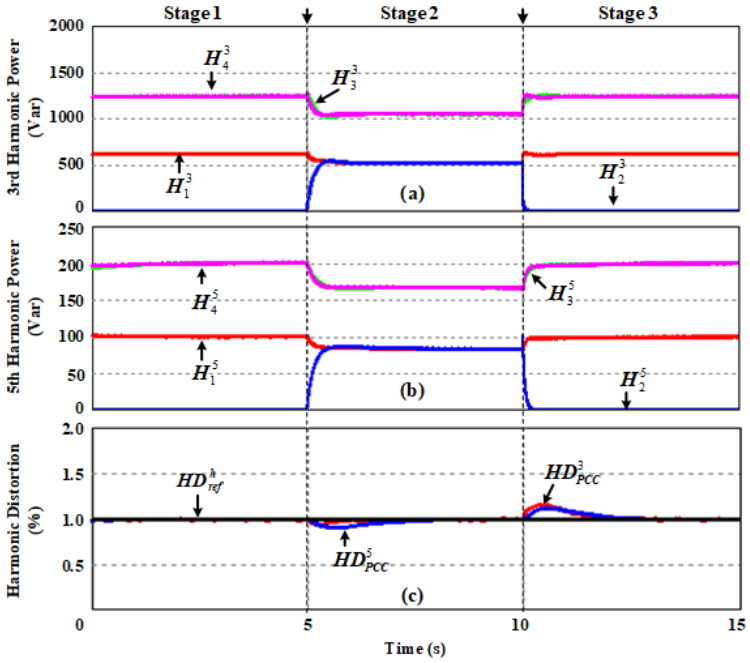

Figure 4.19: Control performance under plug-and-play operation: (a) 3rd harmonic power; (b) 5th harmonic power; (c) harmonic distortion.

The control performance in each stage in Figs. 4.13–4.18 is summarized Table 4.2. As shown in Table 4.2, in stage 1 with conventional droop controller, the power sharing performance is poor with low PCC voltage quality. However, the proposed method provides remarkable power sharing accuracy and PCC voltage quality regardless of the load conditions in stages 2 and 3.

4.3.2 Plug-and-Play Operation

Fig. 4.19 demonstrates the performance of the system when a DG unit is sequentially connected to and disconnected from the microgrid system in Fig. 4.5. At $t = 0$, the microgrid operates with the proposed method with DG units 1, 3, and 4. At $5s$ and $10s$, DG2 is connected to and disconnected from the system, respectively. Regardless of the plug-and-play operation of DG2, the proposed control method shows good performance similar to that in Figs. 4.13 and 4.15.

4.3.3 Effect of Communication Delay

The dynamic responses of the DG harmonic powers and the PCC harmonic distortions for various communication delays and control gains when the proposed method is activated are shown in Fig. 4.20. As shown in Fig. 4.20, with small communication delays, the

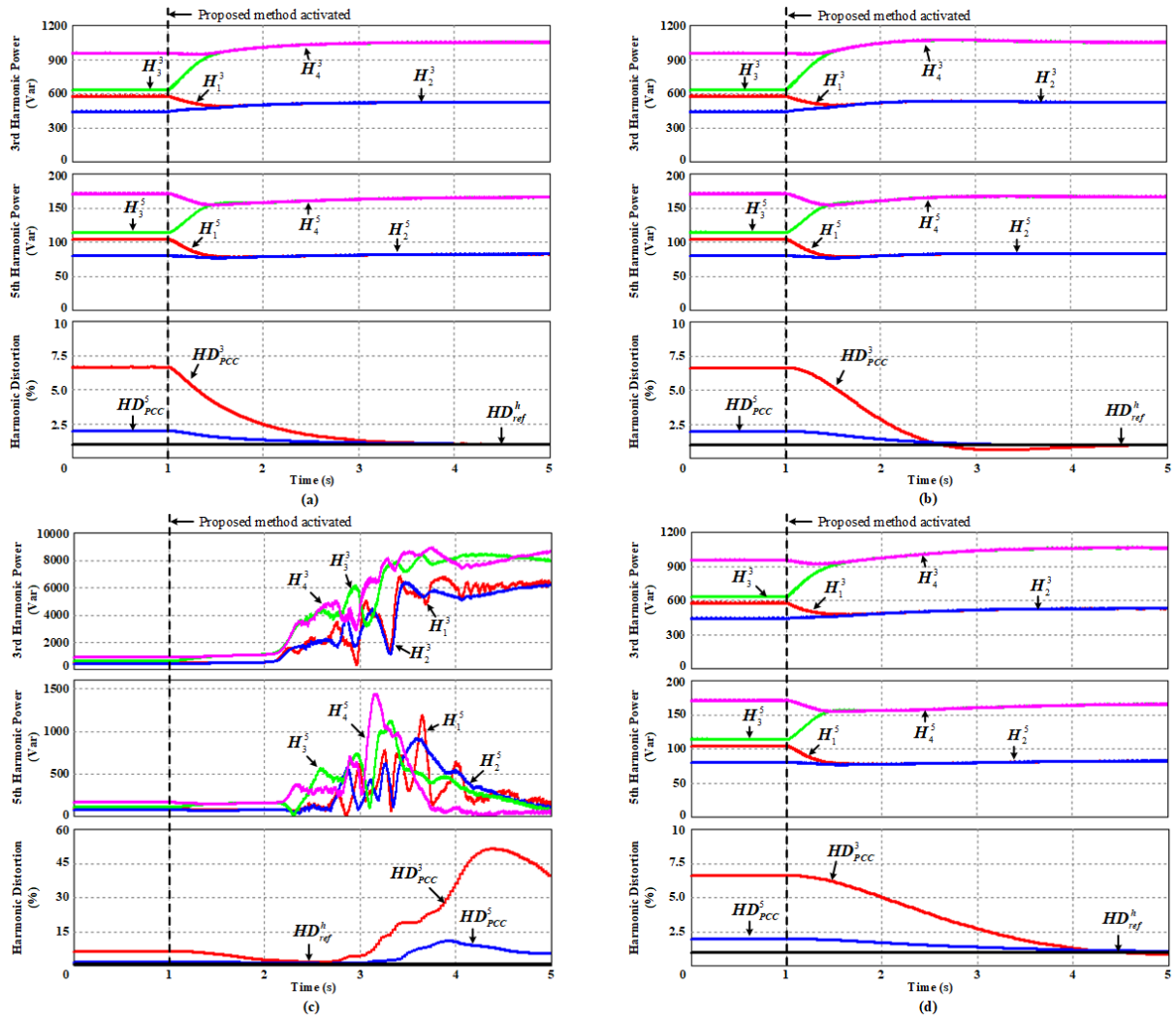

Figure 4.20: Dynamic responses for different communication delays and gains: (a) $\tau = 1ms$, $k_C^3 = 20$, $k_C^5 = 35$; (b) $\tau = 15ms$, $k_C^3 = 20$, $k_C^3 = 35$; (c) $\tau = 25ms$, $k_C^3 = 20$, $k_H^3 = 35$; (d) $\tau = 25ms$, $k_C^3 = 8$, $k_C^5 = 17$.

perfect control performance can be achieved with the proposed method (Figs. 4.20(a) and (b)). On the other hand, for the case of $\tau = 25ms$, the system cannot maintain the stability, and the accurate power sharing and the voltage harmonic compensation cannot be achieved (Fig. 4.20(c)). However, the system becomes stable when decreasing gains k_C^3 and k_C^5 to 8 and 17 despite large communication delay of $\tau = 25ms$, as shown in Fig. 4.20(d). From Fig. 4.20, we can say that there is a tradeoff between robustness of the control system to communication delays and its dynamic performance.

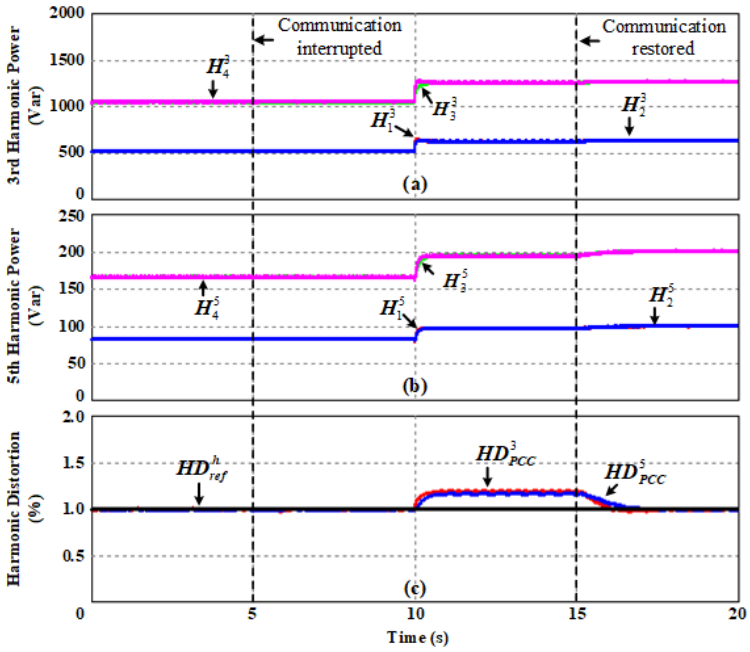

Figure 4.21: Control performance of the proposed controller before and after losing communication, and after recovering communication: (a) 3rd harmonic power; (b) 5th harmonic power; (c) harmonic distortion.

4.3.4 Communication Link Failure

Fig. 4.21 shows the control performance during communication interruption. In Fig. 4.21, the system in Fig. 4.5 is originally operated with the same operating condition as in stage 2 in Fig. 4.13. When the communication fault occurs at $5s$, all DGs stop regulating their virtual impedances and continue to operate with the fixed virtual impedance which is determined from the last regulation. As we can see, there is no change from 5 to $10s$ in the system, and the accurate power sharing and harmonic compensation are maintained despite the communication interruption. When Load 4 is connected at $10s$, even though the PCC harmonic distortions are no longer regulated at the reference value, they are still very low (see Fig. 4.21(c)). At $15s$, the communication is restored, and the enhanced controller is reactivated. As shown in Fig. 4.21, the perfect power sharing and harmonic compensation is recovered with effective virtual impedance regulation.

4.3.5 Effect of Local Load

Fig. 4.22 shows the control performance when a local load is sequentially connected to and disconnected from the system. Initially, the system in Fig. 4.5 operates with the same operating condition as in stage 3 in Fig. 4.13. At $5s$ and $10s$, Load 5 is connected to and disconnected from the system, respectively. As we can see, despite connecting and

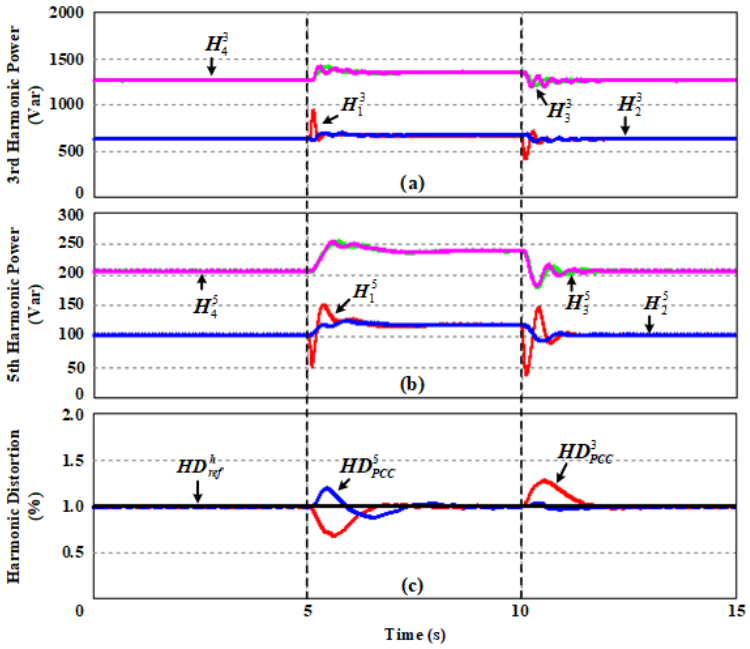

Figure 4.22: Control performance of the proposed controller when connecting and disconnecting a local load: (a) 3rd harmonic power; (b) 5th harmonic power; (c) harmonic distortion.

disconnecting a local load, the enhanced power sharing and harmonic compensation are maintained in steady state thanks to the proposed controller.

4.4 Experimental Results

Experiments were conducted with a simple single-phase scaled-down microgrid prototype with three DG units, as shown in Fig. 4.23. THD of the PCC voltage was measured by the Newtons4th PPA5530 Precision Power Analyzer. The system was controlled by the 32-bit floating-point 200MHz TMS320F28379D DSP. The data communication rate was the same as in the simulation, and the key parameters of the system are listed in Table 4.1.

Fig. 4.24 demonstrates the power sharing performance of the proposed method with four experimental stages. During stage 1 ($0 \leq t < t_1$), the microgrid in Fig. 4.23 is controlled by the conventional droop controller with Loads 1 and 2 (Load 3 is disconnected). During stage 2 ($t_1 \leq t < t_2$), the first virtual impedance part ($L^h_{virH,i}$) is applied at t_1. During stage 3 ($t_2 \leq t < t_3$), the second virtual impedance part ($L^h_{virC,i}$) is activated at t_2. Stage 4 starts from t_3 by connecting Load 3 in order to investigate the performance when the load condition is changed. As shown in Figs. 4.24(b)–(d), before t_1, the reactive, 3rd, and 5th harmonic powers are not equally shared among DG units. Nevertheless, when

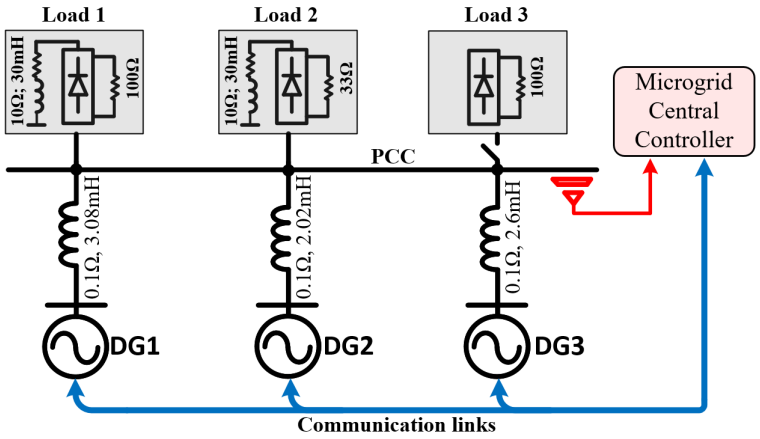

Figure 4.23: The islanded microgrid used for experiment: (a) photo of laboratory setup; (b) equivalent circuit.

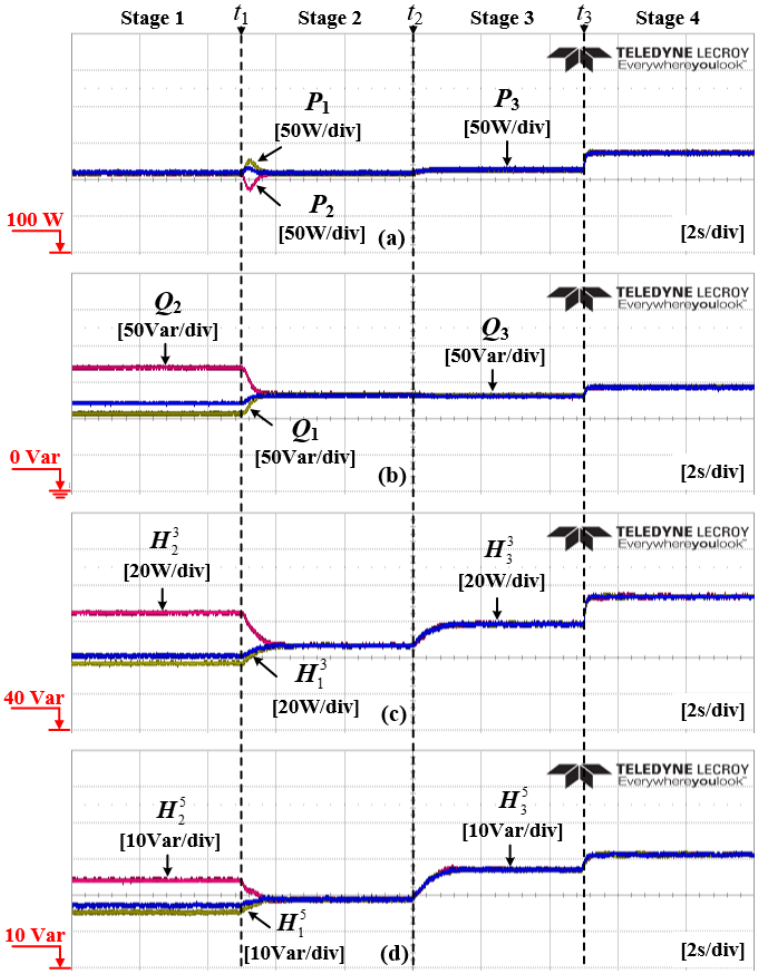

Figure 4.24: Experimental power sharing performance with proposed controller: (a) active power; (b) reactive power; (c) 3rd harmonic power; (d) 5th harmonic power.

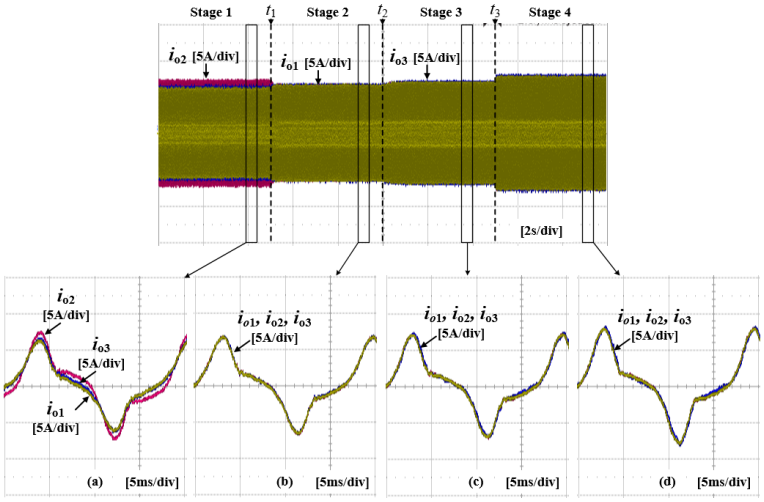

Figure 4.25: Zoom-in DG current waveforms with: (a) conventional droop method; (b) first virtual impedance part (activated at t1); (c) second virtual impedance part (activated at t2); (d) proposed method with increased load (Load 3 is connected at t3).

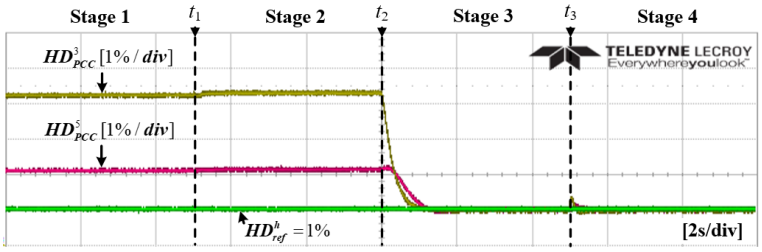

Figure 4.26: PCC harmonic distortion indexes.

the first virtual impedance part ($L^h_{virH,i}$) is applied at t_1, accurate fundamental and harmonic power sharing is realized. Even when the second virtual impedance part ($L^h_{virC,i}$) is activated at t_2 or the load condition is changed by connecting Load 3 at t_3, perfect power sharing for both linear and nonlinear loads is always maintained thanks to the proposed control scheme as shown in Figs. 4.24(a)–(d).

Fig. 4.25 shows a magnification of the DG output current waveforms corresponding to the stages in Fig. 4.24. In Fig. 4.25(a), the magnitude and phase of the DG currents are not the same with the conventional droop method. But they become identical once the first virtual impedance part ($L^h_{virH,i}$) is used (Fig. 4.25(b)). The second virtual impedance part ($L^h_{virC,i}$) has no effect on the power sharing performance (Fig. 4.25(c)). Additionally, the DG currents with the same magnitudes are maintained even when the load condition is changed by connecting a load (Fig. 4.25(d)).

Figs. 4.26 and 4.27 show the PCC voltage harmonic compensation performance with

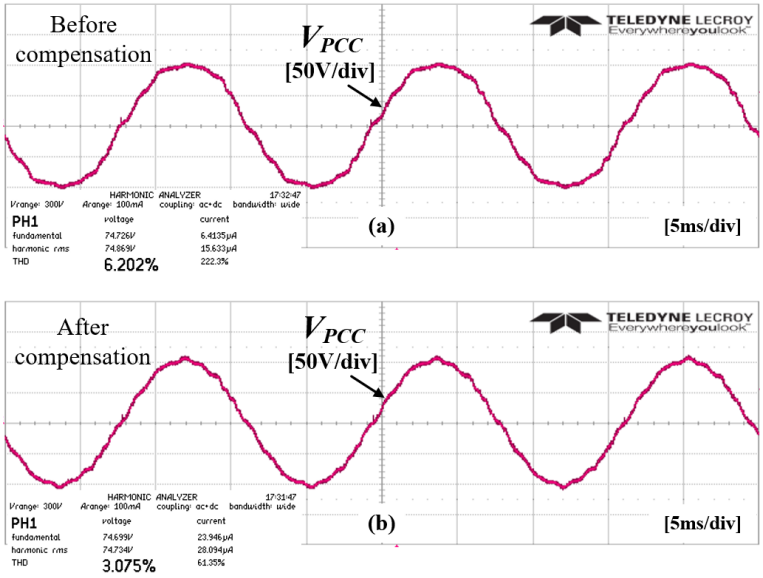

Figure 4.27: Zoom-in PCC voltage waveforms in: (a) stage 1; (b) stage 3.

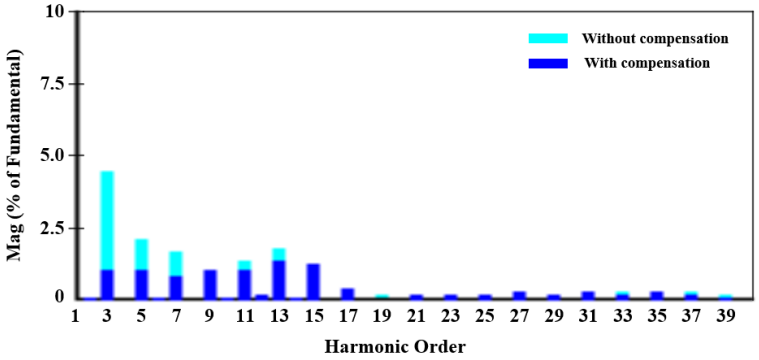

Figure 4.28: The harmonic spectra of PCC voltage waveforms without compensation in stage 1 (cyan) and with compensation in stage 3 (blue).

the proposed control scheme. The operating and load conditions change in the same scenarios as in Fig. 4.24. As shown in Fig. 4.26, the proposed scheme maintains the 3rd and 5th harmonic distortions at 1% regardless of the load change. As a result, the THD of PCC voltage is reduced from 6.202% to 3.075%, as shown in Fig. 4.27. Furthermore, the FFTs of the PCC voltage with and without the compensation are shown in Fig. 4.28. As clearly shown, the harmonic distortions are attenuated significantly thanks to the proposed controller.

Fig. 4.29 shows the dynamic performance for 3rd harmonic power sharing and the PCC harmonic compensation with various communication delays and control gains k_C^3 when the proposed method is activated. In Figs. 4.29(a) and (b), with higher gain of k_C^3 ($\tau = 10ms$), faster dynamic response of HD_{PCC}^3 can be achieved, but the 3th harmonic

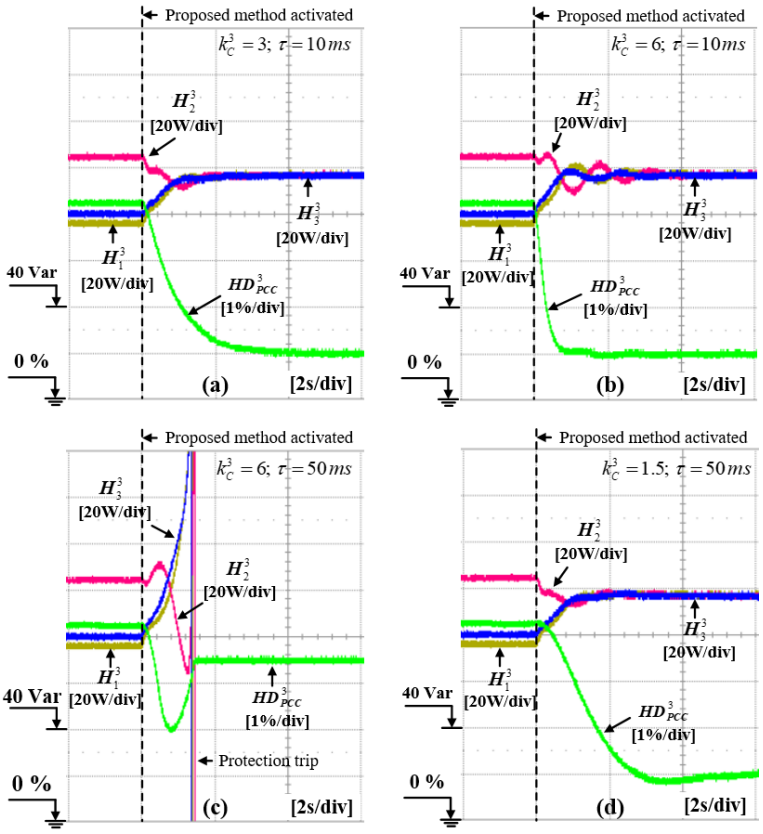

Figure 4.29: Dynamic performance with different communication delays and gains: (a) $\tau = 10ms$, $k_C^3 = 3$; (b) $\tau = 10ms$, $k_C^3 = 6$; (c) $\tau = 50ms$, $k_C^3 = 6$; (d) $\tau = 50ms$, $k_C^3 = 1.5$.

powers become more oscillated. By keeping the high gain $k_C^3 = 6$ and increasing the communication delay to $50ms$, the system stability cannot be maintained as shown in Fig. 4.29(c). However, the instability can be solved at the expense of slower response as shown in Fig. 4.29(d) when the gain k_C^3 reduces to 1.5. From Fig. 4.29, we can say that a larger gain provides a faster dynamic response, while a smaller gain helps to stabilize the system against communication delays.

4.5 Conclusion of the Chapter

Based on the mathematical analysis of an islanded microgrid, we proposed an enhanced virtual harmonic impedance control scheme to compensate for the PCC voltage harmonics without harmonic power sharing error for islanded microgrids. We also evaluated the system dynamics and stability using a small-signal state-space model. To attenuate voltage harmonic and achieve accurate harmonic power sharing simultaneously, the DG virtual impedance at a selected dominant harmonic frequency was directly regulated through two

controllable parts. The first one was adjusted to eliminate harmonic power sharing errors by compensating for the mismatch in feeder impedances. The second part was a negative impedance to attenuate the PCC voltage harmonics by reducing the DG equivalent feeder impedance.

Thanks to the proposed virtual harmonic impedance control scheme, the PCC voltage quality can be maintained within 5% THD with accurate harmonic power sharing, regardless of the load conditions. Only one virtual impedance control loop is used to realize the proposed control algorithm without any information about feeder impedances and load currents, so the control system is quite simple and easy to implement. The simulation and experimental results verified the performance of the proposed control scheme.

Chapter 5

Conclusions and Future Works

5.1 Conclusions

In this thesis, advanced control strategies have been developed for islanded AC microgrids. Power sharing and voltage quality issues were conducted to assess the control performance of these methods. First of all, the thesis investigated power sharing, frequency/voltage deviations, and voltage harmonic problems in islanded microgrids. Then, many advanced control schemes have been proposed to enhance microgrid control performance. These control schemes have been theoretically analyzed and verified through simulation and experiments.

In chaper 2, a centralized virtual impedance control scheme has been proposed to realize accurate active and reactive power sharing. The control scheme is very simple and easy to implement because no information about microgrid configuration is needed. Furthermore, it can maintained accurate power shairng even when the microgrid configuration or the load condition is changed. Therefore, it is very suitable for islanded microgrids, in which the structure is meshed or looped and the loads are mostly linear loads (nonlinear loads are negligible). However, because this scheme needs communication links between MGCC and DGs, it is very difficult to realize the scheme if an MGCC-DG communication link is impossible to be established due to geography condition. In such systems, the distributed control scheme in chapter 2 becomes a more suitable solution to realize accurate active and rective power sharing at the expense of higher bandwidth communication links.

When nonliear loads are extensively used, it is also important to obtain accurate harmonic power sharing and microgrid voltage harmonic compensation besides fundamental power sharing. Because active power filters (APFs) are conventionally used to compensate for voltage harmonics, an adaptive virtual impedance control scheme has been proposed in chapter 3 to share accurately active, reactive, and harmonic load powers among DGs.

This method is very suitable for meshed microgrids with both linear and nonlinear loads because accurate power sharing for both linear and nonlinear loads is always maintained regardless of microgrid configulation and load condition variations and no information about microgrid structure, line impedances, and load powers is needed.

However, in case of single-bus microgrids, the enhanced control scheme in chapter 4 is a more cost-effective solution because accurate power sharing and voltage harmonic compensation are always achieved without additional APFs. The scheme requires no information of line impedances. Therefore, it is very easy to implement.

5.2 Future works

Even though many methods have been proposed to solve the power control and power quality issues in islanded microgrids, in order to further enhance microgrid operation, some areas are needed to be researched in future such as:

- Distributed control strategies to compensate for PCC voltage harmonics,
- Sensorless synchronization methods for connecting a DG unit to the droop-controlled microgrid,
- Fault protection in AC microgrids such as short circuit protection, overload protection, and fault override capability of inverters.

Appendix A - State Matrices in Chapter 2

The matrices Ω_{MG} and Ω_{MG_d} in 2.58 are expressed as:

$$\Omega_{MG} = \begin{bmatrix} -\omega_{LPF} I_{n\times n} & \omega_{LPF}\Omega_{PQ} & \omega_{LPF}\Omega_{P\varphi} & \omega_{LPF}\Omega_{PX} \\ O_{n\times n} & \omega_{LPF}\Omega_{QQ} & \omega_{LPF}\Omega_{Q\varphi} & \omega_{LPF}\Omega_{QX} \\ \Omega_{\varphi P} & O_{n\times n} & O_{n\times n} & O_{n\times n} \\ O_{n\times n} & k_0\Omega_{XQ} & O_{n\times n} & O_{n\times n} \end{bmatrix}$$

and

$$\Omega_{MG\_d} = \begin{bmatrix} O_{n\times n} & \omega_{LPF}\Omega_{PQ\_d} & O_{n\times n} & O_{n\times n} \\ O_{n\times n} & \omega_{LPF}\Omega_{QQ\_d} & O_{n\times n} & O_{n\times n} \\ \Omega_{\varphi P\_d} & O_{n\times n} & O_{n\times n} & O_{n\times n} \\ O_{n\times n} & k_0\Omega_{XQ\_d} & O_{n\times n} & O_{n\times n} \end{bmatrix}$$

where:

$$I_{n\times n} = \begin{bmatrix} 1 & \cdots & 0 \\ \vdots & \ddots & \vdots \\ 0 & \cdots & 1 \end{bmatrix}, \Omega_{PQ} = \begin{bmatrix} -\alpha_{p1} n_1 & \cdots & 0 \\ \vdots & \ddots & \vdots \\ 0 & \cdots & -\alpha_{pn} n_n \end{bmatrix},$$

$$\Omega_{P\varphi} = \begin{bmatrix} \beta_{p1} & \cdots & 0 \\ \vdots & \ddots & \vdots \\ 0 & \cdots & \beta_{pn} \end{bmatrix}, \Omega_{PX} = \begin{bmatrix} \gamma_{p1} & \cdots & 0 \\ \vdots & \ddots & \vdots \\ 0 & \cdots & \gamma_{pn} \end{bmatrix},$$

$$O_{n\times n} = \begin{bmatrix} 0 & \cdots & 0 \\ \vdots & \ddots & \vdots \\ 0 & \cdots & 0 \end{bmatrix}, \Omega_{QQ} = \begin{bmatrix} -(1+\alpha_{q1} n_1) & \cdots & 0 \\ \vdots & \ddots & \vdots \\ 0 & \cdots & -(1+\alpha_{qn} n_n) \end{bmatrix},$$

$$\Omega_{Q\varphi} = \begin{bmatrix} \beta_{q1} & \cdots & 0 \\ \vdots & \ddots & \vdots \\ 0 & \cdots & \beta_{qn} \end{bmatrix}, \Omega_{QX} = \begin{bmatrix} \gamma_{q1} & \cdots & 0 \\ \vdots & \ddots & \vdots \\ 0 & \cdots & \gamma_{qn} \end{bmatrix},$$

$$\Omega_{\varphi P} = \begin{bmatrix} -m_1 & \cdots & 0 \\ \vdots & \ddots & \vdots \\ 0 & \cdots & -m_n \end{bmatrix}, \Omega_{XQ} = \begin{bmatrix} |N_1|\, n_1 & \cdots & 0 \\ \vdots & \ddots & \vdots \\ 0 & \cdots & |N_n|\, n_n \end{bmatrix},$$

$$\Omega_{PQ\_d} = \begin{bmatrix} 0 & a_{12}\alpha_{p1}n_2\,|N_1|^{-1} & \cdots & a_{1n}\alpha_{p1}n_n\,|N_1|^{-1} \\ a_{21}\alpha_{p2}n_1\,|N_2|^{-1} & 0 & \cdots & a_{2n}\alpha_{p2}n_n\,|N_2|^{-1} \\ \vdots & \vdots & \ddots & \vdots \\ a_{n1}\alpha_{pn}n_1\,|N_n|^{-1} & a_{n2}\alpha_{pn}n_2\,|N_n|^{-1} & \cdots & 0 \end{bmatrix},$$

$$\Omega_{QQ\_d} = \begin{bmatrix} 0 & a_{12}\alpha_{q1}n_2\,|N_1|^{-1} & \cdots & a_{1n}\alpha_{q1}n_n\,|N_1|^{-1} \\ a_{21}\alpha_{q2}n_1\,|N_2|^{-1} & 0 & \cdots & a_{2n}\alpha_{q2}n_n\,|N_2|^{-1} \\ \vdots & \vdots & \ddots & \vdots \\ a_{n1}\alpha_{qn}n_1\,|N_n|^{-1} & a_{n2}\alpha_{qn}n_2\,|N_n|^{-1} & \cdots & 0 \end{bmatrix},$$

$$\Omega_{\varphi P\_d} = \begin{bmatrix} 0 & a_{12}m_2\,|N_1|^{-1} & \cdots & a_{1n}m_n\,|N_1|^{-1} \\ a_{21}m_1\,|N_2|^{-1} & 0 & \cdots & a_{2n}m_n\,|N_2|^{-1} \\ \vdots & \vdots & \ddots & \vdots \\ a_{n1}m_1\,|N_n|^{-1} & a_{n2}m_2\,|N_n|^{-1} & \cdots & 0 \end{bmatrix},$$

$$\Omega_{XQ\_d} = \begin{bmatrix} 0 & -a_{12}n_2 & \cdots & -a_{1n}n_n \\ -a_{21}n_1 & 0 & \cdots & -a_{2n}n_n \\ \vdots & \vdots & \ddots & \vdots \\ -a_{n1}n_1 & -a_{n2}n_2 & \cdots & 0 \end{bmatrix}.$$

Appendix B - State Matrices in Chapter 4

The matrixes A_{MG} in 4.38 and Ω_{MG} and Ω_{MG_d} in 4.40 are expressed as:

$$A_{MG} = \begin{bmatrix} O_{n\times n} & A_{LH} & A_{LHD} \\ \frac{\omega_{LPF}E_0}{2}A_{HL} & A_{HH} & O_{n\times 1} \\ A_{HDL} & O_{1\times n} & -\omega_{LPF} \end{bmatrix}, \Omega_{MG} = \begin{bmatrix} O_{n\times n} & A_{LH} & O_{n\times 1} \\ \frac{\omega_{LPF}E_0}{2}A_{HL} & A_{HH} & O_{n\times 1} \\ A_{HDL} & O_{1\times n} & -\omega_{LPF} \end{bmatrix},$$

and

$$\Omega_{MG\_d} = \begin{bmatrix} O_{n\times n} & O_{n\times n} & A_{LHD} \\ O_{n\times n} & O_{n\times n} & O_{n\times 1} \\ O_{1\times n} & O_{1\times n} & 0 \end{bmatrix},$$

where:

$$O_{n\times n} = \begin{bmatrix} 0 & \cdots & 0 \\ \vdots & \ddots & \vdots \\ 0 & \cdots & 0 \end{bmatrix}, A_{LH} = \begin{bmatrix} k_H & \cdots & 0 \\ \vdots & \ddots & \vdots \\ 0 & \cdots & k_H \end{bmatrix},$$

$$A_{LHD} = \begin{bmatrix} \frac{-k_c}{H_{rated,1}} & \frac{-k_c}{H_{rated,2}} & \cdots & \frac{-k_c}{H_{rated,n}} \end{bmatrix}^T,$$

$$A_{HL} = \frac{\omega_{LPF}E_0}{2} \begin{bmatrix} \frac{\alpha_1}{h\omega L^h_{eq,1}} - \frac{V^h_{PCC}}{h\omega\left(L^h_{eq,1}\right)^2} & \cdots & \frac{\alpha_n}{h\omega L^h_{eq,1}} \\ \vdots & \ddots & \vdots \\ \frac{\alpha_1}{h\omega L^h_{eq,n}} & \cdots & \frac{\alpha_n}{h\omega L^h_{eq,n}} - \frac{V^h_{PCC}}{h\omega\left(L^h_{eq,n}\right)^2} \end{bmatrix},$$

$$A_{HH} = \begin{bmatrix} -\omega_{LPF} & \cdots & 0 \\ \vdots & \ddots & \vdots \\ 0 & \cdots & -\omega_{LPF} \end{bmatrix}, O_{n\times 1} = \begin{bmatrix} 0 & 0 & \cdots & 0 \end{bmatrix}^T,$$

$$A_{HDL} = \frac{100\omega_{LPF}}{V^f_{PCC}} \begin{bmatrix} \alpha_1 & \alpha_2 & \cdots & \alpha_n \end{bmatrix}, O_{1\times n} = \begin{bmatrix} 0 & 0 & \cdots & 0 \end{bmatrix}.$$

Appendix C - Publications

Journal Articles

1. T. V. Hoang and H. Lee, "An Adaptive Virtual Impedance Control Scheme to Eliminate the Reactive-Power-Sharing Errors in an Islanding Meshed Microgrid," in *IEEE Journal of Emerging and Selected Topics in Power Electronics*, vol. 6, no. 2, pp. 966-976, Jun. 2018.

2. T. V. Hoang and H. Lee, "Accurate Power Sharing With Harmonic Power for Islanded Multibus Microgrids," in *IEEE Journal of Emerging and Selected Topics in Power Electronics*, vol. 7, no. 2, pp. 1286-1299, Jun. 2019.

3. T. V. Hoang and H. Lee, "Distributed control scheme for accurate reactive power sharing with enhanced voltage quality for islanded microgrids," in *Journal of Power Electronics*, vol. 20, no. 2, pp. 601–613, Mar. 2020.

4. T. V. Hoang and H. Lee, "Virtual Impedance Control Scheme to Compensate for Voltage Harmonics with Accurate Harmonic Power Sharing in Islanded Microgrids," in in *IEEE Journal of Emerging and Selected Topics in Power Electronics*, vol. x, no. x, pp. 1–1, 2020.

Conferences

1. T. V. Hoang, T. D. Nguyen and H. Lee, "Adaptive virtual impedance control scheme to eliminate reactive power sharing errors in islanded microgrid," in *Proc. IEEE International Conference on Sustainable Energy Technologies (ICSET)*, Hanoi, 2016, pp. 224-229.

2. T. V. Hoang and H. Lee, "Distributed Power Sharing Strategy for Islanded Microgrids without Frequency and Voltage Deviations," in *Proc. International Power Electronics Conference (IPEC-Niigata 2018 -ECCE Asia)*, Niigata, 2018, pp. 1752-1757.

3. T. V. Hoang and H. Lee, "A Distributed Power Sharing Approach for Islanded Microgrids," in *Proc. 17th International Conference on Renewable Energies and Power Quality(ICREPQ'19)*, Tenerife, Spain, 2019, pp. 123-127.

4. T. V. Hoang and H. Lee, "A Distributed Harmonic Power Sharing Strategy for Islanded Microgrids," in *Proc. 10th International Conference on Power Electronics and ECCE Asia (ICPE 2019 - ECCE Asia)*, Busan, Korea (South), 2019, pp. 1-6.

Bibliography

[1] J. Schonbergerschonberger, R. Duke, and S. D. Round, "DC-Bus Signaling: A Distributed Control Strategy for a Hybrid Renewable Nanogrid," *IEEE Transactions on Industrial Electronics*, vol. 53, no. 5, pp. 1453–1460, oct 2006.

[2] F. Katiraei and M. R. Iravani, "Power management strategies for a microgrid with multiple distributed generation units," *IEEE Transactions on Power Systems*, vol. 21, no. 4, pp. 1821–1831, Nov 2006.

[3] A. Keane and M. O'Malley, "Optimal allocation of embedded generation on distribution networks," *IEEE Transactions on Power Systems*, vol. 20, no. 3, pp. 1640–1646, Aug 2005.

[4] J. M. Carrasco, L. G. Franquelo, J. T. Bialasiewicz, E. Galvan, R. C. PortilloGuisado, M. A. M. Prats, J. I. Leon, and N. Moreno-Alfonso, "Power-electronic systems for the grid integration of renewable energy sources: A survey," *IEEE Transactions on Industrial Electronics*, vol. 53, no. 4, pp. 1002–1016, June 2006.

[5] F. Blaabjerg, Zhe Chen, and S. B. Kjaer, "Power electronics as efficient interface in dispersed power generation systems," *IEEE Transactions on Power Electronics*, vol. 19, no. 5, pp. 1184–1194, Sep. 2004.

[6] Yaosuo Xue, Liuchen Chang, Sren Baekhj Kjaer, J. Bordonau, and T. Shimizu, "Topologies of single-phase inverters for small distributed power generators: an overview," *IEEE Transactions on Power Electronics*, vol. 19, no. 5, pp. 1305–1314, Sep. 2004.

[7] M. Montoya, R. Sherick, P. Haralson, R. Neal, and R. Yinger, "Islands in the storm: Integrating microgrids into the larger grid," *IEEE Power and Energy Magazine*, vol. 11, no. 4, pp. 33–39, July 2013.

[8] A. Mehrizi-Sani and R. Iravani, "Potential-function based control of a microgrid in islanded and grid-connected modes," *IEEE Transactions on Power Systems*, vol. 25, no. 4, pp. 1883–1891, 2010.

[9] J. C. Vasquez, J. M. Guerrero, A. Luna, P. Rodriguez, and R. Teodorescu, "Adaptive droop control applied to voltage-source inverters operating in grid-connected and islanded modes," *IEEE Transactions on Industrial Electronics*, vol. 56, no. 10, pp. 4088–4096, Oct 2009.

[10] J. Kim, J. M. Guerrero, P. Rodriguez, R. Teodorescu, and K. Nam, "Mode adaptive droop control with virtual output impedances for an inverter-based flexible ac microgrid," *IEEE Transactions on Power Electronics*, vol. 26, no. 3, pp. 689–701, March 2011.

[11] M. A. Zamani, T. S. Sidhu, and A. Yazdani, "Investigations into the control and protection of an existing distribution network to operate as a microgrid: A case study," *IEEE Transactions on Industrial Electronics*, vol. 61, no. 4, pp. 1904–1915, April 2014.

[12] F. Katiraei, R. Iravani, N. Hatziargyriou, and A. Dimeas, "Microgrids management," *IEEE Power and Energy Magazine*, vol. 6, no. 3, pp. 54–65, May 2008.

[13] J. A. P. Lopes, C. L. Moreira, and A. G. Madureira, "Defining control strategies for microgrids islanded operation," *IEEE Transactions on Power Systems*, vol. 21, no. 2, pp. 916–924, May 2006.

[14] J. M. Guerrero, J. Matas, L. G. D. V. D. Vicuna, M. Castilla, and J. Miret, "Wireless-Control Strategy for Parallel Operation of Distributed-Generation Inverters," *IEEE Transactions on Industrial Electronics*, vol. 53, no. 5, pp. 1461–1470, oct 2006.

[15] K. D. Brabandere, B. Bolsens, J. V. den Keybus, A. Woyte, J. Driesen, and R. Belmans, "A Voltage and Frequency Droop Control Method for Parallel Inverters," *IEEE Transactions on Power Electronics*, vol. 22, no. 4, pp. 1107–1115, jul 2007.

[16] J. C. Vasquez, R. A. Mastromauro, J. M. Guerrero, and M. Liserre, "Voltage Support Provided by a Droop-Controlled Multifunctional Inverter," *IEEE Transactions on Industrial Electronics*, vol. 56, no. 11, pp. 4510–4519, nov 2009.

[17] J. He, Y. W. Li, J. M. Guerrero, F. Blaabjerg, and J. C. Vasquez, "An Islanding Microgrid Power Sharing Approach Using Enhanced Virtual Impedance Control Scheme," *IEEE Transactions on Power Electronics*, vol. 28, no. 11, pp. 5272–5282, nov 2013.

[18] J. He and Y. W. Li, "An enhanced microgrid load demand sharing strategy," *IEEE Transactions on Power Electronics*, vol. 27, no. 9, pp. 3984–3995, Sep. 2012.

[19] T. V. Hoang and H. Lee, "An Adaptive Virtual Impedance Control Scheme to Eliminate the Reactive-Power-Sharing Errors in an Islanding Meshed Microgrid," *IEEE Journal of Emerging and Selected Topics in Power Electronics*, vol. 6, no. 2, pp. 966–976, jun 2018.

[20] ——, "Accurate Power Sharing with Harmonic Power for Islanded Multibus Microgrids," *IEEE Journal of Emerging and Selected Topics in Power Electronics*, p. 1, 2018.

[21] Y. W. Li, "Control and resonance damping of voltage-source and current-source converters with *lc* filters," *IEEE Transactions on Industrial Electronics*, vol. 56, no. 5, pp. 1511–1521, May 2009.

[22] H. Han, Y. Liu, Y. Sun, M. Su, J. M. Guerrero, and S. Member, "An Improved Droop Control Strategy for Reactive Power Sharing in Islanded Microgrid," vol. 30, no. 6, pp. 3133–3141, 2015.

[23] J. He, Y. W. Li, and F. Blaabjerg, "An Enhanced Islanding Microgrid Reactive Power, Imbalance Power, and Harmonic Power Sharing Scheme," *IEEE Transactions on Power Electronics*, vol. 30, no. 6, pp. 3389–3401, jun 2015.

[24] H. Han, X. Hou, J. Yang, J. Wu, M. Su, and J. M. Guerrero, "Review of Power Sharing Control Strategies for Islanding Operation of AC Microgrids," *IEEE Transactions on Smart Grid*, vol. 7, no. 1, pp. 200–215, jan 2016.

[25] Y. Han, H. Li, P. Shen, E. A. A. Coelho, and J. M. Guerrero, "Review of Active and Reactive Power Sharing Strategies in Hierarchical Controlled Microgrids," *IEEE Transactions on Power Electronics*, vol. 32, no. 3, pp. 2427–2451, mar 2017.

[26] Y. W. Li and C. Kao, "An accurate power control strategy for power-electronics-interfaced distributed generation units operating in a low-voltage multibus microgrid," *IEEE Transactions on Power Electronics*, vol. 24, no. 12, pp. 2977–2988, Dec 2009.

[27] C. Lee, C. Chu, and P. Cheng, "A new droop control method for the autonomous operation of distributed energy resource interface converters," *IEEE Transactions on Power Electronics*, vol. 28, no. 4, pp. 1980–1993, April 2013.

[28] Q. Zhong, "Robust droop controller for accurate proportional load sharing among inverters operated in parallel," *IEEE Transactions on Industrial Electronics*, vol. 60, no. 4, pp. 1281–1290, April 2013.

[29] J. He, Y. Pan, B. Liang, and C. Wang, "A simple decentralized islanding microgrid power sharing method without using droop control," *IEEE Transactions on Smart Grid*, vol. 9, no. 6, pp. 6128–6139, Nov 2018.

[30] J. M. Guerrero, L. G. de Vicuna, J. Matas, M. Castilla, and J. Miret, "Output impedance design of parallel-connected UPS inverters with wireless load-sharing control," *IEEE Transactions on Industrial Electronics*, vol. 52, no. 4, pp. 1126–1135, aug 2005.

[31] W. Yao, M. Chen, J. Matas, J. M. Guerrero, and Z. Qian, "Design and Analysis of the Droop Control Method for Parallel Inverters Considering the Impact of the Complex Impedance on the Power Sharing," *IEEE Transactions on Industrial Electronics*, vol. 58, no. 2, pp. 576–588, feb 2011.

[32] J. M. Guerrero, J. Matas, L. Garcia de Vicuna, M. Castilla, and J. Miret, "Decentralized control for parallel operation of distributed generation inverters using resistive output impedance," *IEEE Transactions on Industrial Electronics*, vol. 54, no. 2, pp. 994–1004, April 2007.

[33] Y. Zhu, F. Zhuo, F. Wang, B. Liu, and Y. Zhao, "A Wireless Load Sharing Strategy for Islanded Microgrid Based on Feeder Current Sensing," *IEEE Transactions on Power Electronics*, vol. 30, no. 12, pp. 6706–6719, 2015.

[34] L. Lin, H. Ma, and Z. Bai, "An Improved Proportional Load-Sharing Strategy for Meshed Parallel Inverters System With Complex Impedances," *IEEE Transactions on Power Electronics*, vol. 32, no. 9, pp. 7338–7351, sep 2017.

[35] G. Celli, F. Pilo, G. Pisano, V. Allegranza, R. Cicoria, and A. Iaria, "Meshed vs. radial mv distribution network in presence of large amount of dg," in *IEEE PES Power Systems Conference and Exposition, 2004.*, Oct 2004, pp. 709–714 vol.2.

[36] Y. Zhu, B. Liu, F. Wang, F. Zhuo, and Y. Zhao, "A virtual resistance based reactive power sharing strategy for networked microgrid," in *2015 9th International Conference on Power Electronics and ECCE Asia (ICPE-ECCE Asia)*, June 2015, pp. 1564–1572.

[37] Y. Zhu, F. Zhuo, F. Wang, B. Liu, R. Gou, and Y. Zhao, "A Virtual Impedance Optimization Method for Reactive Power Sharing in Networked Microgrid," *IEEE Transactions on Power Electronics*, vol. 31, no. 4, pp. 2890–2904, apr 2016.

[38] H. Zhang, S. Kim, Q. Sun, and J. Zhou, "Distributed Adaptive Virtual Impedance Control for Accurate Reactive Power Sharing Based on Consensus Control in Microgrids," *IEEE Transactions on Smart Grid*, vol. 8, no. 4, pp. 1749–1761, jul 2017.

[39] J. Zhou, S. Kim, H. Zhang, Q. Sun, and R. Han, "Consensus-based distributed control for accurate reactive, harmonic, and imbalance power sharing in microgrids," *IEEE Transactions on Smart Grid*, vol. 9, no. 4, pp. 2453–2467, July 2018.

[40] H. Mahmood, D. Michaelson, and J. Jiang, "Accurate Reactive Power Sharing in an Islanded Microgrid Using Adaptive Virtual Impedances," *IEEE Transactions on Power Electronics*, vol. 30, no. 3, pp. 1605–1617, mar 2015.

[41] H. Moussa, A. Shahin, J. Martin, B. Nahid-Mobarakeh, S. Pierfederici, and N. Moubayed, "Harmonic Power Sharing With Voltage Distortion Compensation of Droop Controlled Islanded Microgrids," *IEEE Transactions on Smart Grid*, vol. 9, no. 5, pp. 5335–5347, 2018.

[42] J. M. Guerrero, J. C. Vasquez, J. Matas, L. G. de Vicuna, and M. Castilla, "Hierarchical Control of Droop-Controlled AC and DC Microgrids—A General Approach Toward Standardization," *IEEE Transactions on Industrial Electronics*, vol. 58, no. 1, pp. 158–172, jan 2011.

[43] Y. Han, P. Shen, X. Zhao, and J. M. Guerrero, "Control Strategies for Islanded Microgrid Using Enhanced Hierarchical Control Structure With Multiple Current-Loop Damping Schemes," *IEEE Transactions on Smart Grid*, vol. 8, no. 3, pp. 1139–1153, may 2017.

[44] Q. Guo, H. Wu, L. Lin, Z. Bai, and H. Ma, "Secondary Voltage Control for Reactive Power Sharing in an Islanded Microgrid," vol. 16, no. 1, pp. 329–339, 2016.

[45] F. Guo, C. Wen, J. Mao, and Y. Song, "Distributed secondary voltage and frequency restoration control of droop-controlled inverter-based microgrids," *IEEE Transactions on Industrial Electronics*, vol. 62, no. 7, pp. 4355–4364, July 2015.

[46] Q. Shafiee, J. M. Guerrero, and J. C. Vasquez, "Distributed Secondary Control for Islanded Microgrids—A Novel Approach," *IEEE Transactions on Power Electronics*, vol. 29, no. 2, pp. 1018–1031, feb 2014.

[47] Q. Shafiee, V. Nasirian, J. C. Vasquez, J. M. Guerrero, and A. Davoudi, "A multi-functional fully distributed control framework for ac microgrids," *IEEE Transactions on Smart Grid*, vol. 9, no. 4, pp. 3247–3258, July 2018.

[48] X. Wu, C. Shen, and R. Iravani, "A Distributed, Cooperative Frequency and Voltage Control for Microgrids," *IEEE Transactions on Smart Grid*, vol. 9, no. 4, pp. 2764–2776, jul 2018.

[49] X. Hou, Y. Sun, J. Lu, X. Zhang, L. H. Koh, M. Su, and J. M. Guerrero, "Distributed Hierarchical Control of AC Microgrid Operating in Grid-Connected, Islanded and Their Transition Modes," *IEEE Access*, vol. 6, pp. 77 388–77 401, 2018.

[50] R. Han, L. Meng, G. Ferrari-Trecate, E. A. A. Coelho, J. C. Vasquez, and J. M. Guerrero, "Containment and Consensus-Based Distributed Coordination Control to Achieve Bounded Voltage and Precise Reactive Power Sharing in Islanded AC Microgrids," *IEEE Transactions on Industry Applications*, vol. 53, no. 6, pp. 5187–5199, nov 2017.

[51] J. W. Simpson-Porco, Q. Shafiee, F. Dörfler, J. C. Vasquez, J. M. Guerrero, and F. Bullo, "Secondary Frequency and Voltage Control of Islanded Microgrids via Distributed Averaging," *IEEE Transactions on Industrial Electronics*, vol. 62, no. 11, pp. 7025–7038, nov 2015.

[52] X. Wang, F. Blaabjerg, and Z. Chen, "Autonomous Control of Inverter-Interfaced Distributed Generation Units for Harmonic Current Filtering and Resonance Damping in an Islanded Microgrid," *IEEE Transactions on Industry Applications*, vol. 50, no. 1, pp. 452–461, jan 2014.

[53] A. Micallef, M. Apap, C. Spiteri-Staines, and J. M. Guerrero, "Mitigation of Harmonics in Grid-Connected and Islanded Microgrids Via Virtual Admittances and Impedances," *IEEE Transactions on Smart Grid*, vol. 8, no. 2, pp. 651–661, mar 2017.

[54] Y. Han, P. Shen, X. Zhao, and J. M. Guerrero, "An Enhanced Power Sharing Scheme for Voltage Unbalance and Harmonics Compensation in an Islanded AC Microgrid," *IEEE Transactions on Energy Conversion*, vol. 31, no. 3, pp. 1037–1050, 2016.

[55] M. Savaghebi, A. Jalilian, J. C. Vasquez, and J. M. Guerrero, "Secondary Control for Voltage Quality Enhancement in Microgrids," *IEEE Transactions on Smart Grid*, vol. 3, no. 4, pp. 1893–1902, dec 2012.

[56] ——, "Secondary Control Scheme for Voltage Unbalance Compensation in an Islanded Droop-Controlled Microgrid," *IEEE Transactions on Smart Grid*, vol. 3, no. 2, pp. 797–807, jun 2012.

[57] L. Meng, X. Zhao, F. Tang, M. Savaghebi, T. Dragicevic, J. C. Vasquez, and J. M. Guerrero, "Distributed Voltage Unbalance Compensation in Islanded Microgrids by Using a Dynamic Consensus Algorithm," *IEEE Transactions on Power Electronics*, vol. 31, no. 1, pp. 827–838, jan 2016.

[58] "IEEE Recommended Practices and Requirements for Harmonic Control in Electrical Power Systems," *IEEE Std 519-1992*, pp. 1–112, apr 1993.

[59] J. He, Y. W. Li, and M. S. Munir, "A Flexible Harmonic Control Approach Through Voltage-Controlled DG–Grid Interfacing Converters," *IEEE Transactions on Industrial Electronics*, vol. 59, no. 1, pp. 444–455, jan 2012.

[60] G. Yajuan, W. Weiyang, G. Xiaoqiang, and G. Herong, "An improved droop controller for grid-connected voltage source inverter in microgrid," in *The 2nd International Symposium on Power Electronics for Distributed Generation Systems*, June 2010, pp. 823–828.

[61] Y. A. I. Mohamed and E. F. El-Saadany, "Adaptive decentralized droop controller to preserve power sharing stability of paralleled inverters in distributed generation microgrids," *IEEE Transactions on Power Electronics*, vol. 23, no. 6, pp. 2806–2816, Nov 2008.

[62] R. Olfati-Saber and R. M. Murray, "Consensus problems in networks of agents with switching topology and time-delays," *IEEE Transactions on Automatic Control*, vol. 49, no. 9, pp. 1520–1533, sep 2004.

[63] Y. Sun, X. Hou, J. Yang, H. Han, M. Su, and J. M. Guerrero, "New Perspectives on Droop Control in AC Microgrid," *IEEE Transactions on Industrial Electronics*, vol. 64, no. 7, pp. 5741–5745, jul 2017.

[64] G. Chen and Z. Guo, "Distributed Secondary and Optimal Active Power Sharing Control for Islanded Microgrids with Communication Delays," *IEEE Transactions on Smart Grid*, p. 1, 2018.

[65] E. A. A. Coelho, D. Wu, J. M. Guerrero, J. C. Vasquez, T. Dragičević, Č. Stefanović, and P. Popovski, "Small-Signal Analysis of the Microgrid Secondary Control Considering a Communication Time Delay," *IEEE Transactions on Industrial Electronics*, vol. 63, no. 10, pp. 6257–6269, oct 2016.

[66] A. Kahrobaeian and Y. A. Ibrahim Mohamed, "Networked-Based Hybrid Distributed Power Sharing and Control for Islanded Microgrid Systems," *IEEE Transactions on Power Electronics*, vol. 30, no. 2, pp. 603–617, feb 2015.

[67] P. Sreekumar and V. Khadkikar, "A new virtual harmonic impedance scheme for harmonic power sharing in an islanded microgrid," in *2016 IEEE Power and Energy Society General Meeting (PESGM)*, jul 2016, p. 1.

[68] "IEEE Standard Definitions for the Measurement of Electric Power Quantities Under Sinusoidal, Nonsinusoidal, Balanced, or Unbalanced Conditions," *IEEE Std 1459-2010 (Revision of IEEE Std 1459-2000)*, pp. 1–50, mar 2010.

[69] J. He and Y. W. Li, "Analysis, Design, and Implementation of Virtual Impedance for Power Electronics Interfaced Distributed Generation," *IEEE Transactions on Industry Applications*, vol. 47, no. 6, pp. 2525–2538, nov 2011.

[70] Y. Qi, P. Lin, Y. Wang, and Y. Tang, "Two-Dimensional Impedance-Shaping Control with Enhanced Harmonic Power Sharing for Inverter-Based Microgrids," *IEEE Transactions on Power Electronics*, p. 1, 2019.